Flexible devices based on layered 2D materials

Radatović, Borna

Doctoral thesis / Disertacija

2022

Degree Grantor / Ustanova koja je dodijelila akademski / stručni stupanj: **University of Zagreb, Faculty of Science / Sveučilište u Zagrebu, Prirodoslovno-matematički fakultet**

Permanent link / Trajna poveznica: https://urn.nsk.hr/urn:nbn:hr:217:907149

Rights / Prava: In copyright / Zaštićeno autorskim pravom.

Download date / Datum preuzimanja: **2025-02-02**

Repository / Repozitorij:

Repository of the Faculty of Science - University of Zagreb

University of Zagreb

UNIVERSITY OF ZAGREB
FACULTY OF SCIENCE
DEPARTMENT OF PHYSICS

Borna Radatović

FLEXIBLE DEVICES BASED ON LAYERED 2D MATERIALS

DOCTORAL THESIS

Zagreb, 2022.

University of Zagreb

UNIVERSITY OF ZAGREB
FACULTY OF SCIENCE
DEPARTMENT OF PHYSICS

Borna Radatović

FLEXIBLE DEVICES BASED ON LAYERED 2D MATERIALS

DOCTORAL THESIS

Supervisor: dr. sc. Marin Petrović

Zagreb, 2022.

Sveučilište u Zagrebu

SVEUČILIŠTE U ZAGREBU
PRIRODOSLOVNO-MATEMATIČKI FAKULTET
FIZIČKI ODSJEK

Borna Radatović

Fleksibilni uređaji bazirani na slojevitim 2D materijalima

DOKTORSKI RAD

Mentor: dr. sc. Marin Petrović

Zagreb, 2022.

INFORMATION ABOUT MENTOR AND PROJECTS

This thesis was done under the mentorship of dr. sc. Marin Petrović as a part of the doctoral study at the Department of Physics, Faculty of Science, University of Zagreb. Presented work was carried out at the Institute of Physics in Zagreb, with significant visits to the University of Münster and Material science Institute in Madrid. The work presented within this thesis was funded through Center of Excellence for Advanced Materials and Sensing Devices (ERDF grant no. KK. 01.1.1.01.0001.), Center for Advanced Laser Techniques (ERDF grant no. KK. 01.1.1.05, HRZZ projects (UIP – 2020-02-1732 Boron based 2D materials", and UIP –2017-05-3869 "Photoexcitations in 2D semiconductors") and bilateral projects (Austria – "Organic semiconductor nanostructures on two-dimensional transition metal dichalcogenide substrates," China – "Synthesis of novel low-dimensional materials for information applications and the characterisation of their magnetic and optical properties," Serbia – Tuning many-body interactions in graphene by cesium intercalation," and with Germany "Two-dimensional metals" and "Intercalation of epitaxial dichalcogenides").

Marin Petrović finished his Ph.D. studies in physics in 2014. at the Institute of Physics in Zagreb, under the supervision of dr. sc. Marko Kralj and with the topic of synthesis and intercalation of graphene. During his postdoctoral Humboldt fellowship at the University of Duisburg-Essen in 2016. and 2017., he continued investigation of 2D materials, mainly hexagonal boron nitride and borophene. In 2017. he re-joined the Institute of Physics in Zagreb as a research associate, where he is currently employed. 2D materials remained in the focus of his research, where the investigations of physical and chemical properties are being complemented by efforts to exploit 2D materials in future technologies. Up to now, dr. sc. Petrović has published 27 scientific papers indexed in the Web of Science database (606 citations, h-index 11), has given ten invited talks and seminars at domestic and international conferences/institutions, and has been a team member on more than dozen scientific projects.

Acknowledgements

For a start, I would like to express my sincere gratitude to my mentor Marin Petrović for his support and guidance in my research. Secondly, I would like to thank Marko Kralj for his leadership from the first day I joined the Institute of Physics. I want to express my gratitude to Nataša Vujičić and Ana Senkić for their support and help with optical characterisations, Sherif Kamal for UHV analysis of borophene samples, Borna Pielić for UHV analysis of graphene samples, and Dino Novko for his DFT calculations. Also, I would like to acknowledge all other colleges in a group that passed their knowledge to me and helped to shape my research and myself. Last but not least, I would especially thank my college, Valentino Jadriško, for his friendship and proficiency that helped me on many occasions and situations we faced.

I would like to give special thanks to Rudolph Bratschitsch for the opportunity to visit the University of Munster and work with his group, from which I would like to thank Iris Niehues for support in absorbance characterisation. Also, I would like to give special thanks to Andres Castellanos Gomez for the opportunity to visit the Material science Institute in Madrid and work with his group, from which I would like to thank Onur Çakıroğlu for the construction of the three-point bending stage.

Finally, I am most grateful to my parents Vjeran and Ljiljana, sister Nika, girlfriend Matija, and all other friends who provided me with a productive environment full of love, faith, and care that helped me overcome all faced obstacles.

Short summary

Present-day flexible and stretchable electronic devices, such as bendable phones or displays, are mostly built from rigid microscopic components (sensors and transistors), where rigidity ultimately sets limitations to the devices' mechanics and performances. Due to their atomically thin nature, 2D materials (2DMs) exhibit impressive mechanical attributes which offer, in conjunction with the tunability of their other properties, significant advancements of the next generation of flexible devices. Although there is a massive interest in 2DMs and their applications, many steps are still needed to fully exploit 2DMs for flexible and stretchable devices.

Within this thesis, we have investigated MoS_2, borophene, and graphene monolayers as well as MoS_2/graphene heterostructures in view of flexible devices. Different segments which are required for the understanding of physical properties and device implementation of these materials have been investigated. For borophene and heterostructures of MoS_2/graphene, the focus was on mechanical manipulation. Graphene monolayers were mainly used for testing of the transfer and transport methods. MoS_2 monolayers and respective devices, as the most advanced systems we constructed, constitute the basis of strain-dependent measurements in our work.

More specifically, the first part of our research was dedicated to different device fabrication procedures in order to determine the optimum type of 2DM growth, sample morphology, and method of transfer. In this effort, several experimental techniques have been used: AFM, SEM, Raman and PL spectroscopy, and transport measurements. Large-scale monolayers (>100 μm) proved to be advantageous over smaller isolated flakes. Mechanical stamping method and electrochemical delamination yielded good results for the transfer of 2DMs from the growth substrates to arbitrary ones, with minimum contaminations or damage. E-beam and stencil lithography were used on both rigid and flexible substrates for the fabrication of electrodes of the 2DM-based devices.

In the second part of the thesis, strain-dependent measurements with uniaxial bending were conducted, thus enabling the investigation of tensile strain on devices' performances. For example, our devices did not show any degradation in terms of electrical resistance even after 40 bending cycles at strain values as high as 1%. Also, the photoresponse of MoS_2 can be significantly enhanced by the application of strain, where the increase of photocurrent and broadening of spectral sensitivity have been found. Additionally, we have shown that on

encapsulated devices strain has uniformly propagated over the whole surface of 2DMs, while with a transfer of 2DMs on pre-fabricated electrodes, the electrodes are a source of inhomogeneous strain distribution within the 2DM.

Overall, the research presented in this thesis provides a new insight into the physical phenomena behind the synthesis and manipulation of 2DMs, and can serve as a guideline for the fabrication of novel devices based on 2DMs. In line with this, the conducted strain-dependent characterisation brings unique properties of 2DMs closer to real-life applications.

Keywords: 2D materials, transition metal dichalcogenides, MoS_2, borophene, graphene, electrochemical transfer, PDMS transfer, lithography, scanning electron microscopy, atomic force microscopy, Raman spectroscopy, photoluminescence spectroscopy, photocurrent spectroscopy, field effect transistors, uniaxial tensile strain, bending, gauge factor, flexible electronics, photodetectors, strain sensors

Sažetak

2D materijali (2DM-i) su atomski tanki sistemi koji posjeduju impresivna i jedinstvena svojstva. 2DM-i su jedni od istaknutijih kandidata za izradu mnogih elektroničkih uređaja koji se mogu savijati i rastezati ili mehanički deformirati u nekom drugom obliku. Trenutno dostupni fleksibilni elektronički uređaji, poput savitljivih telefona, bazirani su na pozicioniranju i arhitekturi rigidnih komponenti (senzora i tranzistora) koje još uvijek limitiraju performanse i mehanička svojstva uređaja. S druge strane, upotreba 2DM-a za takve komponente omogućava puno veću razinu fizičke deformacije konačnih uređaja. Dodatno zbog širokog spektra mogućnosti modificiranja ostalih svojstava, iskorištavanje 2DM-a omogućuje napredak nove generacije fleksibilne elektronike u područjima kao što su nosivi senzori, personalizirana medicina, savitljivi mobiteli i ekrani, IoT (Internet stvari) te pretvorba i pohrana energije.

Unatoč velikom interesu za 2DM-e i njihove primjene, još uvijek je potrebno provesti mnogo koraka prije njihovog potpunog iskorištavanja za komercijalne fleksibilne i rastezljive uređaje. U sklopu ove teze, istražili smo neke od ključnih koraka za primjenu MoS_2 (molibden disulfid), borofen (Bo) i grafen (Gr) jednosloja (eng. *monolayer*) te MoS_2/Gr heterostrukture za fleksibilne komponente uređaja (dalje „fleksibilni uređaji“). Prvo su 2DM-i okarakterizirani nakon sinteze kako bi se utvrdila svojstva materijala kod izlaganja ambijentalnim uvjetima, nakon čega su transferirani na podloge pogodne za izradu uređaja i mjerenja različitih svojstava u ovisnosti o naprezanju. Kako bi se odredile optimalne metode i parametri transfera, istražena su optička i transportna svojstva te površinska morfologija 2DM-a prije i poslije mehaničke manipulacije (transfera ili izrade uređaja). U konačnici, MoS_2 jednosloji su iskorišteni za izradu fleksibilnih uređaja koji su okarakterizirani prateći promjene otpora, fotostruje i ekscitonskih energija prilikom naprezanja.

Specifičnije, u prvom poglavlju teze napravljen je opći uvod o 2DM-ima, utjecaju naprezanja na njihova svojstva te pregled fleksibilne elektronike. Prikazana su dostignuća u područjima sinteze, modifikaciji svojstava te mehaničkoj manipulaciji i uređajima baziranim na MoS_2, Gr, Bo i njihovim heterostrukturama. Potom su predstavljene mogućnosti modifikacije svojstava 2DM-a naprezanjem te metode unosa naprezanja u 2DM-e. Nadalje, napravljen je kratki povijesni pregled područja fleksibilne elektronike, s naglaskom na nedostatke prethodnih materijala koje nadomještavaju do sada ostvareni fleksibilni uređaji na bazi 2DM-a. Na kraju prvog poglavlja, izneseni su ciljevi provedenoga istraživanja u sklopu ove teze.

U drugom poglavlju su predstavljene eksperimentalne metode i postavi korišteni u sklopu našeg istraživanja. Uvedene su metode sinteze 2DM-a kao i postavi korišteni za izradu uređaja na bazi 2DM-a. Potom, objašnjene su metode i postavi karakterizacije 2DM-a i uređaja baziranih na njima, najprije je istražena morfologija površina pa zatim optička i transportna karakterizacija. Naposljetku, prikazani su postavi za savijanje, korišteni za primjenu naprezanja u mjerenjima u ovisnosti o naprezanja.

Treće poglavlje posvećeno je detaljnom opisu rezultata konstrukcije uređaja temeljenih na 2DM-ima, ostvarenih pomoću transfera i litografije. Mehanička manipulacija potrebna je nakon sinteze 2DM-a budući da su podloge korištene za rast nepogodne za tehnološko iskorištavanje materijala i unos naprezanja. Stoga su za transfer 2DM-a izrađena dva postava, elektrokemijski transfer za metalne substrate te PDMS transfer za Si wafere. Za izradu elektrodi, potrebnih za mjerenje električnih veličina kod uređaja na bazi 2DM-a, korištene su stencil te e-beam litografija. Parametri za svaku metodu transfera i litografije detaljno su istraženi u svrhu optimizacije za svaku pojedinu kombinaciju 2DM-a i substrata.

U sljedećem, četvrtom, poglavlju iznesene su karakterizacije Bo, Gr i MoS_2 jednosloja te MoS_2/Gr heterostrukture bez primjene naprezanja. Napravljena je detaljna studija njihovih svojstava u ambijentalnim uvjetima kako bi se odredilo koji su materijali, i u kojoj formi, najpogodniji za izradu senzora i tranzistora. 2DM-i su prvotno okarakterizirani na substratima na kojima su sintetizirani te kasnije na onima na koje su transferirani. Morfologija površine 2DM-a određena je skenirajućim elektronskim mikroskopom (SEM-om) i mikroskopom atomskih sila (AFM-om) dok su optička svojstva istražena Raman i fotoluminiscencijskom (PL) spektroskopijom. Prvo su predstavljeni napreci ostvareni za jedan od recentnijih 2DM-a, Bo, gdje je fokus bio na stabilnost u ambijentalnim uvjetima i uspješnoj mehaničkoj manipulaciji. Potom, izneseni su rezultati istraživanja Gr jednosloja koji je služio kao testni materijal za izrađene eksperimentalne postave te kao podloga za kompleksnije MoS_2/Gr heterostrkture. U konačnici, detaljno su analizirana svojstva MoS_2 u ambijentalnim uvijetima poslije sinteze i transfera. Ispitani su efekti fotodopiranja (eng. *photodoping*) i dopiranja električnim poljem (eng. *electric field doping*) na optička svojstva, konkretno na energije ekscitona i triona određenih PL spektroskopijom. Naposljetku, izneseni su rezultati karakterizacije vodljivosti i mobilnosti konstruiranih FET (eng. *field effect transistor*) tranzistora na bazi MoS_2.

Peto poglavlje se sastoji od rezultata karakterizacije svojstava MoS_2 u ovisnosti o naprezanju, i to za jednoslojeve s lateralnim veličinama preko 1 mm sintetizirane CVD (eng. *chemical vapor deposition*) metodom. Na samom početku predstavljena je analiza prijenosa naprezanja preko pukotina i granica zrna MoS_2–a, smještenog između substrata polikarbonata (PC-a) te polydimethylsiloxana (PDMS-a). Pomoću apsorbcijske spektroskopije određeni su gauge faktori ($GF_{A/B}$) za ekscitonske energije na različitim razinama naprezanja unesenih pomoću nosača za savijanje s dvije točke (eng. *2-point bending stage*). Nakon toga opisana je analiza jednosloja MoS_2-a transferiranog na PC substrat s Au elektrodama, s ciljem utvrđivanja mogućnosti korištenja takve konfiguracije za senzore naprezanja ili pritiska. Morfologija uzorka određena je AFM-om dok je kontinuiranom karakterizacijom MoS_2 senzora ispitana funkcionalnost i reproducibilnost promjene otpora uzorkovanih primjenom jednoosnog vlačnog naprezanja. Naprezanje je primjenjivano tokom ~ 60 sati odnosno 20 ciklusa do iznosa od 0.6% pomoću nosača za savijanje u tri točke (eng. *3-point bending stage*). Potom, interpretirani su rezultati karakterizacije MoS_2 fotodetektora pomoću spektroskopije fotostrujom (eng. *photocurrent spectroscopy*) prilikom naprezanja uzorka i to u istoj konfiguraciji i s jednakim nosačem korištenim za prethodnu analizu MoS_2 senzora naprezanja. Prilikom čega je ostvareno trostruko povećanje fotostruje kod naprezanja od 0.9 %. Na kraju poglavlja, pomoću analize promjena pozicija ekscitonskih energija u spektroskopskim PL mapama iznesena je karakterizacija lokalnih prostornih varijacija naprezanja MoS_2 unesenih morfologijom substrata i dodatno nosačem za savijanje.

Istraživanje provedeno u sklopu ove teze predstavlja nove uvide u fizikalne fenomene u pozadini sinteze i manipulacije 2DM-a, koji mogu služiti kao smjernice za izradu novih uređaja na bazi 2DM-a. Konkretno, pokazali smo kako elektrokemijski transfer može biti korišten za mehaničku manipulaciju osjetljivih materijala poput Bo te kompleksnih materijala poput MoS_2/Gr heterostrukture. Nakon toga detaljno smo istražili svojstva MoS_2 te demonstrirali kako se PDMS transfer te stencil i e-beam litografija mogu primijeniti za konstrukciju uređaja na bazi 2DM-a. Dodatno smo pokazali kako se sa raznim dopiranjima može utjecati na energije kvazičestica te da se MoS_2 može iskoristiti za FET-ove na Si waferima. Poseban naglasak u istraživanju stavljen je na karakterizaciju izrađenih fleksibilnih uređaja MoS_2-a u ovisnosti o naprezanju. Utvrdili smo da granice zrna ne sputavaju prijenos naprezanja unutar *large-scale* 2DM-a, zatim kako se MoS_2 može iskoristiti za fleksibilne senzore naprezanja i pritiska te u konačnici da se primjenom naprezanja mogu poboljšati performanse fleksibilnih fotodetektora na bazi MoS_2. Ostvareni rezultati značajno približavaju iskorištavanje jedinstvenih svojstava

2DM-a za svakodnevne uređaje otporne na drastične mehaničke deformacije poput rastezanja i savijanja.

List of commonly used acronyms

2D – Two dimensional

2DM – 2D materials

AFM – Atomic force microscope

SEM – Scanning electron microscope

PL – Photoluminescence

FET – Field effect transistor

Bo – Borophene

Gr – Graphene

MoS_2 – Molybdenum disulfide

TMD – Transition metal dichalcogenide

GF – Gauge Factor

PC – Polycarbonate

PDMS – Polydimethylsiloxane

PMMA – Poly(methyl methacrylate)

Si – Silicon

IFZg – Institute of Physics in Zagreb

UHV – Ultra-high vacuum

Contents

Acknowledgements ..... **iii**

Short summary ..... **v**

Sažetak ..... **vii**

List of commonly used acronyms ..... **xi**

1. Introduction **1**

1.1. 2D materials *1*

1.2. Strain application in 2D materials *10*

1.3. Flexible electronics *15*

1.4. Objectives *20*

2. Methods and experimental setups **21**

2.1. Synthesis of 2D materials *22*
2.1.1. CVD in an inert atmosphere 22
2.1.2. CVD in UHV 24
2.1.3. MBE in UHV 27

2.2. Device fabrication *29*
2.2.1. Transfer methods 29
2.2.2. Lithography 30

2.3. Morphology characterisation *32*
2.3.1. SEM 32
2.3.2. AFM 34

2.4. Optical spectroscopy *35*
2.4.1. Raman spectroscopy 35
2.4.2. Photoluminescence spectroscopy 37
2.4.3. Absorbance spectroscopy 37
2.4.4. Micro-reflection spectroscopy 38

2.5. Transport characterisation *38*
2.5.1. Resistance 38
2.5.2. Photocurrent setup 39
2.5.3. FET 40

2.6. Setups for application of strain *42*
2.6.1. Two-point bending stage 42
2.6.2. Three-point bending stage 43

3. Fabrication of devices based on 2D materials **46**

3.1. Transfer *46*
3.1.1. Stamping transfer 46
3.1.2. Electrochemical transfer 50

3.2. Lithography *54*

3.2.1. Stencil lithography 54
3.2.2. E-beam lithography 56

4. Characterisation prior to strain application **60**

4.1. Bo *60*
4.1.1. Bo on Ir (111) 60
4.1.2. Bo on Si/SiO_2 wafer 63
4.1.3. Raman spectroscopy of Bo 67

4.2. Gr and MoS_2/Gr heterostructure *70*
4.2.1. Gr 70
4.2.2. MoS_2/Gr heterostructure 73

4.3. MoS_2 ..... *76*
4.3.1. MoS_2 morphology 76
4.3.2. PL of MoS_2 80
4.3.3. MoS_2-based FET 83

5. Strain-dependent device characterisation **86**

5.1. Absorbance *86*

5.2. Resistance *91*

5.3. Photocurrent *96*

5.4. Photoluminescence *101*

6. Conclusion **105**

References **111**

Curriculum vitae **123**

Chapter 1

Introduction

2D materials (2DMs) are atomically thin materials that exhibit very interesting and often unsurpassed combinations of properties. They present a promising platform for the fabrication of many electronic devices that could be bent, stretched, rolled, or in any other way deformed. First, we give an overview of research on 2DMs, especially graphene (Gr), borophene (Bo), and molybdenum disulfide (MoS_2), which were investigated in our work. Progress on their synthesis, tunability of their properties, mechanical manipulation, and device fabrication and characterisation are reviewed. Next, 2DMs we display methods of strain application in 2DMs for strain-dependent characterisations and modifications of their properties and devices based on them. Afterward, we show state-of-the-art in the flexible electronics field and why 2DMs are prominent candidates for bendable and stretchable devices, followed by a detailed overview of previously exhibited flexible devices based on. In the end, we disclose the goals of our research that were aimed throughout this thesis.

1.1. 2D materials

The discovery of Gr (graphene) had a significant impact on the scientific community because 2DMs (2D materials) were not expected to be energetically stable, and they exhibited novel combination of properties that showed a promising future in view of various applications.[1]

Essential for many exceptional properties is Gr structure, depicted in **Figure 1(a)**, consisting of carbon atoms arranged in a 2D hexagonal lattice, with two atoms in the unit cell constituting a honeycomb structure. As a result, Gr can be regarded as a crystal consisting of two hexagonal lattices shifted with respect to each other. The honeycomb structure results from three sp^2 hybrid orbitals, formed by linearly combining 2s, $2p_x$, and $2p_y$ carbon orbitals (which all lie in the same plane with a 120° angle). σ-bonds are formed from sp^2 orbitals on neighboring C-C atoms, with a distance of 1.42 Å.[2] The reciprocal lattice of Gr with the first Brillouin zone (BZ) and high symmetry points (Γ, M, K, K') is shown in **Figure 1(a)** on the right side. There are two nonequivalent neighboring points in the corners of the BZ, K and K', since one cannot

use unit vectors b_1 and b_2 to translate from the K point to the K' point, which exhibits Dirac cones, as shown in **Figure 1(b)**. As there are two atoms in the basis of a Gr unit cell, the electron wave functions can be described by two components (i.e., spin orientation). Moreover, the dispersion in the vicinity of these points is linear, due to which electrons near the K and K' points can be described by the Dirac equation for massless particles and the corresponding electronic states constitute so-called Dirac cones in the *k*–space.[2] Gr electronic structure governed by Dirac fermions is an interesting mix of a semiconductor (zero density of states) and a metal (zero bandgap), making it a semi-metal. The electrons in Gr seem to be almost insensitive to disorder and electron-electron interactions and have very long mean free paths. Hence, Gr's properties differ from those of usual metals and semiconductors. Gr also has a robust but flexible structure with unusual phonon modes that do not exist in ordinary 3D solids.[2] As seen in **Figure 1(c)**, the two most intense Gr's Raman spectra features are the G peak at 1580 cm^{-1} and a 2D band at 2700 cm^{-1}, historically named G', since it is the second most prominent peak always observed in graphite samples.[3] The G peak arises from the doubly degenerate zone center E_{2g} mode, while the 2D peak is a two-phonon resonance second-order Raman peak. G peak, caused by in-layer transverse vibrations of sp_2 hybridized carbon atoms, is dependent on the number of layers of Gr sheets and is vulnerable to stress and susceptible to doping. The double resonance process connection phonon wave vector and the electronic band make the frequency of the 2D peak susceptible to the excitation wavelength. Since zone-boundary phonons do not satisfy the Raman fundamental selection rule, they are not seen in first order Raman spectra of defect-free Gr. Such phonons give rise to a peak at 1350 cm^{-1} in defected Gr, called the D peak.[3,4]

The unique band configuration of the Dirac point gives Gr excellent conductivity and ambipolar electric field effect, which is reflected in the symmetric shape of the $\sigma-V_G$ curve, as seen in **Figure 1(d)**. In other words, charge carriers can be continuously tuned between electrons and holes, and current conduction is independent of the type of carriers.[5] Also, charge carrier concentrations as high as 10^{13} cm^{-2} can be achieved by gating in Gr pass through the barrier with 100% probability. Due to a strong force between the carbon atoms, the collision of carbon atoms has little effect on the motion of electrons, resulting in high mobility with ballistic tranport, as seen in **Figure 1(e)**. The carrier mobility of Gr placed on a SiO_2 wafer could reach $\mu = 10^6$ cm^2 V^{-1} s^{-1}, while the Gr conductivity can reach 10^6 Sm^{-1} and zero Schottky contact barrier.[2,6] Electronic properties in combination with mechanical robustness on nm scale resulted

in high-performance devices and massive interest in Gr as a replacement for silicon (Si) used for present electronics.[5]

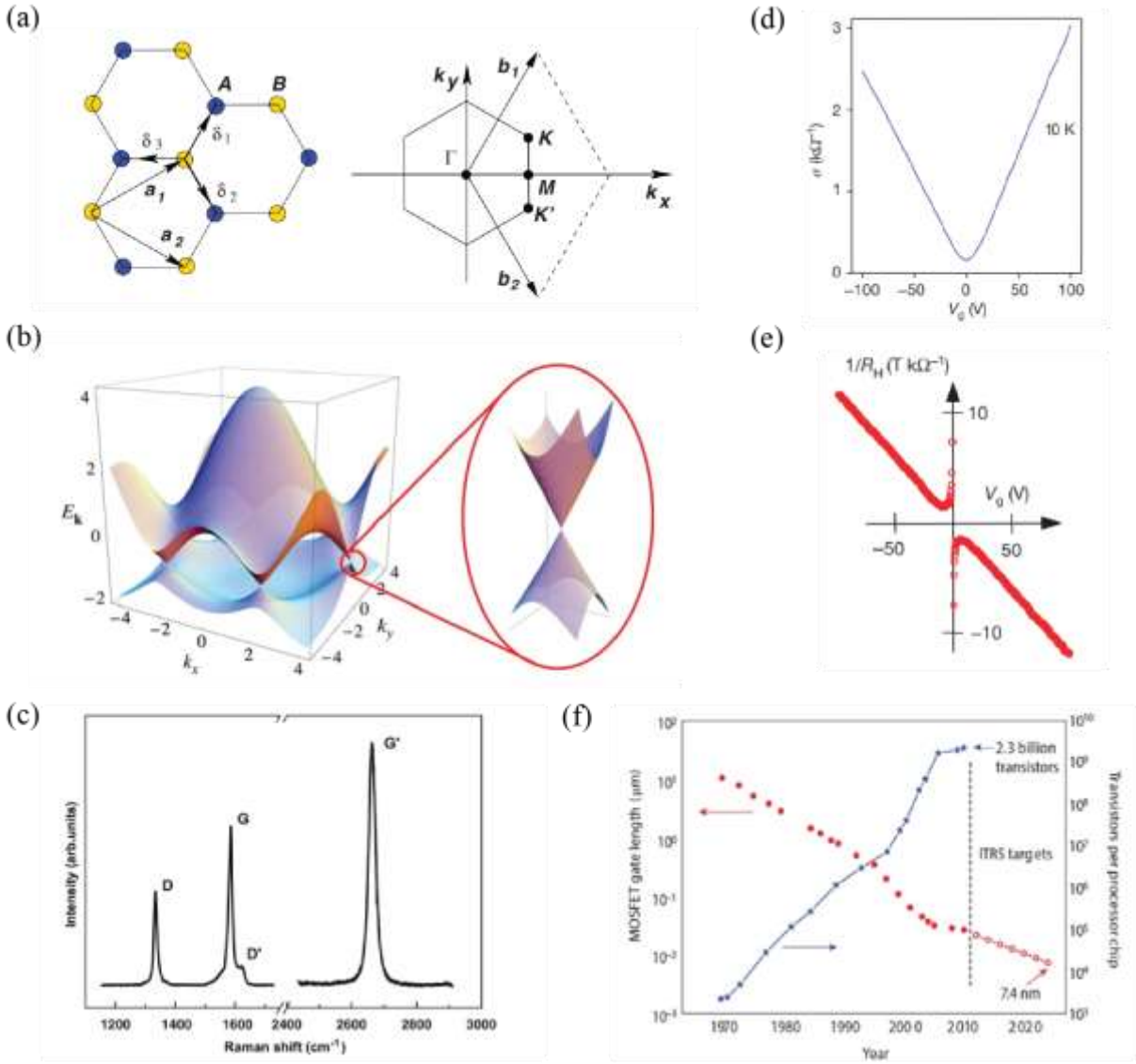

Figure 1. *Gr structure and properties with field effect transistor (FET) potential. (a) Honeycomb lattice and its Brillouin zone. Left: lattice structure of Gr, made out of two interpenetrating triangular lattices, with a_1 and a_2 as the lattice unit vectors, and δ_i, i= 1, 2, 3 the nearest-neighbor vectors. Right: corresponding Brillouin zone. The Dirac cones are located at the K and K' points. (b) Electronic dispersion in the honeycomb lattice. Left: energy spectrum. Right: zoom-in of the energy bands close to one of the Dirac points. (c) Raman spectrum of Gr monolayer. (d) Changes in Gr's conductivity by the gate voltage. (e) Gr hall coefficient for mobility determination. (f)MOSFET gate length in production-stage integrated circuits (filled red circles) and International Technology Roadmap for Semiconductors (ITRS) targets (open red circles). As gate lengths decrease, the number of transistors per chip (blue stars) increases, following Moore's law.[Adopted from Ref.* [2,3,5,7]*].*

As shown in **Figure 1(f)**, the physical dimensions of transistors play a crucial role in chip performance. As gate and channel lengths decrease, it is possible to place more individual transistors in the same area, enabling the complexity of the integrated circuit and leading to significant improvements in performance and decreases in price per transistor.[8] In several decades of the semiconductor industry, each production series increased the number of chips and their performance according to Moore's law and Dennard's rule.[8,9] However, with scaling of device parameters to nm sizes and atomic level, Si-based technology faces problems due to quantum effects and increased leakage current preventing the proper functionality with standard materials and configurations. In contrast, Gr and 2DMs flourish on nm scales and present a possible exchange for silicon (Si) and present-day electronic devices.[5] Due to Gr's semi-metallic nature, significant effort was made for the experimental opening of bandgap from chemical and molecular doping to patterning and functionalizing substrate.[10–13] But none of the realized processes showed results that succeeded in opening the large enough gap while keeping the process sufficiently simple in a way to make it applicable in the industry.[14]

Although Gr itself did not meet the expectations in the view of transistors, , new classes of 2DMs were experimentally realized since Gr's discovery, which broadened the spectrum of possible applications.[15,16] Few thousand of new 2DMs were studied, each having considerably different properties.[17] From insulators such as hexagonal boron nitride (hBN) to semiconductors as MoS_2 and metallic ones as Bo. Each material has other particular properties in addition to different transport properties. As illustrated in **Figure 2(a)**, 2DM's properties vary not only between each other but also within the same material, depending on the number of layers, lateral sizes, phases or type and number of defects.[18] Possibilities expand even more if different 2DMs are combined mutually to form heterostructure material, as shown in **Figure 2(b)**. Heterostructures can be constructed, either by a sequential growth or with the mechanical transfer of 2DMs, with custom properties depending on application requirements.[19]

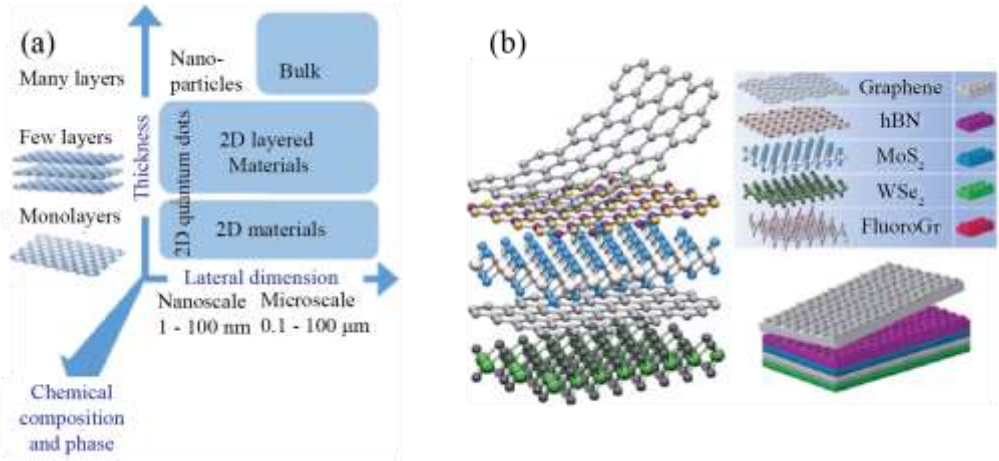

***Figure 2**. 2DMs after Gr. (a) Morphology (thickness and lateral dimension) with chemical composition and phase determine 2DM properties. [Adopted from Ref. [20]]. (b) 2DMs can be used as building elements for heterostructures with custom-made properties. [Adopted from Ref. [21]].*

After Gr, most investigated are layered 2D transition metal dichalcogenides (TMDs) such as MoS_2. They consist of transition metal atoms between two dichalcogenide atoms, one above and one below, as depicted in **Figure 3(a)**. Covalent bonds connect S and Mo inside the monolayer, while layers interact with relatively weak van der Waals forces in multilayers. As a result of covalent bonds, there are no intrinsic dangling bonds; however, they can exist if defects, such as sulphur vacancies, are present in the crystal.[22] In contrast to Gr, the MoS_2 monolayer has a bandgap of 1.8 eV. Calculated band structures of MoS_2 (from bulk to monolayer) are shown in **Figure 3(d)**, where solid arrows indicate the lowest energy transitions. It can be seen that at the K point, MoS_2 has a direct transition in contrast to indirect one for multilayers and bulk form.[23] Excitons are neutrally charged electron-hole pairs and their behavior can be investigated by photoluminescence (PL) and absorbance spectroscopy. There are two characteristic peaks for MoS_2 monolayer at 670 nm and 627 nm that are signatures of two excitons (A and B) associated with the energy split from valence band spin-orbit coupling, as depicted in **Figure 3(e)**.[23] If an additional electron or hole gets bound on exciton, as illustrated in **Figure 3(f)**, a charged quasiparticle called trion is formed.[24] Optically generated electron−hole pairs in monolayer MoS_2 form stable exciton states even at room temperature because of the substantial Coulomb interactions in 2DMs. Due to quantum confinement effects in 2DMs, reduced dielectric charge screening promotes stronger excitonic interactions.[25]. As a result, MoS_2 photoluminescence from a monolayer is the strongest, whereas it is absent in bulk

material.[23] This is because MoS_2 is indirect bandgap material in its bulk form, while in contrast, the monolayer form becomes a direct bandgap semiconductor with a 2.1 eV gap.[26]

In an abundance of desirable characteristics, MoS_2 properties can be tuned additionally by many methods, for instance, an electric field, external force or chemical and different types of dopings as the MoS_2 monolayer is susceptible to various chemical compounds or molecules.[27,28] FETs based on MoS_2 monolayers, with the configuration shown in **Figure 3(b)**, achieved mobility higher than 200 $cm^2 V^{-1} S^{-1}$ and a 10^8 on/off ratio.[29] While MoS_2 photodetectors, with the configuration shown in **Figure 3(c)**, exhibited 880 AW^{-1} photoresponsivity. which is better than Gr by a factor of 10^6.[30] Also, they have a broad spectral range from 680 nm to 400 nm and the possibility to be turned off with low dark current and signal-to-noise even lower than commercial state-of-the-art silicon avalanche photodiodes.[31]

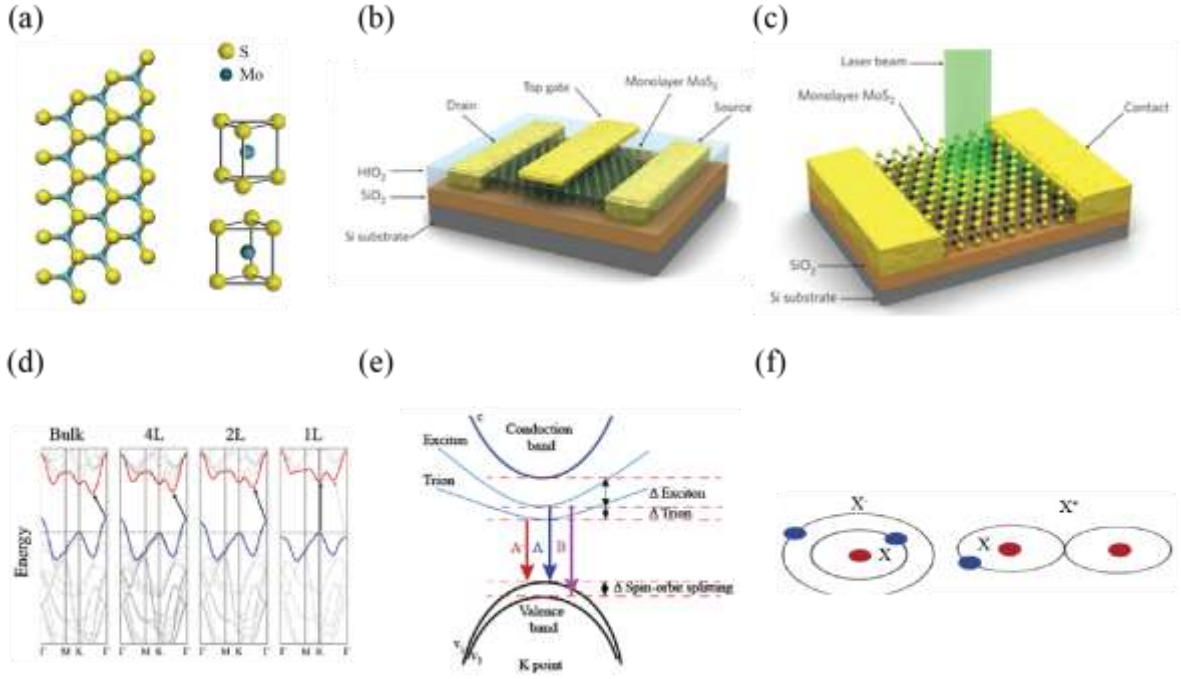

Figure 3. *Schematic of semiconducting MoS_2 monolayer, devices and properties. (a) Atomic structure of MoS_2, clearly showing the spatial inversion symmetry breaking in MoS_2 monolayer. [Adopted from Ref. [32]]. (b) FET based on MoS_2 monolayer.[Adopted from Ref. [29]]. (c) Photodetector based on MoS_2 monolayer. [Adopted from Ref. [30]]. (d) Calculated band structure of MoS_2 in dependence on layer number.[Adopted from Ref. [23]] (e) Schematic of Brillouin zone K point band structure and quasiparticle energy states in MoS_2 monolayer. (f) Charged quasiparticle trion is formed with an additional electron or hole bound on exciton. [Adopted from Ref. [24]].*

MoS_2 broadened the spectrum of possible applications of 2DMs on transistors, photodetectors and memory devices, with the possibility to integrate it with currently used Si-based technology or exploit it for flexible electronics.

Furthermore, MoS_2 can be combined with different 2DMs into heterostructures, for instance, the MoS_2/Gr, where nm-sized MoS_2 islands are grown directly over large-scale Gr layer. Such devices offer further possibilities as quantum photonics and optoelectronic devices, from top 2DM, while 2DM on bottom enables mechanical support of the heterostructure. For example, in small lateral-sized MoS_2, single-photon emission is possible due to quantum confinement in the grain boundaries and edges, which can be used as top 2DM.[33] At the same time, the bottom 2DM, such as Gr, provides the mechanical robustness necessary for large-scale applications.

One of the recently discovered 2DMs is borophene (Bo), an atomically thin sheet of boron atoms. Bo gained significant attention in recent years due to its exceptional physical and chemical properties, which are variable due to its polymorphic nature.[34,35] While examples can be found where the atomic structure is adopted from 3D bulk boron with triangle structure; most Bo polymorphs are composed of the two main building blocks, small triangles and hollow hexagons. The dominance of these two structural elements emerges from a competition of two- and three-center bonding caused by the inherent electron deficiency in boron.[36] Electronic properties of Bo are governed by the interplay and arrangement of these hollow hexagons in a lattice of triangles that compose a 2D sheet.[37] This opens pathways for customization of this unique 2DM. Most Bo polymorphs are expected to be metallic, making Bo the lightest 2D metal (as opposed to semimetals such as graphene and silicene or semiconductors such as phosphorene) while also exhibiting mechanical compliance and optical transparency, as shown in **Figure 4**.

So far, experimentally disclosed Bo devices were mainly focused on Bo composites and multilayer forms.[38] One of the main reasons is known Bo reactivity, especially affinity for oxygen bonding under ambient exposure.[39] However, in certain polymorphs, Bo can be stabilized by passivation; for instance, by hydrogenating Bo in ultra high vacuum (UHV), a combination of boron-hydrogen and boron-hydrogen-boron bonds can reduce Bo ambient oxidization.[40] Generally, researches published on Bo are theoretical papers and synthesis protocols for various polymorphs of Bo with in-situ characterisations. Synthesis efforts are often directed toward the large-scale Bo, aiming to bring Bo closer to the applications in, e.g., supercapacitors, flexible memory devices, photodetectors and batteries.[41–44]

Additionally, instead of vertically stacking 2DMs, their heterostructures can be achieved by lateral composits of 2DMs, either by stacking or chemical reactivity. Recent reports showed that MoS_2 can be combined with novel 2DMs, such as Bo to fabricate sensors that exceed individual 2DMs. For instance, the p–n junction of Bo–MoS_2 has ultrahigh humidity sensing characteristic, fast response, long life and can be strained without loss of functionality. Its sensitivity at a relative humidity (RH) of 97 % is as high as 15 500 %, which is more than 90 or 70 times higher than that of Bo or MoS_2 alone.[45]

Parallel to high-quality synthesis, an additional challenge for application development and device fabrication is manipulating and transferring Bo samples to arbitrary target substrates.[34,46] For example, Mazaheri et al. performed the transfer of CVD (chemical vapor deposition) grown Bo from the aluminum substrate to target Si substrates.[47] The transfer method consisted of poly(methyl methacrylate) (PMMA) spin coating and treatment of the sample in several liquid substances. This growth-transfer combination provided many isolated Bo sheets of different sizes, layer number and polymorphs. Chahal and co-workers extracted single-layer Bo sheets of dominantly only one polymorph from crystalline boron pieces and placed them on different insulating substrates.[48] However, lateral dimensions of the transferred monolayer flakes were in the sub-micrometer range.

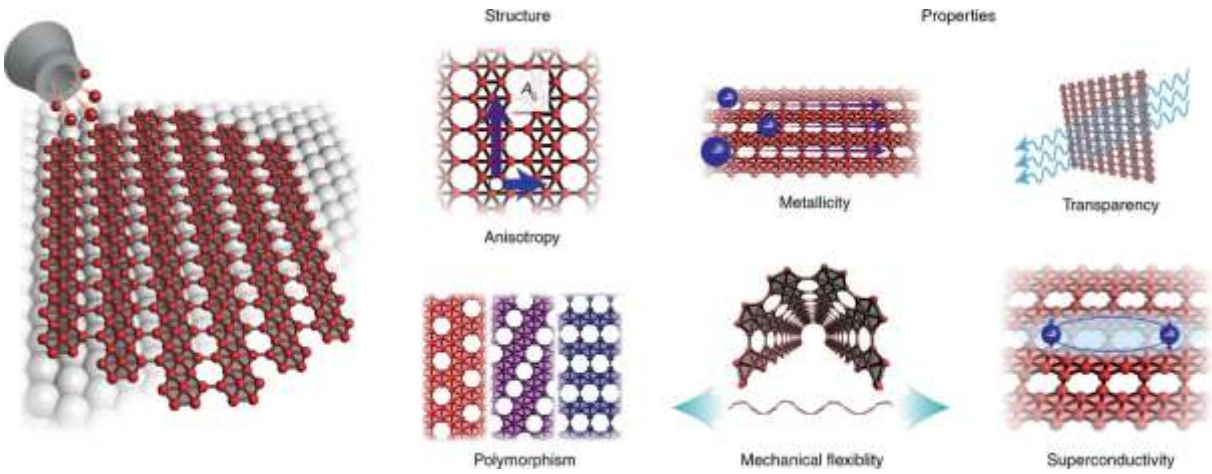

Figure 4. *Bo synthesized on a single-crystal surface through evaporation exhibits structural anisotropy (where Aij denotes a generic anisotropic property tensor component) and polymorphism, which results in a range of properties unique to 2DMs such as a combination of metallicity, mechanical flexibility, transparency, and superconductivity. [Adopted from Ref.* [49]*].*

The first experimental realization of 2DMs was achieved by mechanical exfoliation from bulk material.[1] Such method offers a simple and in principle, fast production method of

2DMs, but in parallel has few setbacks and limitations. Primarily, the samples obtained via mechanical exfoliation are limited to the micrometre range. The larger samples get the chance to have an inhomogeneous sample with areas containing bilayers or multilayer.[50] Similar methods such as liquid phase exfoliations bypass the problems with the size of the samples, but such methods are optimized for multilayer materials. Such techniques have the possibility for fast production, which in the future can provide large quantities of various 2DM s. However, inhomogeneity presents a significant setback for scientific research and explanations for a current development phase in which fundamental materials properties are still not apparent.[51]

Currently, most of the research regarding the 2DMs is directed at their scalability. Moreover, high-quality large-scale monolayers are the main requirement for the application of 2DMs. As previously discussed, defects present a major role in electronic and optical properties, and controlling them by synthesis is one of the essential requirements for maintaining the quality of the samples. Although the highest quality 2DMs are usually obtained via exfoliation from bulk, there was significant effort invested into different methods of laboratory synthesis of 2DMs. As part of that, many possibilities were developed for in-situ monitoring the growth process of 2DMs.[36,52–54] From many methods of synthesis, CVD and molecular beam epitaxy (MBE) are presented as the most beneficial for the growth of large-scale samples with adequate quality.[55–58] Notably, with those methods, the lateral size of the 2DM is only limited by the size of the substrate used.

The second major scalability issue is the transfer of 2DMs from the growth substrate to a new one required for a specific application.[16] For example, UHV growth usually implies metallic substrates, such as single-crystals and foils. While inert atmosphere growth usually involves an oxidized Si wafer or sapphire. [59–61] In both cases, a transfer is needed to integrate obtained 2DMs into different devices, especially in the case of flexible and stretchable devices. Various methods were applied to transfer 2DMs, and depending on the material and substrate combination, different approaches can present as more or less beneficial. For instance, an electrochemical transfer can be exploited for transfer from metallic substrates, while polydimethyldisiloxane (PDMS) transfer can be used for transfer from Si wafers.[62,63] Transfer methods consist of a pick-up step in which 2DM is removed from the growth substrate and a step in which 2DM is positioned on the new substrate. Processes can be all dry or include some liquid used to promote the transfer with different sorts of the assist layer in the process. [63–65] Substrates on which 2DMs are transferred can be with a clean surface, other 2DMs or structures patterned previously with any lithography. Although there is considerable progress in the

transfer of 2DMs, a couple of issues still need to be resolved. For instance, wrinkles and cracks, the bubbles at the interface between TMD and substrate and residues from the support layer can be found as the primary type of defects and transfer-induced damage.[66–68]

1.2. Strain application in 2D materials

To characterise 2DMs and devices based on them, many setups were developed for strain application with access to various characterisation techniques. As a result, experiments can be conducted with precise control of tensile or compressive strain in samples, while optical, transport or other characterisations can be performed simultaneously. In such a way, various 2DM devices can be tested, and the fundamental physical properties of 2DMs investigated. **Figure 5** shows examples of strain application and properties that can be investigated in dependence on the strain, such as carrier mobility, chemical reactivity, phonon response, and various phase transitions.[69] As shown first for Gr, 2DMs can sustain reversible tensile strain larger than 20%, which yields an exciting possibility to tune the properties of 2DMs by strain and thus opens a new field of "straintronics".[70]

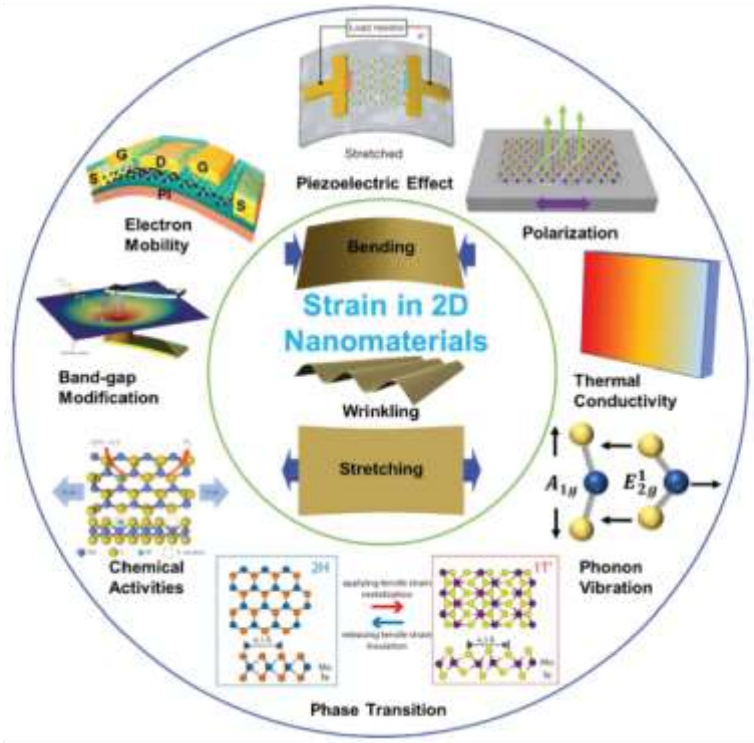

Figure 5. *Examples of strain application on 2DMs and their properties that can be examined. [Adopted from Ref. [69]].*

Generally, strain in 2DMs introduces changes in the bond lengths and angles, and in some cases, lattice deformations. These structure modifications significantly change the lattice vibrations,e.g. phonon frequency shift, detectable by Raman spectroscopy. When the uniaxial tensile strain is applied along the zigzag direction of MoS_2, the bond lengths along with the zigzag direction gradually increase with the strain, but the bonds along with the armchair direction decrease with strain, and further bond angle change, resulting in lattice distortion.[71,72] Even though uniaxial strain can induce deviations in Raman, biaxial strain results in much more drastic changes in Raman modes, especially for in-plane modes one strain values over 5%.[69,73]

In addition to crystal lattice change, bandgap tenability is the most dominant effect in strained 2D TMDs. For instance, Feng et al. reported that inhomogeneous strain could be exploited for creating a continuously varying bandgap profile in an initially homogeneous 2DM.[74] Furthermore, they showed that strain-engineered MoS_2 monolayer will capture a broad range of the solar spectrum and concentrate excitons or charge carriers.[74] The outputs of strain-dependent measurements are GFs (gauge factors) which show how much specific physical properties changed under 1% of strain. For instance, GFs for A and B excitons energy in MoS_2 monolayer (usually derived at GF_A=-37±1meV/%, GF_B=-34 ±1 meV/%) express how much the central position of exciton shifts for 1% of strain, as shown in **Figure 6(a)**.[75] Redshift of exciton positions is due to bandgap reduction with applied strain and funneling of photoexcited excitons towards higher strain regions.[71] Bandgap reduction is favorable for indirect transition, resulting in higher strain values and leading to change from direct to the indirect optical bandgap, seen in PL intensity reduction.[72] While GF for MoS_2 monolayer resistance (best reported GF_R=-148±19) shows how much resistance changes in the percentage of starting value for 1% of strain, as depicted in **Figure 6(b)**.[76,77] This observed piezoresistive behavior can be understood as band gap reduction under tensile strain. Thermally activated transport dominates in the subthreshold regime at room temperature, and the electrical current is carried by electrons thermally excited into the conduction band.[78] For 2DMs with an odd number of layers (one, three, five), inversion symmetry is broken, resulting in charge accumulation on the material's edges due to the strain's influence and piezoresponse.[77,79] Therefore, with the applied strain, conductance and valence band symmetrically reduce, leading to enhanced conductivity under strain.[76] The change of electronic structure and the bandgap cause inter-valley scattering and effective mass reduction, resulting in strain-enhanced FET mobility as previously reported.[80,81]

Furthermore, previous reports showed that the strain in MoS_2 can be exploited for selective enhancements on the adsorption of different gas molecules (enhanced adsorption of

NO and NH_3) while at the same time remaining insensitive to the adsorption of NO_2, CO, and CO_2. This contrasting behavior may lead to new design strategies for constructing ultrahigh-sensitivity sensors and electromechanical devices based on strain engineering of 2DMs.[82]

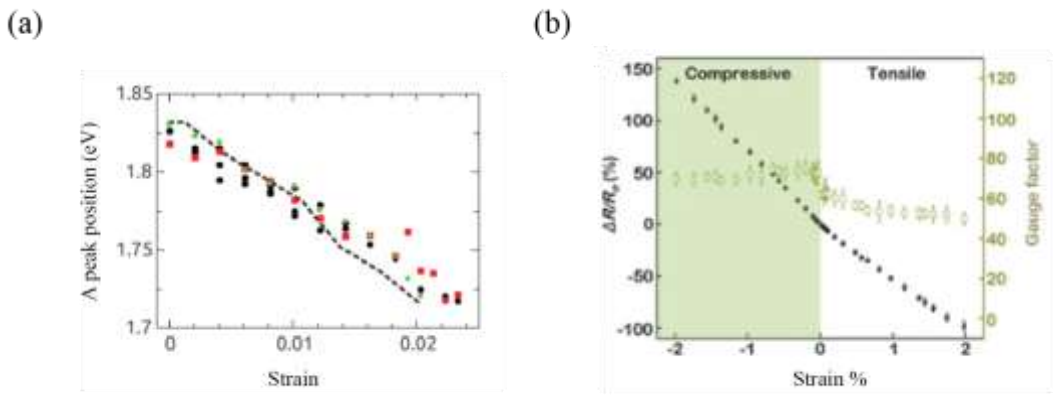

Figure 6. *Examples of Gauge factor determinations. (a) Position of A exciton peak GF. [Adopted from Ref. [71]]. (b) Resistance change GF. [Adopted from Ref. [76]].*

First reports on strain-engineering were on thermal expansion coefficient mismatch between the MoS_2 and the substrate, generated by a biaxial strain when the sample temperature was varied. However, the magnitude of the applied strain was modest with limited strain quantification.[83] Even though weak wan der Waals forces interact with the substrate, they are high enough to transfer strain from substrate to the 2DM for values more than 1-2%, while on higher values, sample topography can lead to slippage if no additional mechanism is applied for 2DM stabilization. As a result, many other mechanisms for strain application are designed and utilized to perform strain-dependant measurements, most with spatially homogenous and some inhomogeneous strains.

Application of strain can be divided into methods that use external force and methods that use patterned substrate. In both cases, strain is governed by the geometry and morphology of the sample. That can easily be determined with macroscopic samples and features, while for μm-sized or smaller ones, scanning probe microscopies (SPM) can be employed. With external force, uniaxial and biaxial homogeneous or local inhomogeneous strain can be induced in 2DMs.[69] Homogeneous strain can be induced by bending or stretching a substrate on which 2DMs or devices based on 2DMs are located. The sample is deformed along a single axis for the uniaxial strain, while for the biaxial is deformed along two axes. With biaxial configuration,

strain transfer from substrate to 2DM tends to be higher, which is visible in increased GF values, but those setups require more special stages and samples.[84]

Usually, deformation is achieved by controlling the position of two sample points with mechanical manipulators. At two-point bending, the substrate is bent by bringing its edges closer, as shown in **Figure 7(a)**. Depending on whether 2DM is at the top or bottom of the substrate, tensile or compressive strain is induced. In the three-point bending, the middle point of the substrate is fixed while edges are moved along the z-axis, causing the substrate to bend, as demonstrated in **Figure 7(b)**. With four-point bending, the edges of the substrate are fixed while two symmetric points between the edges and the middle are moved along the z-axis,

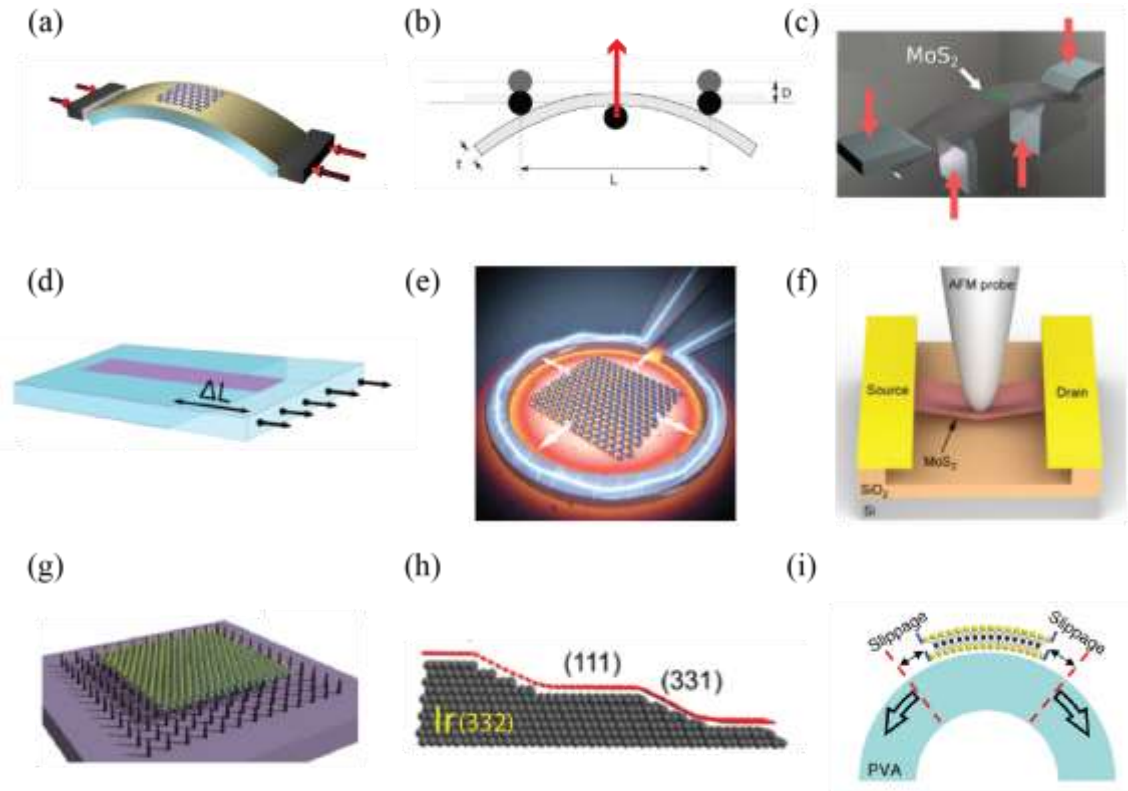

Figure 7. *Schematics of strain applications in 2DMs. (a) Two-point bending. [Adopted from Ref. [85]]. (b) Three-point bending. [Adopted from Ref. [75]]. (c) Four-point bending. [Adopted from Ref. [71]]. (d) Stretching by mechanical elongation stage. [Adopted from Ref. [86]]. (e) Stretching by thermal stage. [Adopted from Ref. [87]]. (f) Local inhomogenous strain induced by an AFM tip. [Adopted from Ref. [77]]. (g) 2DM transferred over patterned array of pillars. [Adopted from Ref. [88]]. (h) 2DM grown on stepped Ir(322) surface. [Adopted from Ref. [89]]. (i) Slippage of 2DM from substrate under strain. [Adopted from Ref. [90]].*

where 2DM can be located either on top or bottom for compressive or tensile strain, as illustrated in **Figure 7(c)**. If the edges of the sample are clamped physically, by increasing the separation of the clamps sample can be stretched, as depicted in **Figure 7(d)**.

Furthermore, in specially designed stages, the whole surface of 2DM can be controlled and strain induced, by stretching caused by thermal heating or piezoresponse, as shown in **Figure 7(e).** Inhomogenous strain can be induced by suspending the 2DM and deforming a single point of its surface, usually by atomic force microscope (AFM) or scanning tunnelling microscope (STM) tip, as demonstrated in **Figure 7(f).** With a patterned substrate, strain is induced by local deformation caused by the substrate morphology on which 2DM was transferred or synthesised. For example, 2DM can be transferred on a patterned substrate with structures (pillars, spheres, cones, etc.) that are usually fabricated from metals or polymers, as shown in **Figure 7(g)**. In some cases, 2DMs can be grown directly on patterned surfaces such as stepped Ir (332) single-crystal or modified Si wafer, as depicted in **Figure 7(h)**.

Even though setups are designed for homogeneous application of strain, due to the substrate or 2DM morphology and their adhesion, inhomogeneities of strain transfer from substrate to 2DM can arise. Previous studies on exfoliated TMD monolayers showed that the strain transfer is spatially-dependent due to edges of the 2DM. The highest amount of the strain is in the middle while it drops towards the edges of the flake.[91] For strain-dependent measurements with bending stages, strain is transferred by bending the substrate on which 2DM is located. In that way, strain is induced in the substrate, which transfers the strain towards the 2DM. Due to the weak van der Waals interaction of 2DM and the substrate, the chance for the slippage of 2DM, illustrated in **Figure 7(i)**, increases with higher amounts of strain.[91] Strain slippage is caused by strain variations over the surface of 2DM. With substrates having low Young modulus, those variations might increase locally with the applied strain, resulting in a higher chance for slippage. With smaller exfoliated flakes, the area where strain is adequately transferred gets decreased, and variations can cause slippage at minor amounts of the strain. In contrast, the larger the flake gets, the chance for the slippage should decrease. Additionally, by clamping the 2DM to the substrate either by side top encapsulation, side encapsulation or evaporating metal rods over 2DM, strain transfer can be enhanced and the chance for the slippage minimized.[71,90,92,93] Weak out-of-plane Wan der Waals forces may result in decoupling of the monolayer from the substrate or second layers in case of strain mismatch, which is exploited for 2DM exfoliation but at the same time presents a setback for strain utilization. As a result of in-plan covalent bonds and weak out-of-plane van der Waals bonds, the main

limitation for 2DM strain devices is not the mechanical properties of 2DM itself, instead, it is the device configuration that will govern which maximal strain values 2DM device can endure.

1.3. Flexible electronics

In recent decades, there has been a significant increase in the use of the term flexible electronics in scientific papers, as shown in **Figure 8**. The main reasons for such an increase ishigh interest in macroscopic devices that could be bent, rolled, stretched, and/or folded without losing functionality. With them, tremendous progress can be achieved in many high-tech areas, for example, in wearable sensors, personalized medicine, IoT (Internet of Things), novel smartphones and displays, and energy converters or storage.[94] Currently, commercially available macroscopic devices presented as flexible/stretchable are generally based on modifying the component architecture and not on the genuinely flexible/stretchable components. Instead, rigid components are positioned on low-strain areas of the macroscopic device.[94,95] For example, transistors, gyroscopes, photodetectors, and other sensors (building components of a mobile phone) are placed on the phone's edge where the strain induced by bending the phone is drastically lower than the middle, or similar strain-friendly configuration strategies are exploited.[96,97] Screen is usually built from organic semiconductors that showed suitability for usage in display devices. However, 2DMs and their composites are among the most prominent materials that could enable next-generation stretchable and flexible devices.[98,99]

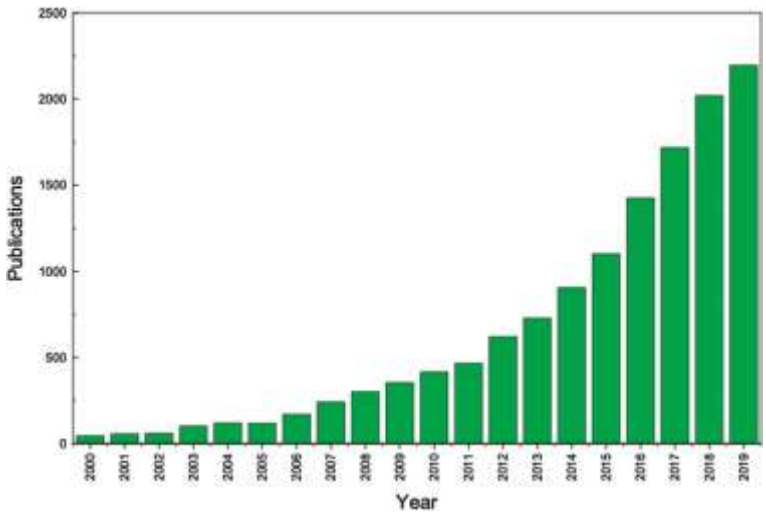

Figure 8. *The number of scientific papers that used the term "Flexible Electronics" on the Web of science, per year. [Adopted from Ref. [94]].*

Even though one might think that flexible electronics is a modern trend, such technology has roots more than 50 years back, as illustrated in **Figure 9**. A major milestone were thin metal films, that possessed for that time superior mechanical properties, with which first flexible transistors and solar cells were fabricated. However, a couple of decades were needed for significant progress of technology in some real-life applications. The progress was enabled by the discovery of conductive polymers, specifically organic semiconductors, with which flexible displays, photovoltaics and other sensor were constructed. Unfortunately, although many devices were constructed, devices based on organic semiconductors usually suffer from low performance and non-compatibility with standard fabrication technology. After them, other materials such as nanotubes and nanowires or new thin films were also investigated. However, similarly to organic semiconductors, their fabrication scale and low device yield limit their practical applications. Once the 2DMs were discovered, due to their appealing mechanical properties and abundance of different properties, the next generation of flexible electronic devices with intrinsically bendable and stretchable components has never been closer to real-life applications. [94,96]

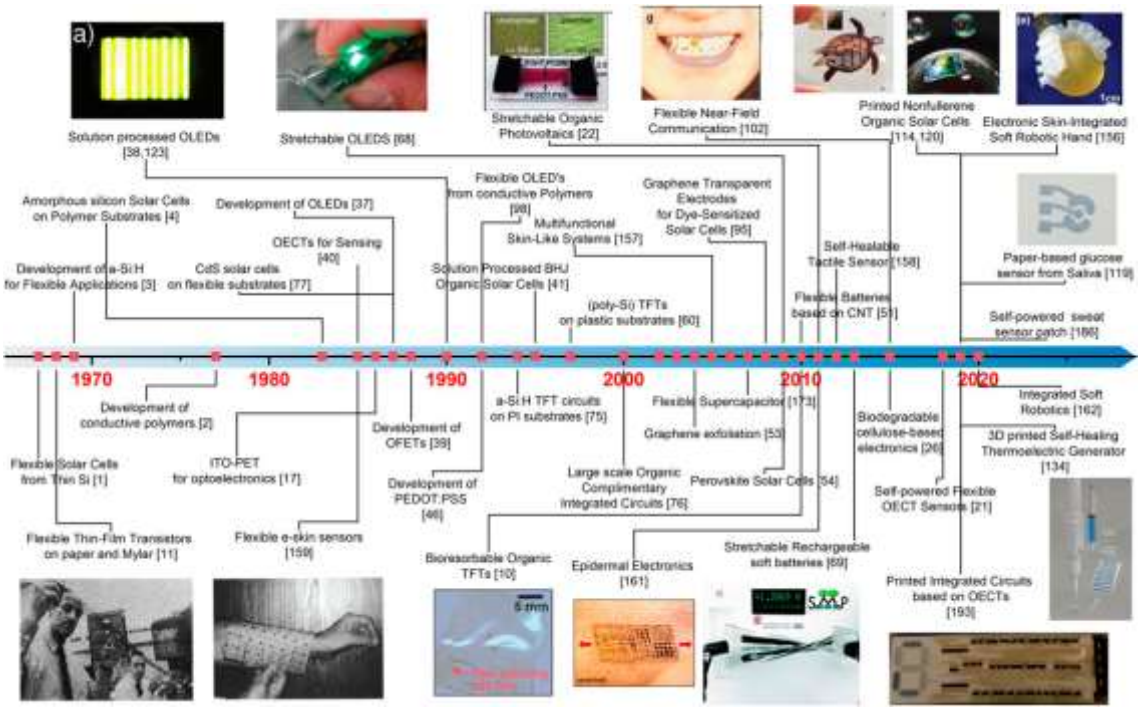

Figure 9. *Timeline of development in materials, processing and applications for flexible electronics. [Adopted from Ref. [94]].*

Modern-day technology is generally based on the electronic components which either passively or actively participate in complex devices. Those individual components are devices such as transistors, capacitors, or sensors. Mainly they operate by measuring voltage, current

or capacitance via pairs of electrodes.[100–102] Depending on the application, electrodes can be fabricated with arbitrary configuration and dimensions.[103] Some devices do not use electrodes or electric signals for processing and sensing. For example, photodetectors are generally based on transformation from photons to electronic signals with photovoltaics. However, they can also be based only on optical properties without exploitation of electrodes, such as monitoring the change of Raman or PL signal under different environments.[104,105]

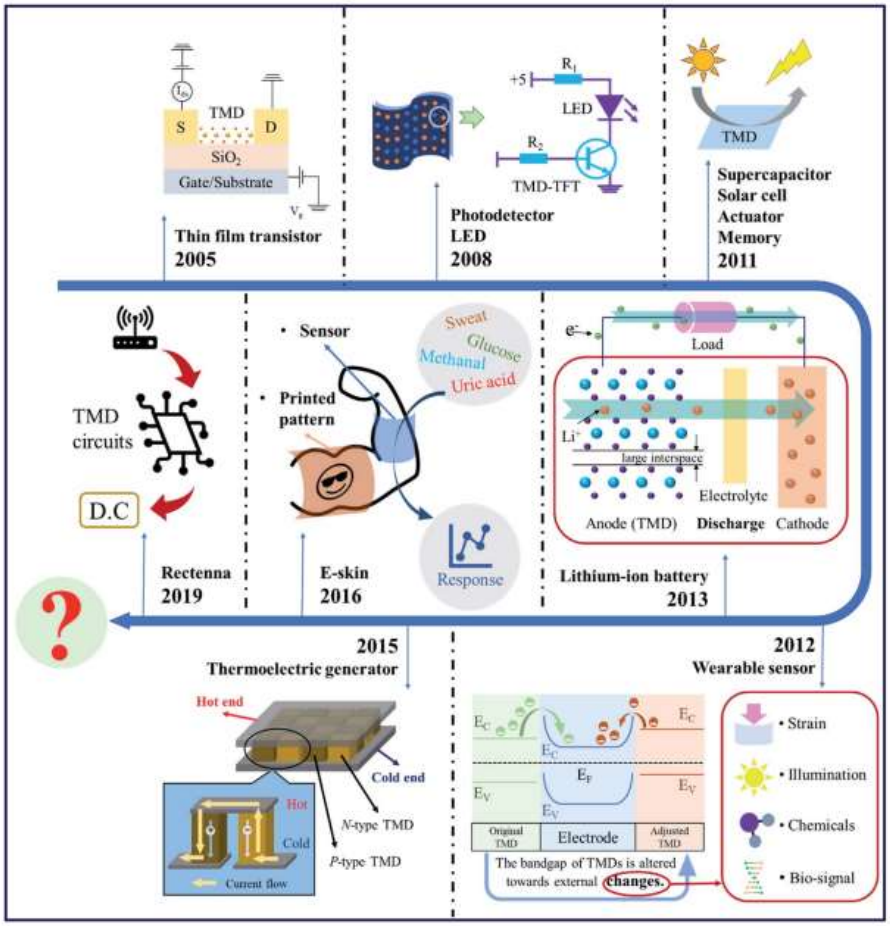

Figure 10. *The timeline of some key 2D TMD-based electronics. [Adopted from Ref. [106]].*

2DMs, especially TMDs, showed significant progress for different utilisations and applications, as shown in **Figure 10**. Due to their atomically thin nature, 2DMs inherent mechanical superiority (high Young and flexural modulus together with the endurance of high strain values before breaking) compared to other candidates for flexible electronics.[107] Bertollazi et al. experimentally derived the in-plane stiffness of monolayer MoS_2 at 180 ± 60 Nm^{-1}, corresponding to an effective Young's modulus of 270 ± 100 GPa, which is comparable to that of steel. Furthermore, they have shown that the breaking occurs at an effective strain between 6 and 11%, with the average breaking strength of 15 ± 3 Nm^{-1} (23 GPa), which is an order of magnitude larger than standard industrial Si wafer breaking.[107] To illustrate 2DMs

mechanical superiority, a comparison can be drawn with simple metal; a rod of Aluminum can be bent only for a small amount before breaking, while a thin Al foil can be bent significantly more. Additionally, other mechanisms can enhance the mechanical properties of some 2DMs.[108] Based on the combination of mechanical and other properties of 2DMs, they show high potential for flexible electronics. **Figure 11** shows a comparison of transport and mechanical properties of different 2DMs, from where it can be seen that they cover a wide range of required physical properties.

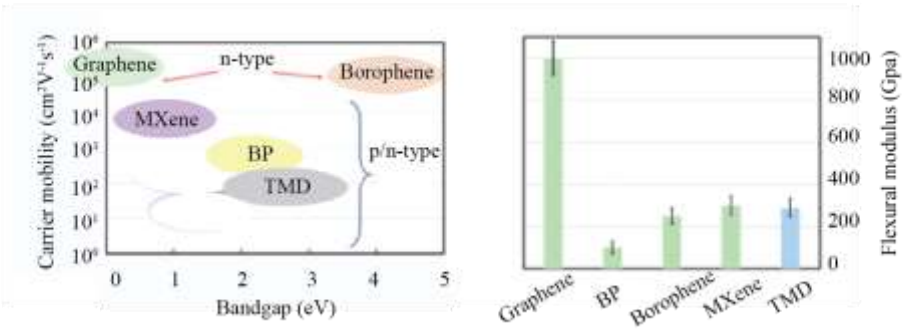

Figure 11. *The carrier mobility, bandgap and flexural modulus of some state-of-the-art 2DMs. [Adopted from Ref. [106]].*

Depending on various physical properties and their behaviour under strain, different 2DM s can be used for different devices. For example, if a material's mobility and resistance change only by a small amount reproducibly, as seen in **Figure 12(a)**, they can be used for flexible transistors.[109,110] Generally, if the physical properties do not change under strain, that material can be used as a flexible and stretchable sensor, e.g., as chemical sensor or photodetector, as illustrated in **Figure 12(b)**.[105,111] As shown in **Figure 12(c)**, if a material has a considerable change of physical property under strain, it can be used for a strain sensor and from there for pressure sensors or accelerometers.[79,112] In the case of monolayers, their inversion symmetry is broken, meaning they exhibit piezoelectricity and have possible applications as actuators and energy harvesting.[113] In addition, 2DMs performances under strain can be exploited for devices; with strain application in 2DMs, their properties can be enhanced. For example, the bandgap can be reduced or metal-insulator phase transitions induced, as shown in **Figure 12(d)**.[71,114,115]

Although many applications have been verified in the laboratory, there is still a need for many optimizations and upgrades to realize their commercial potential. As previously mentioned, large-scale samples and their transfer method are vital for integrating 2DMs into the industry. Furthermore, devices based on 2DMs can be enhanced with new dielectric layers,

improved contact fabrication and resistance, or overall device architecture.[86,94,106,116] Also, 2DMs can be combined with other industry-established materials, such as various polymers, to exploit the benefits of both. For instance, 2DMs can be used as conductive ink for printed electronics on flexible substrates.[117,118]

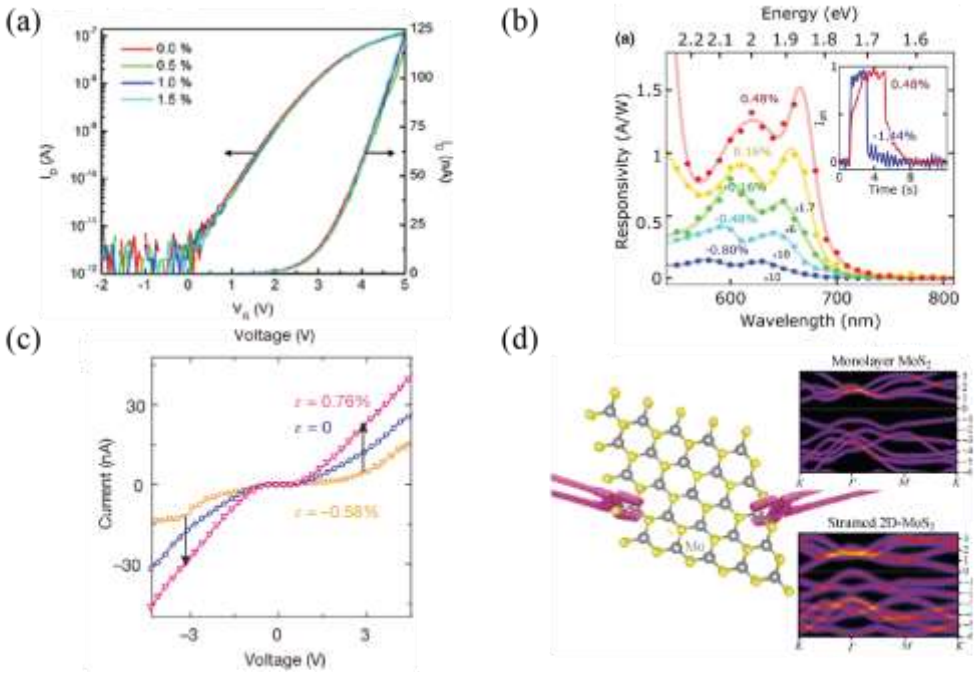

Figure 12. *Examples of properties of MoS_2 and MoS_2-based devices under strain. (a) I_{DS}-V_G characteristic of a FET constructed from MoS_2/hBN/Gr heterostructure under tensile strain.[Adopted from Ref. [110]]. (b) Photoresponsivity of MoS_2 photodetector under compressive and tensile strain [Adopted from Ref. [119]]. (c) I-V characteristics of MoS_2 monolayer under tensile and compressive strain. [Adopted from Ref. [113]]. (d) Strain-induced bandgap modulation of MoS_2 monolayer. [Adopted from Ref. [115]].*

To summarize, 2DMs present a platform for achieving new and enhanced flexible electronic devices such as wearable sensors or foldable smartphones. In addition, TMDs offer a tunable band structure, transparency and high flexibility, which are advantages over other candidates for similar technological tasks. However, on the way toward commercially available 2DM devices, there is still a requirement for large-scale synthesis and transfer with surface and architecture processing to ensure improvements in contact resistance, adhesion, defects, and contaminations.

1.4. Objectives

At the end of the introduction, we summarize the objectives that are aimed throughout the thesis. The main goal is to explore the potential of a selected set of 2DMs for flexible electronics, and in particular, to investigate which material synthesis and device fabrication methods are most suitable for specific flexible devices. First, surface, optical and transport properties of 2DMs will be investigated after exposure to the ambient conditions and subsequent transfer to the device-ready substrate. For certain 2DMs, such as MoS_2/Gr heterostructure and especially Bo monolayer, this presents a significant challenge preventing utilization for any electronic devices.

Secondly, different device fabrication methods, including transfer and lithography, will be used to determine which methods induce minimal structural impairment of 2DMs and their respective devices. For this part, the focus will be dedicated to large-scale MoS_2 monolayers, as the most-established representative of semiconducting 2DMs. Additionally, to verify MoS_2 quality, prior to MoS_2 exploit for strain-dependent measurements, doping effects on optical properties and FET devices will be investigated at the Si wafer. Afterward, propagation of strain induced by bending will be studied for large-scale sheets to conclude the role of cracks and grain boundaries by MoS_2 strain-dependent absorption spectroscopy and resultant GFs for positions of A and B exciton. Next, strain-dependent measurements of photocurrent and resistance will be performed with an analysis of corresponding GFs, to reveal MoS_2 suitability for flexible photodetectors and strain sensors. At the same time, PL spectroscopy will be employed to derive a local strain map induced by a transfer of MoS_2 sheet on a flexible substrate patterned with electrodes.

Chapter 2

Methods and experimental setups

This chapter shows experimental setups and methods which were used for our research. All methods and setups are divided into six groups. The first displays methods for synthesizing 2DMs, and the second shows setups used for fabricating devices based on 2DMs. After that, setups and methods for characterisations performed on 2DMs and devices based on them are disclosed, starting with surface morphology and then optical and transport characterisations. At the end of the chapter, bending setups used for applying strain during strain-dependant measurements are presented.

Our work was based on large-scale (>500 μm) 2DMs that were obtained by CVD and MBE growth. Samples of MoS_2, Bo, and Gr monolayers and MoS_2/Gr heterostructure were investigated. Depending on the 2DM and its properties, different synthesis methods are used through this work. Each batch of samples required initial characterisations, which would confirm the quality of the samples before further exploitation for devices.

Through our research, 2DMs were used to fabricate FETs on Si//SiO_2 wafers and strain detectors and photodetectors on flexible polycarbonate (PC) sheets. All devices consisted of a 2DM and substrate with electrode pairs. 2DM was transferred on electrodes, or either electrodes were patterned directly over it. 2DMs were transferred, via electrochemical or PDMS transfer, while electrodes were fabricated by stencil or e-beam lithography, depending on device configuration. A detailed description of all transfer and lithography methods used for device fabrication is given in chapter 3, while this chapter provides a brief overview and general technicalities.

After obtaining 2DM samples, various microscopy techniques were employed to determine their surface characteristics. Depending on the substrate on which materials are characterised, an optical microscope, AFM, or scanning electron microscope (SEM) presented a more beneficial and faster choice.

Raman, PL, Absorption and micro-reflectance spectroscopy were employed throughout the thesis. While before implementing MoS_2 into strain devices, transport properties were tested on Si wafers. Resistance, carrier mobility, and on-off ratio were calculated from I-V sweeps.

Two configurations of setups were used for controlled strain application: two-point bending and three-point bending. Both configurations induced the uniaxial tensile strain in 2DM by bending the flexible substrate on which 2DM and devices based on 2DM were transferred or fabricated. Setups are situated in ambient conditions with access for optical and transport characterisation. By employing them, strain-dependent measurements of MoS_2 monolayer resistance, photocurrent, photoluminescence, and absorbance were performed.

2.1. Synthesis of 2D materials

2.1.1. CVD in an inert atmosphere

CVD in an inert atmosphere was used to synthesize MoS_2 monolayers on top of oxide-covered Si wafers (Si/SiO_2), with an oxide thickness of 75 nm or 300 nm. Such substrate is suitable for transport characterisation and quick inspection via optical microscope, allowing distinction of 2DMs from the substrate due to the oxide thickness and interference effect.[120] Schematic of CVD growth is depicted in **Figure 13(a)**, while the photograph of the setup used is shown in **Figure 13(b)**. The standard synthesis protocol uses 3 mg of MoO_3 powder inside a ceramic boat and 2 mg of sulphur powder in a separate ceramic boat. With heating the ceramic boat, precursors evaporate under the argon gas flow (10 – 100 s.c.c.m). Sulphur and molybdenum react over the heated surface of the Si wafer kept at 750 °C, resulting in the growth of monolayers of MoS_2. Temperature is regulated with spiral heaters, the area of the quartz tube in which synthesis occurs is insulated with polystyrene foam, while a K-type thermocouple monitors the temperature. With this method of precursor delivery, full coverage samples with centimeter lateral size can be grown.[121] With the variations of precursor type and their delivery method, grown 2DMs can be small isolated flakes or large-scale sheets. For example, isolated flakes (with lateral sizes up to 50 µm) are obtained by changing the molybdenum precursor to a mixture spread over the substrate surface prior to the synthesis. The mixture consists of two deionized (DI) water-based solutions in equal parts: 15.4 parts per million (ppm) solution of ammonium heptamolybdate ($(NH_4)_6Mo_7O_{24}$) (AHM) and a solution of sodium-molybdate (Na_2MoO_4).[122]

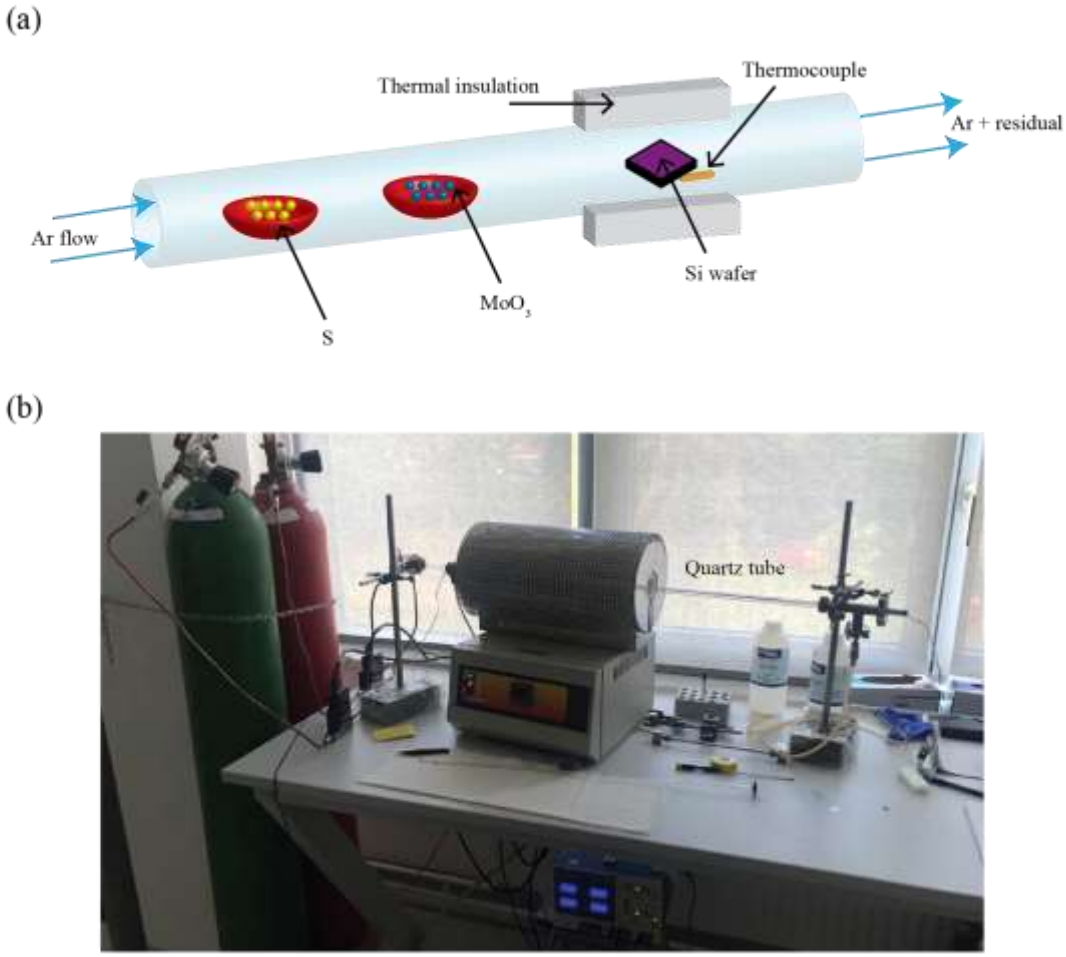

Figure 13. *CVD synthesis of MoS_2. (a) Schematic illustration of CVD synthesis on Si wafer. (b) Photograph of CVD setup at Institute of Physics in Zagreb (IFZg).*

Although many samples can be prepared via CVD, their quality drastically varies from batch to batch due to the slightest variations of humidity and pressure inside of the chamber.[123] Often flakes of 2DM grown by CVD had different optical properties, e.g. Raman and PL, even though they were grown not only in the same batch but also on the same sample. The biggest obstacle in employing these samples for devices was their quality degradation, reflected in transport characterisations. The most apparent degradation of quality was primarily due to ambient exposure, which promoted crack formation at grain boundaries, initially induced by a difference in thermal expansion of MoS_2 and SiO_2 during sample cooling after synthesis. Secondly, due to inherent structural defects, samples often lacked the standard behavior of previous reports of transport characterisations on 2DMs grown by this method.[55,56] With specific batches, FET devices fabricated on Si/SiO_2 wafers showed expected I-V characteristics. However, additional samples were bought from commercial suppliers (such as 2D semiconductors), for strain-dependent measurements, due to variation of homegrown MoS_2

quality and sensitivity of the growth output from batch to batch. By using such purchased, standardized materials, we were also able to draw additional, better established conclusions about certain properties of the respective devices.

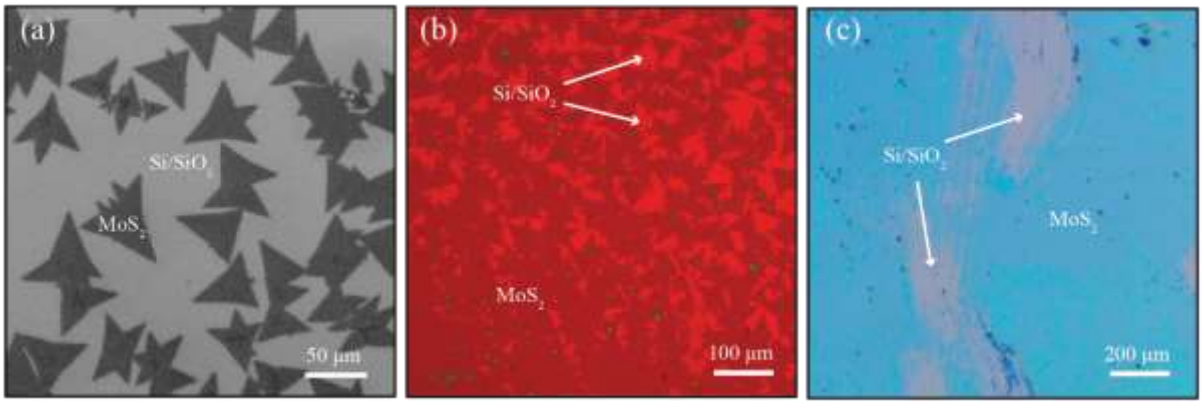

Figure 14. *Images of CVD-grown MoS_2 samples. (a) SEM image of homegrown isolated flakes of MoS_2. (b) Optical microscope image of homegrown MoS_2 islands starting to form large scale sheet. (c) Optical microscope image of bought full coverage MoS_2 sheet with scratched areas to distinguish substrate.*

Examples of samples grown via the CVD method are shown in **Figure 14**. SEM image of isolated flakes whose growth was stopped before the formation of a complete monolayer is given in **Figure 14 (a)**, while **Figure 14(b)** shows an optical micrograph of MoS_2 flakes that started to form a full-coverage monolayer sheet. **Figure 14(c)** shows an optical micrograph of a full coverage sheet that was deliberately scratched to uncover the bare Si wafer surface and to distinguish material from the substrate. Colour variations of optical micrographs are due to different RGB parameters used on different microscopes. Detailed analysis with AFM or SEM of each flake was done, in parallel with optical characterisation, to determine which flakes or sheets would be suitable for further device fabrication. [124,125]

2.1.2. CVD in UHV

CVD growth in UHV was employed to synthesize high-quality samples of Bo and Gr on Ir(111) single-crystal (bought from MaTeck). Before synthesizing any 2DM, Ir(111) substrate was annealed to 1225 °C under Ar+ ion exposure at 1.5 keV at chamber base pressure $p \approx 8x10^{-10}$ mbar. Sample temperature is determined through thermocouple (C-type or K-type), which were in physical contact with the iridium crystal. Annealing ensures the structural quality of the

substrate and the absence of any adsorbates, which yields a sample surface containing large terraces of specified crystal orientation separated by (most often) mono-atomic steps

After cleaning the substrate, a combination of temperature programmed growth (TPG) and CVD methods was used to synthesize the Gr monolayer sheet.[126] First, Ir(111) was exposed to ethylene at room temperature until saturated and heated to 1025 °C in temperature-programmed growth. TPG consists of adsorption of precursor on the substrate crystal at room temperature until saturation is achieved (typically applied dose was 5×10^{-8} mbar of hydrocarbon during 50 s), followed by short annealing (800 – 1200 °C range, 30 s). This procedure yields small nanometer-sized, epitaxial Gr samples on the Ir surface, whose average size depends on the annealing temperature. For full sheet coverage of Gr, CVD is subsequently done by exposing the sample to hydrocarbon at the temperature of 925 °C. [127–130] Grown Gr lies like a blanket on the substrate and bends over step edges coherently over the substrate surface. The only defects in the Gr lattice are edge dislocations forming pentagon-heptagon carbon atom rings. However, these edge dislocations are spread in low density.[131] **Figure 15(a)** shows a photograph of the used UHV chamber for synthesizing the Gr on Ir(111). This chamber offers *in-situ* characterisation with LEED, STM and STS.[132] Examples of STM and LEED images of Gr grown on Ir(111) are shown in **Figure 15(b)** and **Figure 15(c)** respectively.

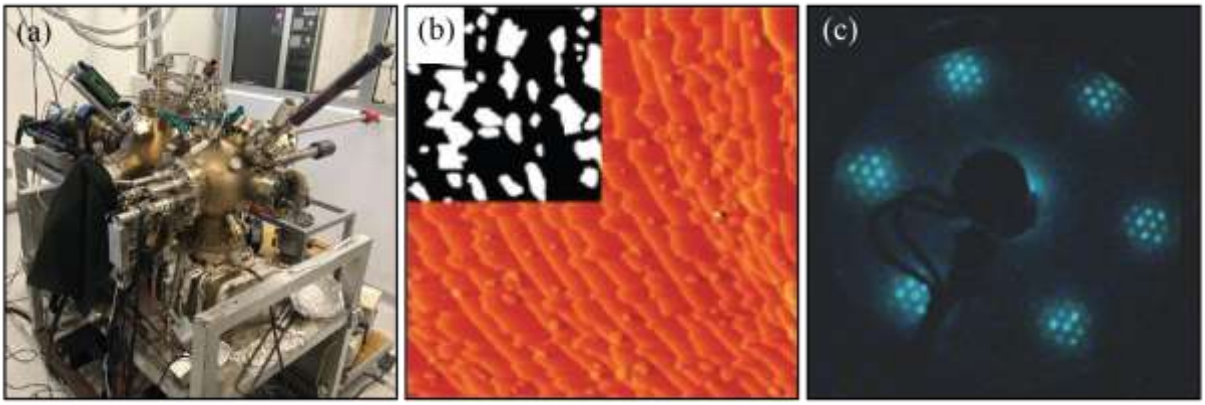

Figure 15. *TPG/CVD growth of Gr in UHV. (a) Photograph of the UHV setup, with STM and LEED, used for Gr growth at IFZg. (b) STM image of graphene growth on Ir(111) with inset showing areas of Gr with white and Ir with black color. [Adopted from Ref. [126]]. (c) LEED image of the full coverage monolayer Gr on Ir(111).*

Segregation-enhanced epitaxy, a variation of CVD growth, was employed for the growth of Bo. Repetitive cycles of borazine ($B_3H_6N_3$) exposure at vapors at a pressure of 3×10^{-8} mbar and temperature 1200 °C with subsequent sample cooling were employed to synthesize

χ_6 polymorph Bo on Ir(111) [Bo/Ir(111)].[36] During borazine exposure at high temperature, B atoms dissolve in the subsurface regions of Ir. As the sample is cooled after borazine exposure, the solubility of B in Ir reduces and B atoms segregate to the surface of Ir crystal and self-assemble into borophene. The process is schematically illustrated in **Figure 16**. With increasing the number of the growth cycles N_c, the Bo coverage increases until full a full monolayer is reached(at $N_c = 12$, for this particular set of synthesis parameters). With each cycle, the amount of dissolved B atoms available for segregation to the Ir surface increases, and Bo coverage (Θ_{Bo}) becomes larger accordingly.

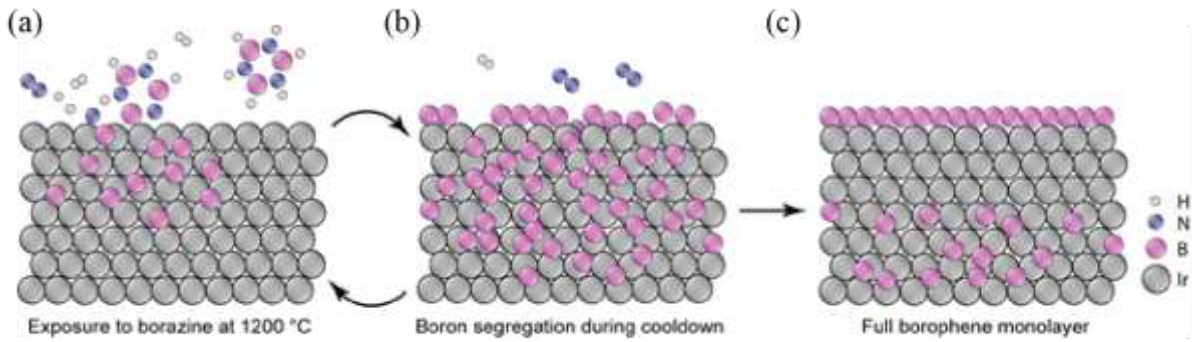

***Figure 16**. Schematic of segregation-enhanced epitaxy of Bo on Ir(111). (a) Borazine precursor is dosed repeatedly onto the hot Ir surface, resulting in boron dissolution into the bulk. (b) Sample cooldown follows each dosing step, during which B atoms segregate to the surface and self-assemble into a Bo mesh. (c) After finishing a set of dosing/cooling cycles, a full Bo monolayer is formed on the surface. [Adopted from Ref. [133]].*

By observing in-situ low energy electron diffraction (LEED), an increase of Θ_{Bo} as a function of the number of N_c can be determined. **Figure 17(a)** shows LEED pattern line profiles across the first order Ir diffraction spot and its first neighboring Bo spot at several N_c. A typical LEED image of 1 ML Bo/Ir(111) is shown in the inset of **Figure 17(a)**, with a characteristic sharp (6×2) pattern with three rotational domains visible.[36,134] The χ_6 polymorph has been assigned to such a diffraction pattern and the same polymorph can also be fabricated on Ir(111) by employing MBE[135] or conventional CVD technique.[136] After synthesis and in-situ confirmation of structural quality and coverage with LEED, sample was taken out of the UHV chamber for further analysis and processing. Fast ex-situ inspection regarding surface morphology and sample stability under ambient conditions can be achieved by employing AFM and SEM microscopes, as shown in **Figure 17(b)** and **(c)**, respectively.[133] With this growth method, Bo monolayer can also be grown in-house on metallic foils such as Cu and Ni.

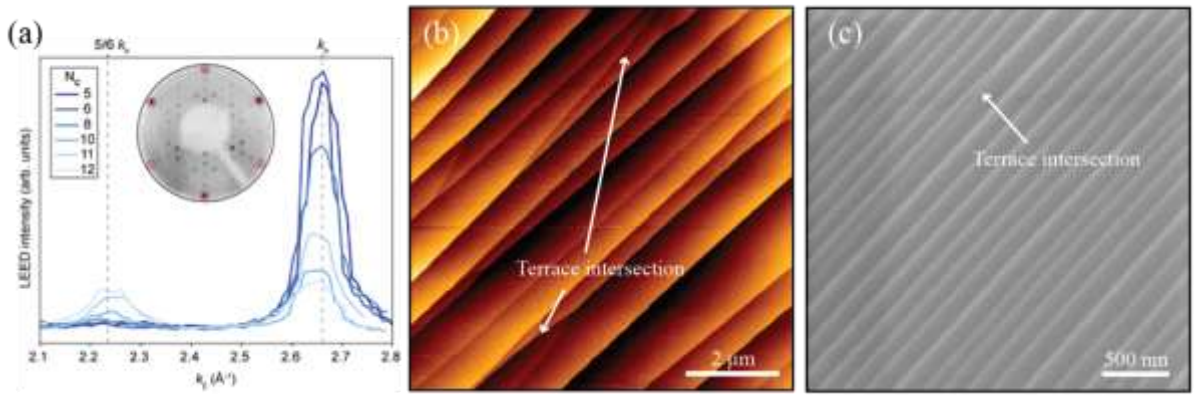

Figure 17. *In-situ and ex-situ characterisation of Bo monolayer on Ir(111), (a) A sequence of Ir and Bo diffraction spot profiles extracted from LEED images recorded after the noted number of dosing/cooling cycles (N_c). A decrease of Ir spot intensity and an increase of Bo spot intensity as a function of N_c is visible. Inverted LEED image of a monolayer Bo/Ir(111) recorded at 35 eV, with the Ir spots encircled in magenta, is shown in the inset. Superposition of three 120°-rotated (6×2) patterns corresponds to the Bo layer. (b) AFM image of Bo monolayer with visible Bo features such as intersecting terraces and step bunching. (c) SEM image of Bo monolayer after ambient exposure without any visible contamination or degradation. [Adopted from Ref.* [133]*].*

2.1.3. MBE in UHV

UHV molecular beam epitaxy (MBE) was employed to synthesize MoS_2/Gr heterostructures.[58,137] As illustrated in **Figure 18**, nanometre MoS_2 islands were grown by MBE on a Gr sheet, previously synthesized on Ir (111) by a combination of TPG and CVD. MBE offers a method for synthesis with minimal defect density and negligible substrate interaction for 2DMs such as MoS_2.[57] In contrast, CVD methods require the catalytic role of the substrate, which is a challenge in the case of sulphur precursors in a low-pressure environment and in the case of the insulating substrate which lacks catalytic properties.

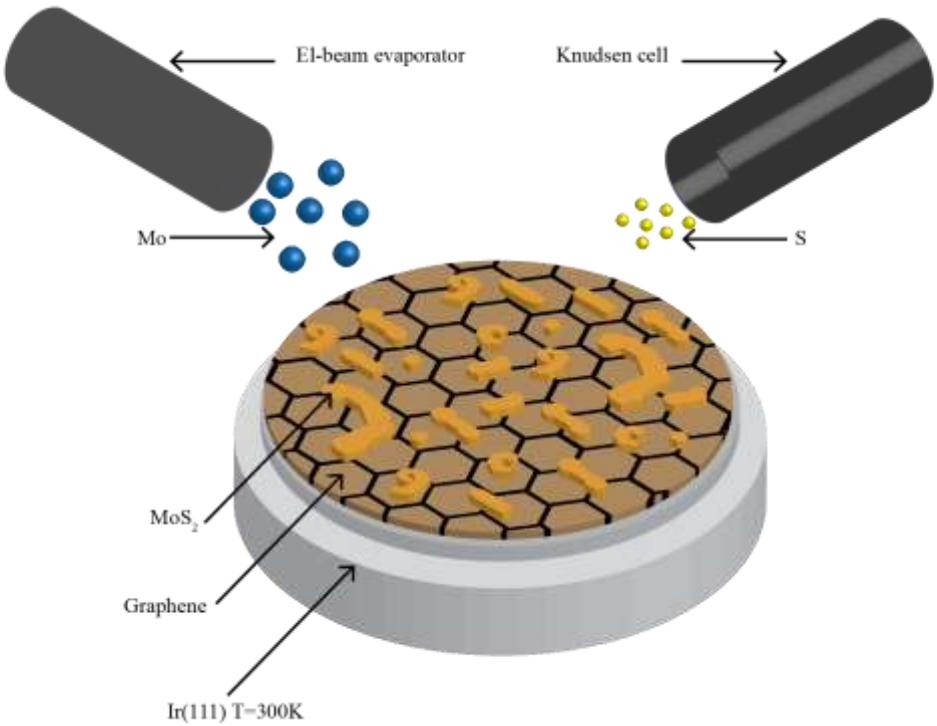

Figure 18. *Schematic illustration of MoS_2 on Gr on Ir(111) via VdW MBE growth.*

A two-step method was used to synthesize MoS_2 monolayers on Gr / Ir (111). First, the growth substrate is exposed for 15 minutes to Mo flux of 6×10^{14} m^{-2} s^{-1} at a background sulphur pressure of 1×10^{-8} mbar, at 300K. Secondly, the substrate is annealed at 1160 K and left in sulphur vapor pressure for 1 minute. In the first step, using lower temperatures prolongs sulphur residence time on the substrate surface, promoting the formation of MoS_2 from molybdenum and sulphur. The second step is used to prevent unwanted properties such as nonuniform shapes, random orientations, and the presence of bilayers. With annealing of the sample, higher quality of MoS_2 islands is achieved due to island diffusion and coalescence. During growth, surplus of sulphur atoms promotes reactivity with Mo but in values with which formation of bilayers and intercalations can be avoided. [130,138] An example of the STM topograph of MoS_2/Gr heterostructure is shown in **Figure 19(a)** with height profile, taken along indicated blue line, shown below the topography. **Figure 19(b)** shows atomic resolution STM of MoS_2 island, while a typical LEED pattern of the heterostructure is shown in **Figure 19(c)**.

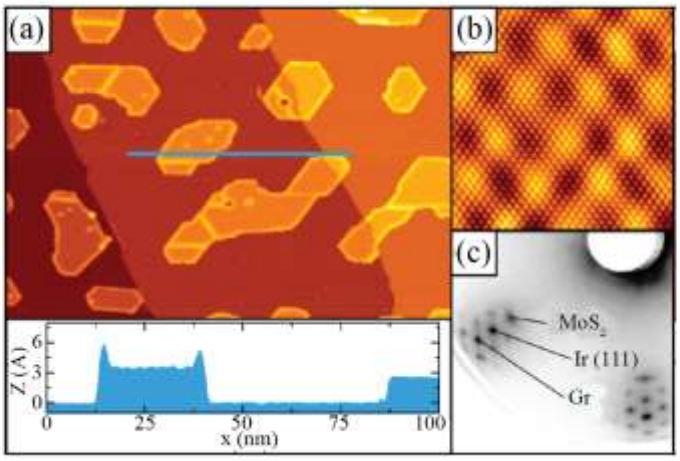

Figure 19. *MBE growth of MoS_2/Gr heterostructure. (a) STM topograph after growth of MoS_2 islands with the on Gr/Ir(111). The height profile along the indicated blue line is shown below. (b) Atomically resolved topograph of a MoS_2 island. (c) Section of a corresponding 80 eV LEED pattern. The first-order reflections of MoS_2, Ir(111) and Gr are indicated. [Adopted from Ref.* [58]*].*

2.2. Device fabrication

2.2.1. Transfer methods

Through this research, two transfer setups were built, one for electrochemical delamination and the other for PDMS stamping, both using a polymer layer for the transfer. The electrochemical delamination setup is shown in **Figure 20(a)** while the setup for PDMS stamping is shown in **Figure 20(b)**. Generally, there are many methods of transfer that are not limited by polymers or exploit some modifications of our procedure, but with stamping and electrochemical delamination whole range of 2DMs and substrates is covered. Substrates on which 2DM are transferred can be arbitrary with minor modifications of transfer procedures. Substrates can have a clean surface, other 2DMs or structures patterned previously with any type of lithography. We have established successful protocols for both methods for various 2DMs such as MoS_2, Gr, Bo, and their heterostructures.[133,138,139] A detailed description of both transfer methods is given in section **3.1.**.

A two-step electrochemical method was used to transfer 2DMs from metallic single-crystals and foils. PMMA in a solvent, that forms a couple of tens of micrometer thick layer after solidification, was used as a support during the transfer. The first step consists of

intercalation, which weakens 2DM and substrate interaction, followed by delamination, during which 2DM separates entirely from the substrate.[62] With electrochemical delamination, substrate used for transfer has to be resistant to acetone used for removing the polymer and chemical solvents exploited during the transfer procedure.

For the PDMS transfer, 160 µm thick PDMS was used for transferring 2DMs from Si/SiO_2 substrates and sapphire. With the stamping method, the most important parameter is the speed of mechanical separation of polymer used during transfer, which depends on the adhesion of specific 2DM to the substrate.[66]

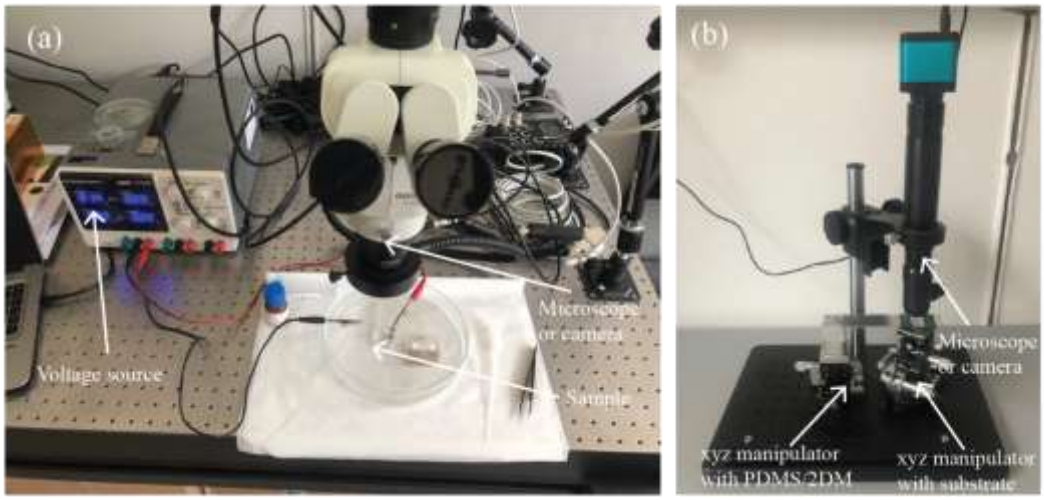

Figure 20. *Home-built setups for transfer of 2DM at IFZg. (a) Setup for electrochemical delamination used for transfer of 2DMs from metallic substrates. The most crucial parameter is the voltage difference applied to sample while immersed in different solutions for intercalation and delamination steps of the transfer method. (b) Setup for PDMS stamping used for targeted transfer of 2DM by two sets of XYZ manipulators. The most critical parameter is separating the PDMS/2DM stamp and the substrate, which can be controlled by z-axis movements with manipulators and simultaneously observed via an optical microscope or camera.*

2.2.2. Lithography

In our work, we have developed procedures for fabricating electrodes on rigid and flexible substrates such as Si/SiO_2 or PC. Both methods can fabricate electrodes directly on 2DMs or substrates with a subsequent transfer of 2DMs on top of the electrodes. The basis of both methods is selective covering the substrate with a protective layer modelled to the wanted

shape. After forming or placing a protective layer, a layer of metal is deposited on top with thermal evaporators shown in **Figure 21**. Usually, first a thin layer of Cr (< 5nm) is deposited to promote adhesion of the Au layer (≈ 75 nm) deposited subsequently inside of the vacuum chamber (i.e., metal evaporator). Piezoelectric quartz crystal microbalance (QCM) sensors can monitor deposited metal thickness. Under the mass increase due to deposited metal on top of the QCM sensor, its frequency is changed. By precisely monitoring changes, deposited mass and the height of the deposited electrodes can be determined.[140] Both e-beam and stencil lithography methods and protocols are described in section **3.2.**.

Stencil lithography can rapidly fabricate large-scale electrodes or any features (> 100 μm) by exploiting a mechanical mask fabricated by cutting metal sheets with a modified plotter or femtosecond laser. After metal evaporation and removal of the stencil, metal is left on the substrate areas exposed by features formed in the stencil. With devices on flexible substrates, the robustness of the electrodes was preferred, and stencil lithography was the most used method for electrode fabrication.

With e-beam lithography, nanometre-sized electrodes or features can be fabricated. SEM, described in the following section, generates an e-beam that is precisely moved over the sample by a set of magneto-optical components for selective exposure of the polymer. Depending on polymer type, either positive or negative imprint can be used. In the case of a positive polymer, bonds are weakened upon e-beam exposure resulting in rupture of the polymer after further processing with developer and stopper solutions. In the case of a negative polymer, bonds are strengthened upon e-beam exposure resulting in the removal of unexposed areas after further processing.[141] In the case of an insulating substrate such as PC sheets, glass or sapphire additional polymer layer is beneficial. Although the second polymer is not affected by the e-beam exposure, it promotes the dissipation of electrical charges to realize accurate structural images on the bottom polymer pattern. After metal deposition, the polymer is removed by acetone, leaving metal on selected areas unprotected by the polymer mask. It was the preferred method of fabrication of electrodes for transport characterisation on Si wafers where minimal electrode dimensions were desired.

Figure 21. Metal evaporator at IFZg.

2.3. Morphology characterisation

2.3.1. SEM

SEM is a tool for the quick assessment of the sample quality. Within a few minutes, the whole growth substrate can be inspected. **Figure 22** shows TESCAN VEGA 3 SEM with a tungsten filament, and the specified resolution of 3 nm, that was used for our measurements. Resolution of the imaging decreases with insulating substrates due to the charging effect.[142]

Figure 22. Photograph of SEM at IFZg.

Figure 23(a) shows a schematic of SEM and its components. An electron beam is generated by an electron source (in our case by heating a tungsten filament) and subsequently accelerated by the anode whose potential determines the initial beam parameters. Voltage is set in the range from 1 kV to 30 kV depending on the sample imaged. Generally, the higher the

voltage the better the resolution, but those parameters can also damage sensitive samples and accumulate charge for non-conductive samples. With condenser lenses and an objective lens, the beam is formed and focused on the sample, while with x-y scan coils move the beam over the sample surface, which is a crucial feature for e-beam lithography that uses an electron beam and SEM. After e-beam exposure to the sample, electrons and photons induced by a different physical process can be collected, such as secondary electrons, back-scatter electrons, or Auger electrons. All possible processes upon the collision of the electron beam and the substrate are shown in **Figure 23(b)**. Secondary electrons generally give the best information on the sample's topography, while back-scattered electrons give images based on different atomic numbers and can be used for distinguishing different materials on the surface.

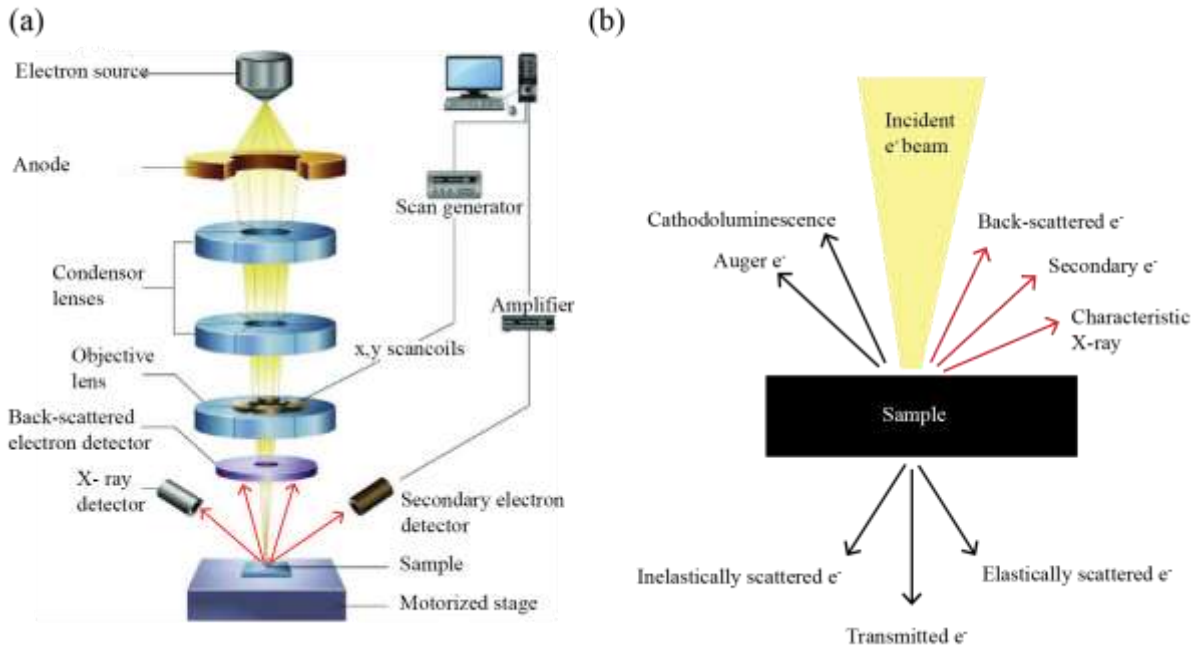

Figure 23. *Illustration of SEM components and resulting electrons and photons. (a) Schematic representation of SEM and its components. [Adopted from Ref.* [143]*]. (b) Illustration of electrons and photons that emerge from the collision of the e-beam and the sample, with red arrows showing the particles that can be detected with the SEM used in our work.*

The basis of SEM imaging is exposure to an electron beam, after which excess electrons can get trapped around the imaged area.[142] In the case of the Si wafer, the effect can be minimized with the use of lower beam intensity (BI < 5) and lower high voltage (HV < 10 kV) with longer working distance (WD > 10 mm). Our Si wafers had an oxide layer of 85 nm and 300 nm, which prevents charge dissipation to Si substrate, but with the more careful setting of the imaging parameters, 2DM can be inspected on them. However, in the case of PC sheets,

even the least invasive parameters cannot prevent charge accumulation. For such substrates, samples can be coated with a conductive polymer, such as Electra 92 PMMA, which can be washed away easily with deionized (DI) water after imaging.

2.3.2. AFM

AFM provides topography information of the samples, with a possibility to identify nanometre-sized features. AFM is a powerful tool for analyzing the large-scale sheets of 2DMs on any substrate, in contrast to SEM which has limitations in view of non-conductive substrates. JPK/Bruker Nanowizard Ultra AFM was used for our work, which is depicted in **Figure 24**. With our AFM, images of maximum 30 µm by 30 µm size can be obtained with a maximum sample height of 2 µm. For each AFM image, one can get information on topography but also on phase-contrast of the surface, from which one can distinguish various types of materials on the sample. AFM was particularly useful for determining the success of the 2DM transfer by measuring topography prior and post transfer, because with AFM different defects can be distinguished (such as transfer contaminations, physical cracks and holes).

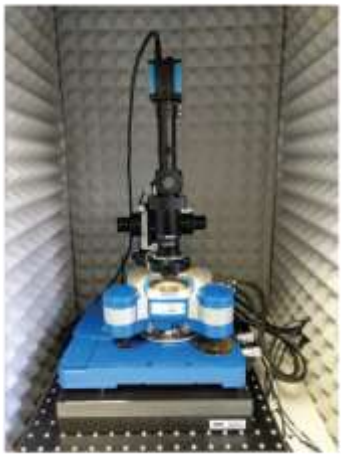

Figure 24. *Photograph of AFM used at IFZg.*

Figure 25(a) shows a schematic of AFM operation. AFM cantilever with tip is brought close to surface with step motors and lowered in contact with the surface be means of precise piezo controllers. The tip follows the contour of the sample surface, during which the exact position of the tip is determined with a laser deflected from a cantilever to a segmented photodiode. As a result, an AFM topography image is acquired by moving the cantilever and scanning the sample surface line by line. With AFM, detailed information (resolution of around 100 pm along the z-axis) on the height is obtained. However, in lateral axes, the image gets

modified by tip convolutions, which results in features seemingly larger than they are in reality as shown in **Figure 25(b)**. Depending on the material imaged, softer or harder tips can be used to ensure that there is no damage to the samples. In the case of stiff tips, the surface can get scratched and damaged. In some cases, scratching can be beneficial, for instance for SPM lithography or imaging of full coverage samples. In the case of soft tips, one should be aware that excessively soft tips can give false signals that are based only on the slightest interactions without any valid data regarding topography. In general, with a good choice of tips and imaging parameters, one can inspect any 2DM-substrate combination. Non-contact AC (tapping) mode was used for image acquisition with a setpoint around 50%. We used Bruker FESP-V2 silicon tips with a nominal spring constant of 2.8 N/m, a tip radius of 8 nm and a resonance frequency of 75 kHz, and Bruker TESP-V2 silicon tips with a nominal spring constant of 37 N/m, a tip radius of 7 nm and a resonant frequency of 320 kHz. Images were processed with JPK Data Processing software and WSxM software.[144]

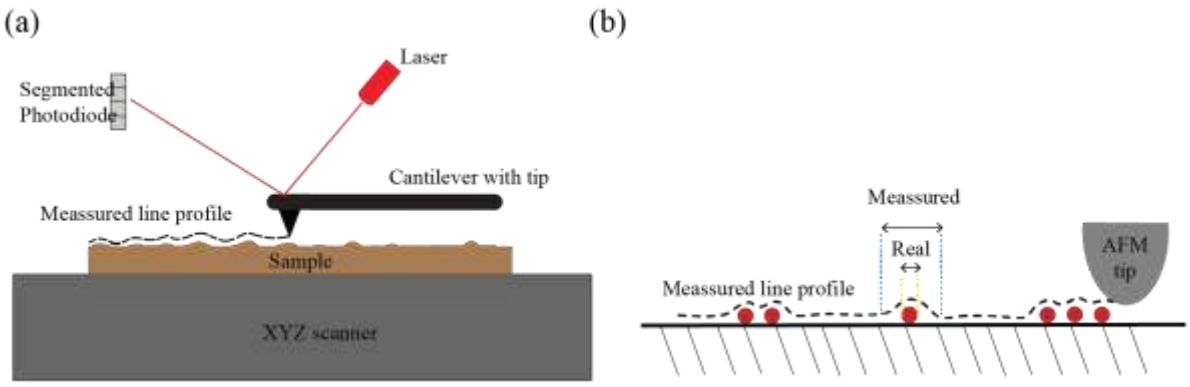

Figure 25. *Illustration of AFM components and operation. (a) Schematic of AFM operation with indicated measured profile acquired by monitoring cantilever position with a laser beam. (b) Lateral dimensions in AFM are subjected to convolution, which completely distorts the lateral size of the sample features comparable to the tip size (<10 nm).*

2.4. Optical spectroscopy

2.4.1. Raman spectroscopy

By exploiting an optical probe (laser or white light) that illuminates 2DM, spectra of the probe can be collected with spectrometers for different ranges of energy, thus providing signatures of various properties of 2DM. **Figure 26(a)** shows the optical characterisation setup, consisting of the laser source (optical probe), XYZ sample stage, spectrometer with charge-coupled device

(CCD) detector, and series of optical elements such as filters and fibers used for guiding and selecting the optical probe. A schematic of the optical characterisation setup is illustrated in **Figure 26(b)**. After the optical probe interacts with the sample, the reflected part of the probe is selected with a set of Bragg filters and subsequently analyzed by a spectrometer (Andor-500i-B1) with an EM CCD detector (Newton 971). 50× infinity-corrected objective NA = 0.75 (numerical aperture) was used for focusing the incident beam on the sample. A 50 µm core fiber guided the probe to the spectrometer. Higher precision can be achieved for different energy ranges depending on the spectrometer diffraction gratings (150, 300, 1800 l/mm). Depending on the material analyzed, spectrometer grating can be selected for the highest precision in a specific energy range where that material has characteristic peaks. Peak positions and shapes are sensitive to physical and chemical variations among the samples. As a result, different optical characterisations can be performed, and their features on characteristic energies can be investigated.

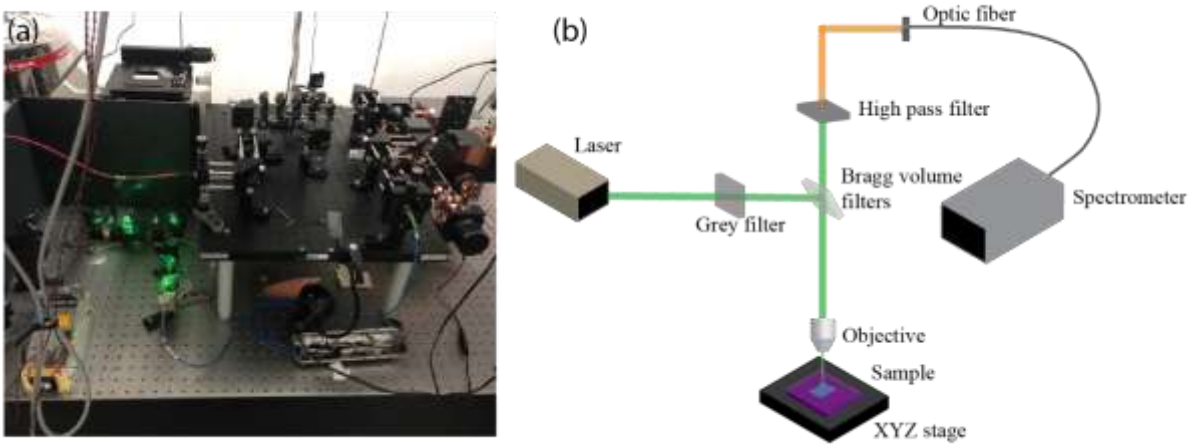

Figure 26. *Optical characterisation setup. (a) Photograph of optical characterisation setup at IFZg. (b) Schematic illustration of optical characterisation setup.*

One of the most widely used techniques for optical characterisation is Raman spectroscopy. With Raman, vibrational modes of the crystal lattice are probed, from where one can detect the type of 2DM and many of its details. Such as temperature and thickness-dependent intralayer and interlayer modes of 2DMs or phase transitions caused by defects and electrostatic doping.[145–147] Furthermore, Raman can be employed to investigate the charge density waves, moiré phonons, interfacial coupling, and cross-dimensional electron-phonon coupling.[25,148,149] Therefore, Raman is an essential technique for starting analysis of the material because it presents a fast and non-destructive method for determining material quality. For the

acquisition of the Raman spectra in the thesis, the setup shown in **Figure 26** was used in the backscattering configuration with the highest spectrometer grating number (1800 l/m). Raman was used to provide information on the overall sample quality for all investigated 2DMs, and the respective results are shown in chapter **4.**.

2.4.2. Photoluminescence spectroscopy

In 2DMs with a bandgap, such as MoS_2, PL (photoluminescence) spectroscopy can provide information on quasiparticles, excitons and trions, that have energies slightly below the MoS_2 conductive band.[24,150] Control of the carrier density by an electric field is an effective method to modulate the optical properties of monolayer TMDs.[151] However, other methods such as straining, chemical doping, and photodoping can be used to modify the PL of MoS_2 monolayers.[27,28] For the Gr, PL and absorbance spectroscopy provide a signal based only on hot electrons because of the lack of Gr bandgap.[152]

For PL spectroscopy same setup as for Raman was used, with the same optical probe (532 nm laser) and spectrometer with a selection of the grating chosen for the energy range in which MoS_2 exciton and trion peaks occur. For the acquisition of the MoS_2 PL spectra, the setup shown in **Figure 26** was used in the backscattering configuration with the spectrometer grating number (300 l/m). Part of the setup was the XYZ stage on which the sample is mounted for optical characterisation. Setup can be automated so that the stage moves line by line in 500 nm steps while spectrum is acquired at each step. As previously mentioned, bending setups were combined with the stage used for optical characterisation, which enabled the acquisition of PL maps of strained MoS_2 samples. MoS_2 PL dependence on photodoping and electric field doping is shown in subsection **4.3.2.**, while PL maps of MoS_2 and dependence on strain are shown in section **5.4.**.

2.4.3. Absorbance spectroscopy

An absorption spectrum is created by the transition from a ground state to an excited state, in contrast to the photoluminescence spectrum created by the transition from an excited state to a ground state. Those methods are complementary, as each observes the same transition but in opposite directions.[153] The absorption spectrum represents the distribution of all exciton states, while the PL spectrum corresponds to the distribution of the lowest exciton energy states. As a

result, positions of characteristic peaks are different in absorbance to PL, where the difference between positions of exciton peaks is called the Stokes shift.[24]

We have investigated strain-dependent absorption spectra of MoS_2 monolayer with a similar setup as shown in **Figure 26**. However, the setup exploited a white-light emitting diode that serves as an optical probe instead of a laser. In addition, absorbance setup was used in transmission configuration, i.e., the optical signal is collected after transmission through the sample and not reflection as in the backscatter configuration used for Raman and PL spectroscopy. The objective lens used to collect transmitted light had a wide-field configuration and NA=0.6, while detection was performed with an imaging spectrograph (300 l/mm) and a CMOS camera. Results on absorbance spectroscopy of MoS_2 in dependence on strain are shown in section **5.1.**.

2.4.4. Micro-reflection spectroscopy

Micro-reflectance spectroscopy is a technique that can be used with a regular microscope and a few upgrades, as disclosed below, for the characterisation of 2DMs fundamental optical properties as previously described for absorbance and PL spectroscopy.[154] In principle, it is based on the same physical process described for absorption spectroscopy. However, a backscatter configuration is used, and the reflected signal is analyzed.[155] Motic BA310 metallurgical microscope equipped with a 50× objective (0.55 NA and 8.2 mm WD) was modified to enable optical inspection with microscope and spectroscopy analysis of the same sample area. A halogen light source was used as an optical probe that is split at a 90/10 ratio by modified trinocular. 10% is coupled to optical fiber and used for signal analysis by CCD spectrometer, while 90% is used for imaging of the sample. In our work, micro-reflectance spectroscopy was used as a quick tool for verifying the transfer of MoS_2 on a PC sheet with Au electrodes before any strain-dependent measurements shown in section **5.2.**.

2.5. Transport characterisation

2.5.1. Resistance

A schematic illustration of the setup for measurement of resistance is shown in **Figure 27(a)**. Either the electrodes are fabricated on top of the 2DM, or the 2DM is transferred on the electrodes. Electrodes fabricated by lithography are connected to SMU with standard laboratory

wires by dropping silver paste on the pads of the electrodes. Keithley 2450 SM which was used for all transport measurements is shown in **Figure 27(b)**. With the SMU (source meter unit), the current that passes over the 2DM between electrodes can be measured while varying potential difference, applied with the same SM. SM can be programed for I-V sweeps, i.e. current is measured as a function of potential difference. Usually, voltages up to 10 V were applied. After data fitting with linear regression, resistance R can be determined for each sample. This setup can be combined with the bending setups (described in section **2.6.**), enabling the exploit of bending setups for strain-dependent resistance measurements as described in section **5.2.**.

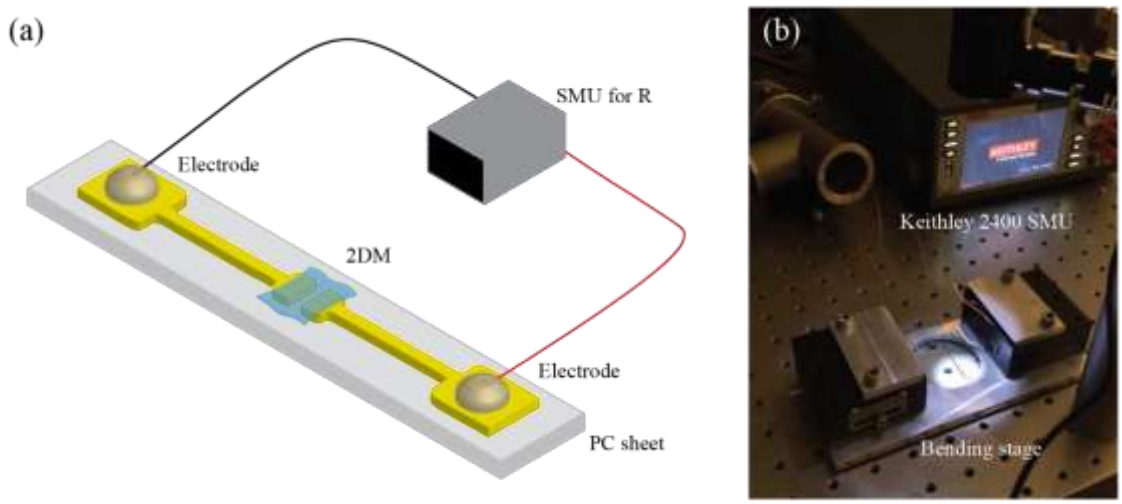

Figure 27. *Resistance setup. (a) Schematic illustration of the resistance measurement. (b) Photograph of the SM unit used for resistance measurements at IFZg.*

2.5.2. Photocurrent setup

Samples fabricated in the same configuration as for resistance measurements were characterised by the photocurrent setup, as schematically shown in **Figure 28(a)**. If the current is measured continuously in time, with the illumination of the 2DM, photocurrent can be derived by subtracting the current measured without illumination from the current measured under illumination. For the analysis of generated photocurrent by exposure to monochromatic light, a potential of 1 V was applied to the sample via electrodes, and the current was measured before, during, and after illumination. For the measurement of current, the same SM unit was used as the one for resistance measurements.

Photocurrent spectroscopy can be done by measuring photocurrent during illumination by light with different wavelengths.[119,150] Two setups were used; the first one, shown in **Figure 28(b)**, uses LED lights with specified wavelengths (365, 405, 420, 455, 470, 505, 530, 565, 595, 617, 625, 660, 780, 850) nm at fixed power of P = 1.25 µW. In contrast, the second setup used a commercial Bentham TLS120Xe light source that can continuously be set to different wavelengths in arbitrary steps with a light spot of 400 µm diameter and a power density of 8 mW/cm^2. For a closer inspection of the exciton energy range, the second setup was used with wavelengths from 580 nm to 680 nm in steps of 5 nm. A detailed description of the photocurrent measurement, data fitting, and strain dependence is given in section **5.3.**.

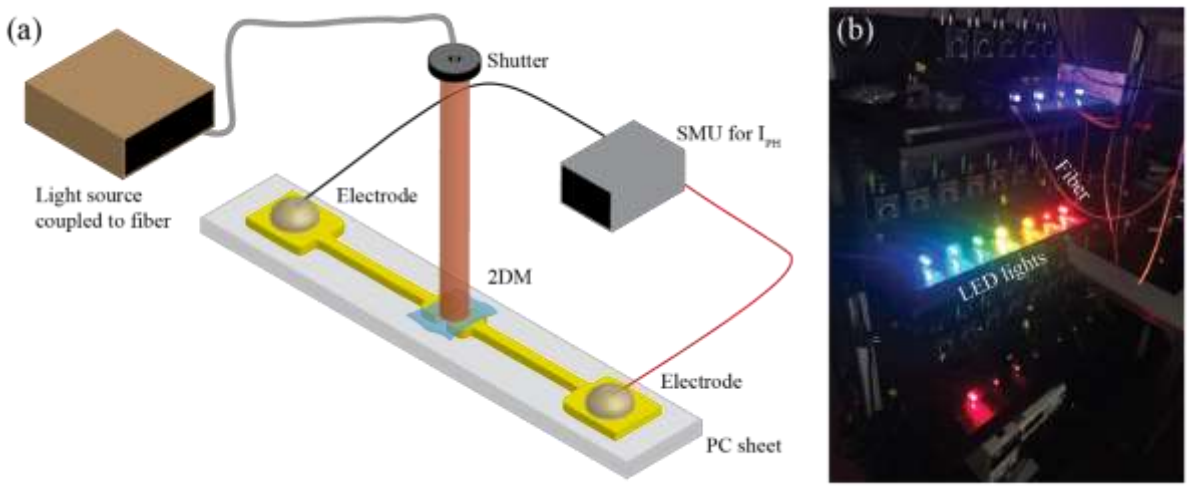

Figure 28. *Photocurrent setup. (a) Schematic illustration of photocurrent measurement. (b) LED light sources used for the illumination of MoS_2 photodetectors.*

2.5.3. FET

2DMs on Si/SiO_2 wafers were characterized in a FET configuration, as shown in **Figure 29(a)**. Au source and drain electrodes were fabricated by stencil or e-beam lithography (depending on the size of the 2DM), while the Si substrate was used as a back-gate. FET channels were fabricated with lengths from 10 µm to 100 µm and widths from 5 µm to 1500 µm. For mobility measurements, I-V sweeps were done, with constant drain-source voltage V_{DS} of 10 mV or 100 mV and gate voltage V_G sweeps up to 10 V or 100 V, depending on the Si wafer used and oxide thickness. For current measurement and voltage applications, two SM units were employed, the same as for previous transport characterisations. The field-effect mobility μ is extracted from linear regression done in the linear regime of the device I_{DS}-V_G curve, with the formula: $\mu =$

$\left(\frac{\partial I_{DS}}{\partial V_G}\right)\frac{1}{C_{OX}\frac{W}{L}}\frac{1}{V_{DS}}$. The I_{DS} and V_{DS} are the source to drain current and voltage, respectively, V_G gate voltage, W and L width and length of the channel. C_{OX} is the capacitance of the dielectric layer, i.e. capacitance between the channel and the back gate per unit area, calculated as $C_{OX}=\varepsilon_o\varepsilon_r/t_{OX}$, where $\varepsilon_o = 8.85\times10^{-12}Fm^{-1}$, $\varepsilon_r = 3.9$ and t_{OX} is the thickness of oxide, which was 85 nm or 270 nm. Measurements were performed in a custom-built vacuum chamber at the Institute of Physics in Zagreb with a pressure of 10^{-4} mbar, shown in **Figure 29(b)**, or in ambient conditions. Part of the constructed setup was pair of mechanical manipulators shown in **Figure 29(c)**, which worked as a probe station. As a result, multiple pairs of transistors can be tested on the same substrate without the use of a wire bonder or similar techniques. Results of fabricated Gr and MoS_2 FETs are shown in chapter **3.**. FET characterisation was not done on

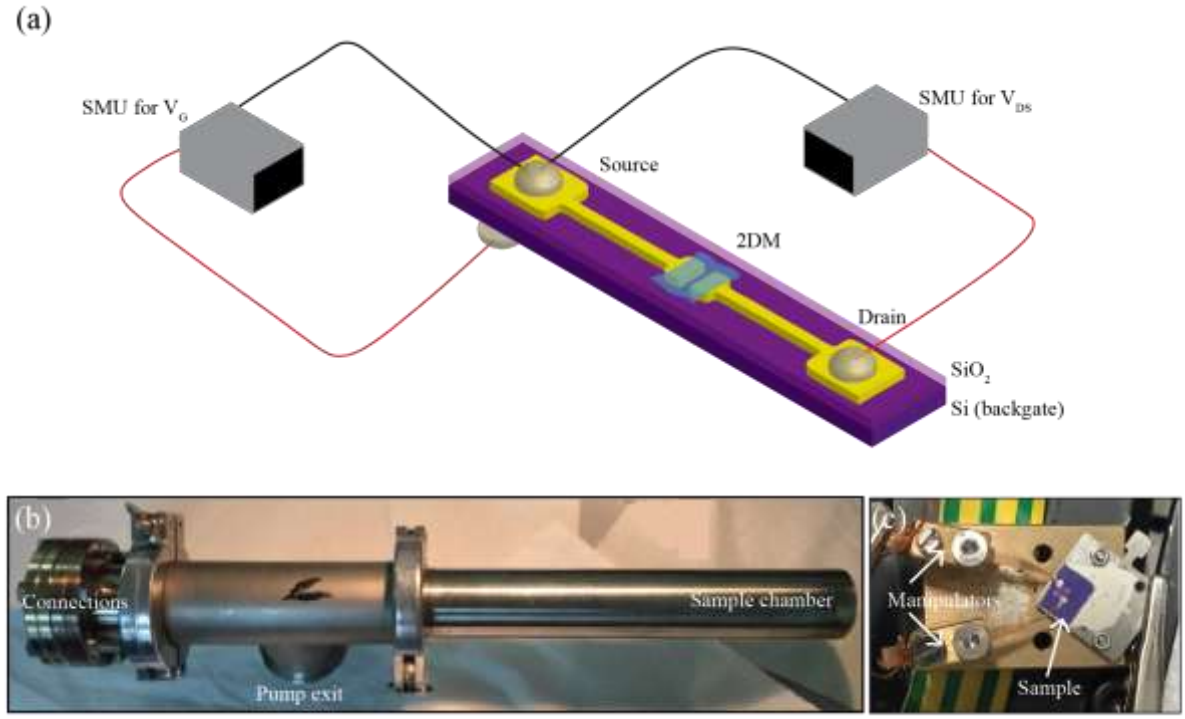

Figure 29. *FET setup. (a) Schematic illustration of FET characterisation. (b) Vacuum chamber built at IFZg. [Adopted from Ref. [156]] (c) Probe station that can be used inside the vacuum chamber or at ambient conditions.*

samples with a flexible substrate because the substrate is too thick to apply high enough electric field over the back gate. Unfortunately, there was no possibility to fabricate a dielectric layer on top of the electrodes and 2DM for top-gate measurements. For example, employing techniques such as ALD (atomic layer deposition) or MSD (magnetron sputtering deposition)

would enable the deposition of dielectric layers (i.e. HfO_2 and Al_2O_3) and subsequent fabrication of the top-gate electrode.[29]

2.6. Setups for application of strain

2.6.1. Two-point bending stage

By moving two manipulators along the same direction as the sample (i.e., substrate) extension, strain can be applied to the sample, as illustrated in **Figure 30(a)**. By decreasing the separation of the manipulators, the sample is bent, and strain is induced. Subsequently, separating manipulators afterward can return the sample to the initial shape. The exact amount of strain depends on the dimensions of the substrate which is used and can be calculated as $\varepsilon = 2T/R$ as shown in **Figure 30(b)**, where T is the thickness of the substrate and R is the curvature radius that can be determined by observing sideways the geometry of the sample with the camera.[86,91]

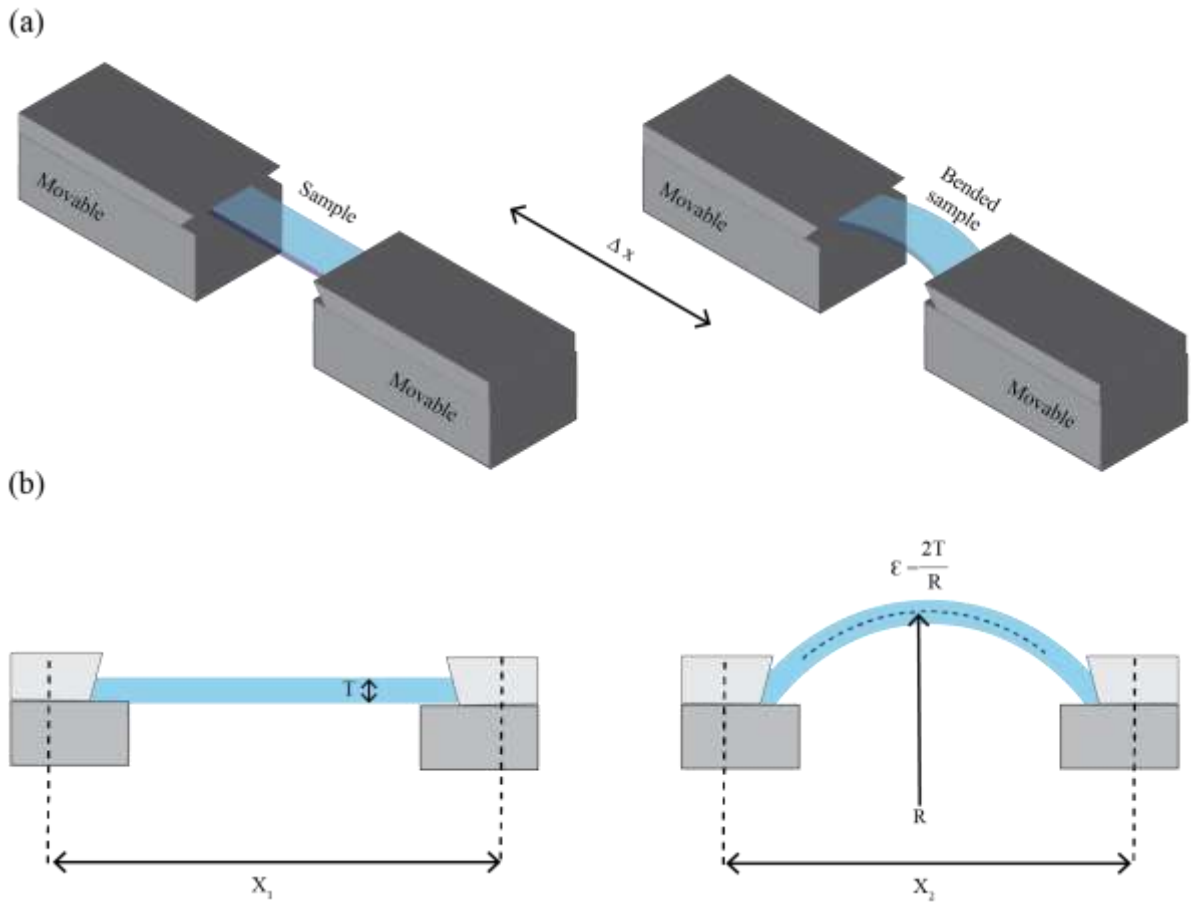

Figure 30. *Illustration of two-point bending setup. (a) Schematic of an unstrained and strained sample. Strain is induced by moving two manipulators towards each other and bending the substrate. (b) Side view of bending process with specified parameters for calculation of strain.*

With additional calibrations of the stage, the radius can be determined from the x movement of the stage. Since manipulators are manual and not motorized/automated, strain can be recalculated from recorded geometry afterward to eliminate human errors.

Two-point bending stage was used to apply uniaxial tensile strain in samples with flexible PC substrate of 500 µm thickness. The sample edges were fixed on two modified manipulators, each on the opposite side. Two stages were constructed at IFZg, one suitable for optical transmission characterisations shown in **Figure 31(a)** and the second for other characterisations in **Figure 31(b)**. This type of setup was used for strain-dependent measurements of MoS_2 monolayer absorbance and photoluminescence, described in detail in sections **5.1.** and **5.4.**.

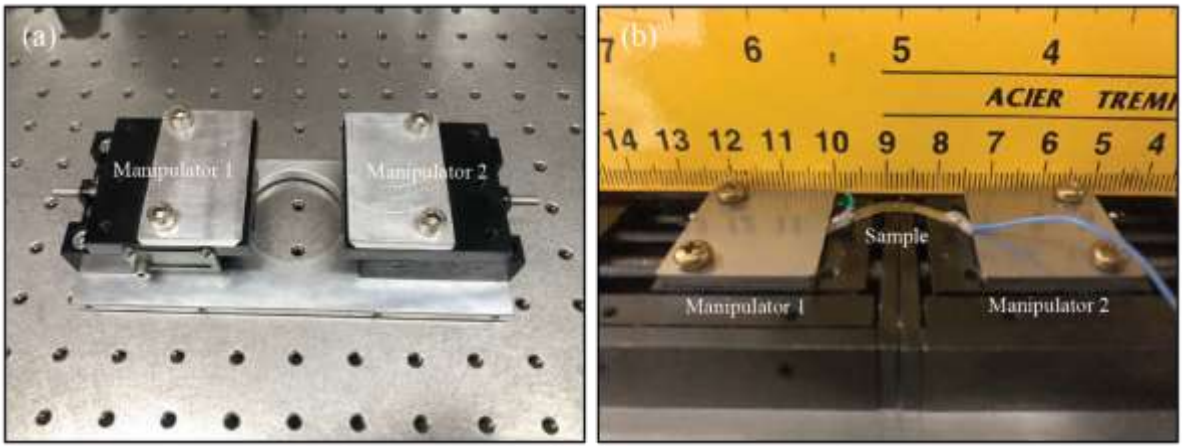

Figure 31. *Two-point bending setup. (a) Setup for larger samples and optical transmission characterisations. (b) Setup with a mounted sample bent by moving two manipulators towards each other during transport characterisation.*

2.6.2. Three-point bending stage

Three-point bending offers better control of the induced strain in the sample, which is achieved by fixing the targeted area of the sample over the middle rod. In that way, 2DM or device based on 2DM stays in the same position during the whole bending process, eliminating errors in optical characterisations that can occur due to defocusing (which can happen with a two-point bending setup). Furthermore, with the two-point stage, due to the geometry of the edges, a sample can move unintentionally if the edge of the sample moves relatively to manipulators. While with three-point bending, touching points are at the surface/bottom of the sample and not on the sides of the sample, preventing unwanted movement caused by the side edges of the sample.

Figure 32(a) shows a schematic of the bending process with a three-point bending setup by moving two rods vertically while the middle one is fixed.[157] Rods are covered with sticky tape that promotes adhesion of the rods to the substrate so that any unintentional movement of the sample is minimized. Two movable rods are connected via the same holder on the motorized manipulator, ensuring they have the same step. Before fixing the sample in the stage, movable rods are separated vertically from the fixed rod so that sample can be placed between them. After ensuring that the targeted part of the sample is placed in the middle of the fixed rod, edge rods are moved down to touch the edges of the sample, but only slightly so that bending would not start. Coordinates of the rods are saved as values for the 0 % of the strain. Next, the sample is bent by moving two rods down, as shown in **Figure 32(b)**. The exact amount of applied strain

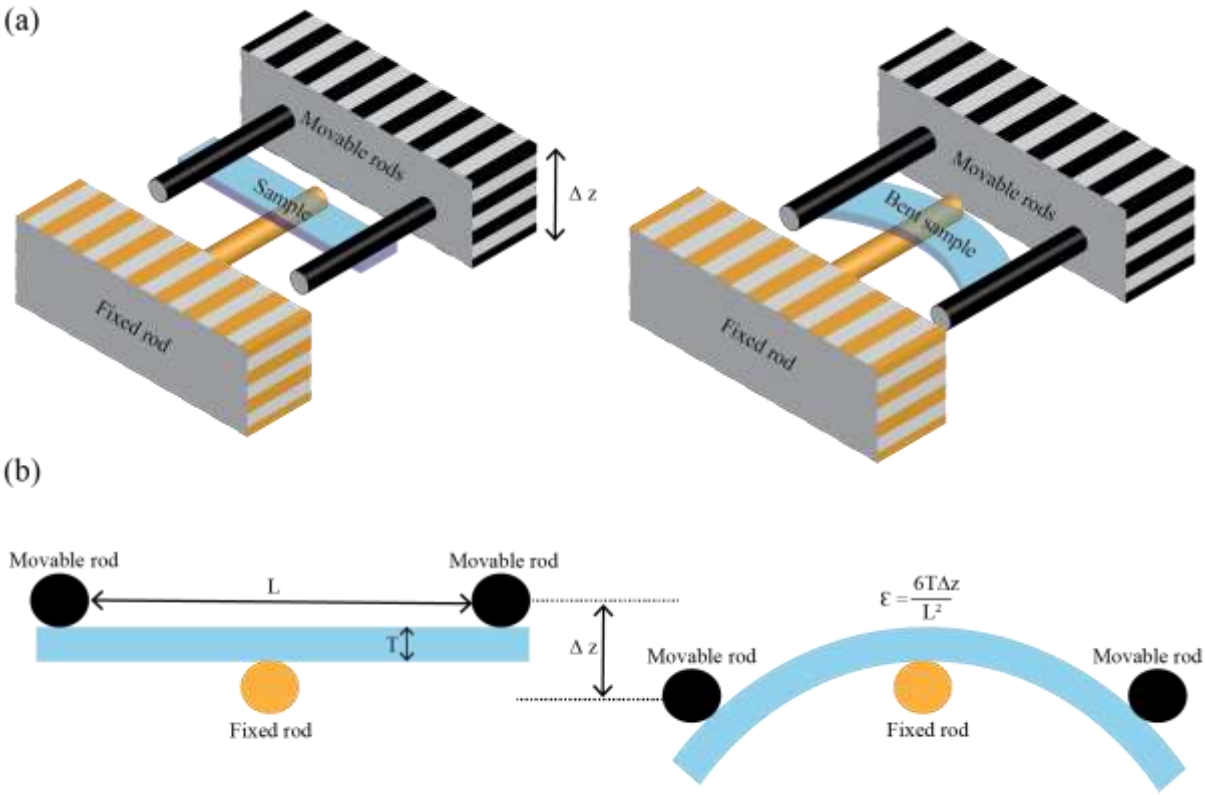

Figure 32. *Illustration of the three-point bending setup. a) Schematic of an unstrained and strained sample by bending achieved by moving two rods (located at the top of the sample edges) along the z-axis. (b) Side view of three-point bending process with specified parameters for calculation of strain.*

can be derived from $\varepsilon = 6T\Delta z/L^{2,}$ where T is the thickness of the substrate, L is a horizontal separation between two movable rods, and Δz is vertical movement.[73,75] By exploiting a

motorized stage calibrated for the specific thickness and length of the sample, measurements can be performed automatically over many cycles of bending and releasing.

Three-point bending stage was used to apply uniaxial tensile strain in samples with flexible PC substrate of 240 µm thickness. This stage uses three anchor points on the sample, two on the edges and one in the middle, as shown in **Figure 33(a)**, with indicated movable and fixed rods connected to motorized manipulators. By employing this method, part of the sample with 2DM or a device based on 2DM can be placed precisely in the middle of the fixed rod by observing their relative positions via an optical microscope, as shown in **Figure 33(b)**. This setup was used for strain-dependent measurements of the resistance in the MoS_2 strain detector and photocurrent in the MoS_2 photodetector, as described in sections **5.2.** and **5.3.**.

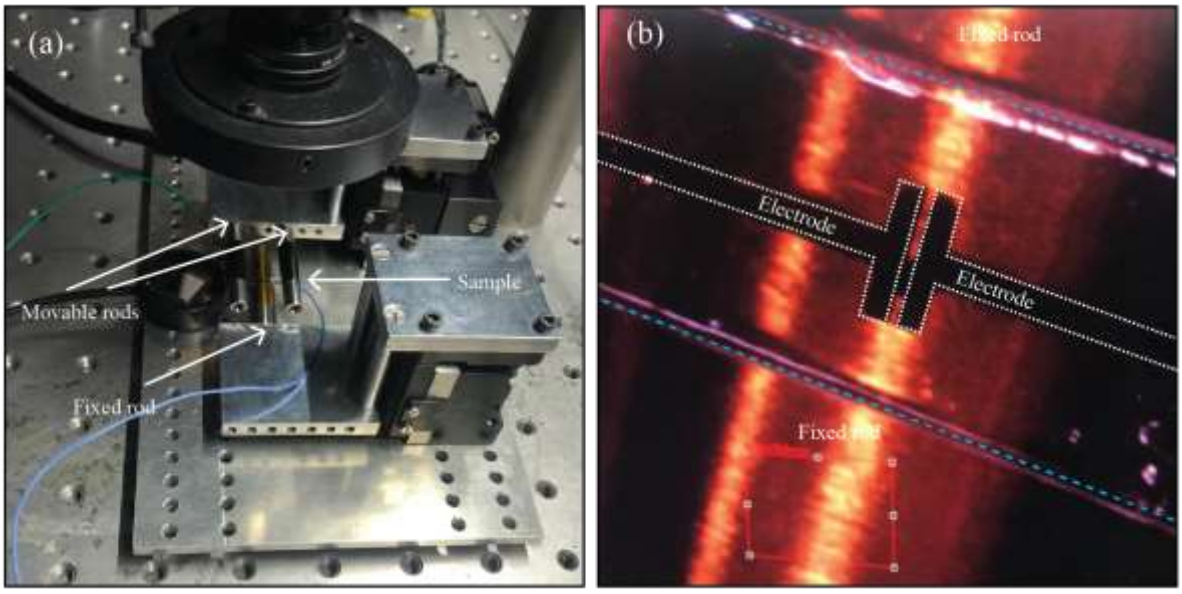

Figure 33. *Three-point bending stage. (a) Photograph of the motorized stage that was used. (b) Optical reflection image of the sample placed across fixed rod which ensures that the middle of the sample where 2DM is, stays at the same position while other two rods move edges of the sample and in that way bend it.*

Chapter 3

Fabrication of devices based on 2D materials

This chapter describes in detail the application of transfer and lithography methods to materials used in our work, i.e. to the substrate/2DM combinations studied in this thesis. Substrates used for the growth of 2DMs usually prevent the exploitation of materials and strain-dependent characterisations, which means that mechanical manipulation of 2DMs is needed after synthesis and initial characterisations on the growth substrate. We have constructed two setups for the transfer of 2DMs, electrochemical transfer for metallic substrates and stamping transfer for Si wafers. For fabrication of electrodes, which are necessary for 2DMs device utilization, stencil and e-beam lithography were exploited. Parameters for each method were carefully investigated until optimal ones were achieved for each combination of the 2DM and the substrate.

3.1. Transfer

3.1.1. Stamping transfer

Stamping transfer is a method for transferring 2DMs from the substrate on which they were grown or exfoliated onto an arbitrary substrate using a polydimethylsiloxane (PDMS) stamp or any similar polymer layer. Process itself can be carried out as all – dry method or with partial employment of the wet chemistry.[63,158,159] In the case of the transfer from the Si/SiO_2 wafers, usage of liquids is beneficial, and the liquid can be non-destructive, for example we used DI water. The process employs a thin water layer that, by gradual evaporation, changes the adhesion energy between 2DM and PDMS, enabling uniform pickup of the 2DM from the initial substrate onto the PDMS.[160] After the pickup step, 2DM was placed on an arbitrary substrate, e.g., patterned flexible PET or PC. To ensure that 2DM stays on top of the new substrate, one should gently press the stamp over a targeted substrate and then slowly separate the PDMS stamp, which provides gradual separation. The separation front can be easily observed via an optical microscope or camera.[63] Basis of this step is the viscoelasticity; with slow separation of the PDMS stamp, its viscoelastic properties change to ensure that the 2DM has more extensive adhesion to the targeted substrate instead of the PDMS.[117]

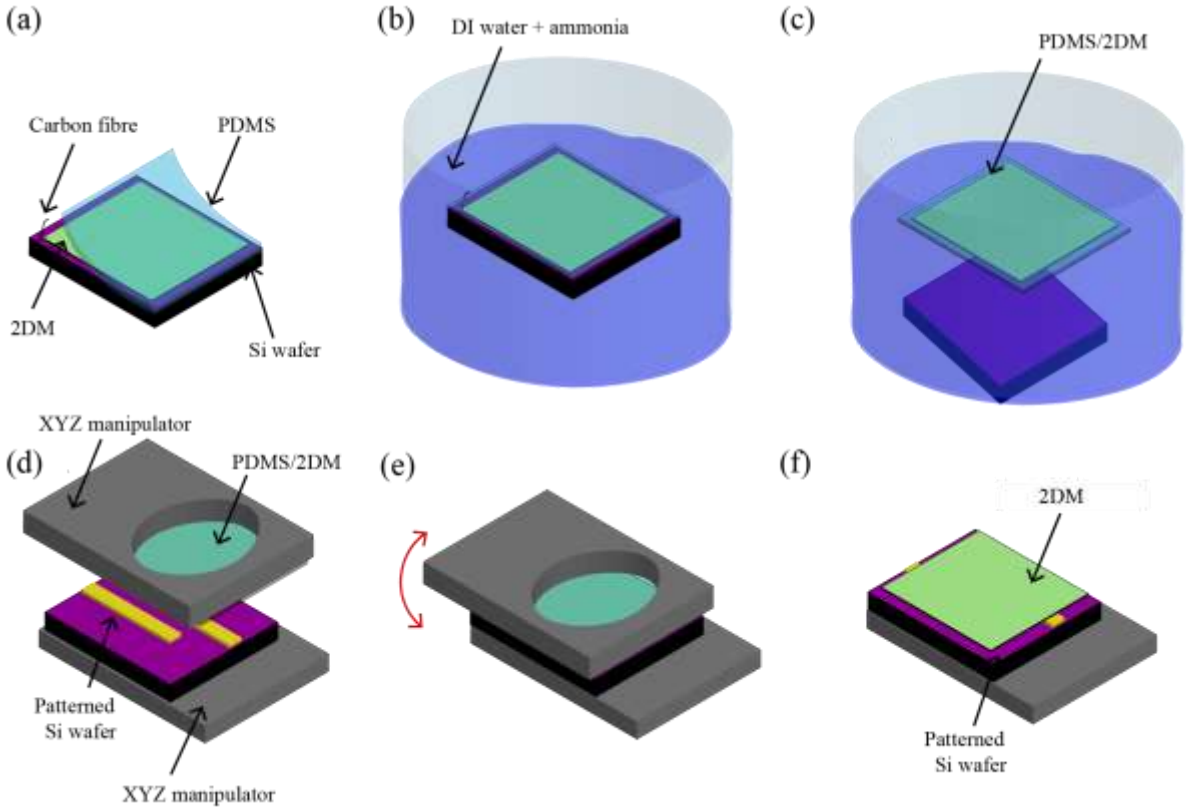

Figure 34. *Schematic of PDMS pick–up and stamping. ˙(a) PDMS layer is placed on top of 2DM grown on Si wafer. (b) The sample is placed to float on top of DI water and Ammonia solution. (c) PDMS//2DM is separated from the wafer that sinks to the bottom of the solution in a few minutes. (d) PDMS/2DM is positioned with an XYZ manipulator over the targeted area on the patterned substrate and connected and pressed slightly to ensure uniform adhesion to the substrate. (e) PDMS is slowly separated with a z-axis manipulator leaving 2DM on a new substrate. (f) 2DM is transferred onto the patterned substrate.*

In this work, PDMS sheets were bought from Gel Pack company. Larger sheets were cut onto smaller arbitrary shapes compatible with the substrate from which the 2DMs are transferred. The PDMS stamp is cut into a rectangle and placed on 2DM grown on Si/SiO_2 wafer, as illustrated in **Figure 34(a)**. To increase the speed of the next step, PDMS is left without contact on one of the edges of the Si wafer, which can be ensured by placing a carbon fibre or any similar object on the edge of the wafer before placing PDMS on top. **Figure 34(b)** shows an illustration of the pick-up step during which a PDMS / 2DM / Si wafer is placed on top of the solution of 100 ml DI water with a few drops of ammonia (100 µL), which is gently stirred in start to ensure the flow of the solution. The solution slowly intercalates between PDMS and Si wafer, separating 2DM from the Si wafer. After complete separation in a few minutes, Si wafer sinks into the solution, and PDMS with 2DM is left floating on top of the

solution, as shown in **Figure 34(c)**. Ammonia is known to dissolve alkali-like metals and is often used during the intercalation of 2DMs.[161] It is added into DI water to improve the removal of any ions that could dope 2DM s afterward, but pure DI water could also be used for this step.[162]

Figure 34(d) shows the step during which PDMS with 2DM is placed onto the substrate on which 2DM will be transferred. During placing, the PDMS stamp is gently pressed with an ear stick or simply by hand to ensure adequate adhesion over the whole substrate. This step is monitored by an optical microscope or camera and controlled with a set of micromanipulators with which one can precisely control the position and separation of PDMS and substrate.[63] To ensure that 2DM has higher adhesion with the substrate, PDMS is slowly separated in small steps with a z-axis manipulator, as shown in **Figure 34(e)**. After complete separation of PDMS, 2DM is left on top of the new substrate, as shown in **Figure 34(f)**. The front of the adhesion is monitored via an optical microscope to increase separation speed in the areas of no interest and reduce it in the areas where 2DM is targeted for transfer. **Figure 35.** shows a step-by-step stamping, PDMS with MoS_2 is slowly removed by increasing the z position of the PDMS with a micromanipulator. (a) – (c) were taken in 15 second intervals during the passing of separation front over MoS_2 flake.

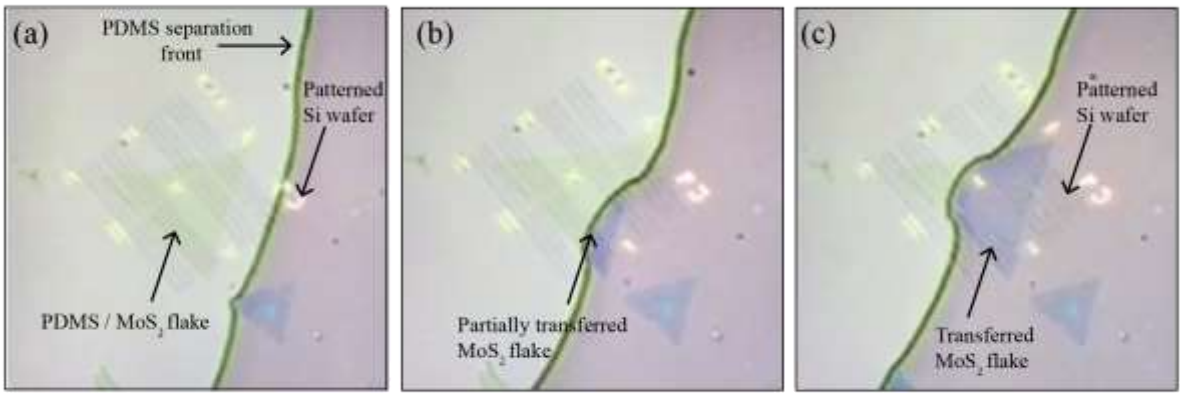

Figure 35. *Optical microscope images of PDMS removal. (a) PDMS separation front is brought in the vicinity of the targeted area by the Z manipulator, with the previous alignment by XY manipulators. (b) PDMS front is slowed with a Z manipulator over the targeted area and monitored during the process. (c) MoS_2 flake is transferred onto a targeted area of the patterned Si wafer.*

This method was used to transfer 2DMs on substrates such as PC and Si wafer, which can be previously patterned via lithography or have other 2DMs grown or transferred. For

instance, MoS_2 was transferred on top of the electrodes for transport characterisation, as shown in **Figure 36(a)** and **Figure 36(b)**, or on pillars also previously patterned via lithography to induce local strain, as shown in **Figure 36(c)** or on the second 2DM to form heterostructure as shown in **Figure 36(d)**. It is important to note that for some applications, there is no need to remove the PDMS in the final step. The PDMS layer can provide an additional supporting layer for the device but also can serve as a protective layer to decrease device degradation with time, which is often a problem with 2DMs.[163] For instance, PDMS was left to form a sandwich sample of PDMS/MoS_2/PC, which was used for absorbance vs. strain measurements used to determine strain transfer over cracks and grain boundaries.[139]

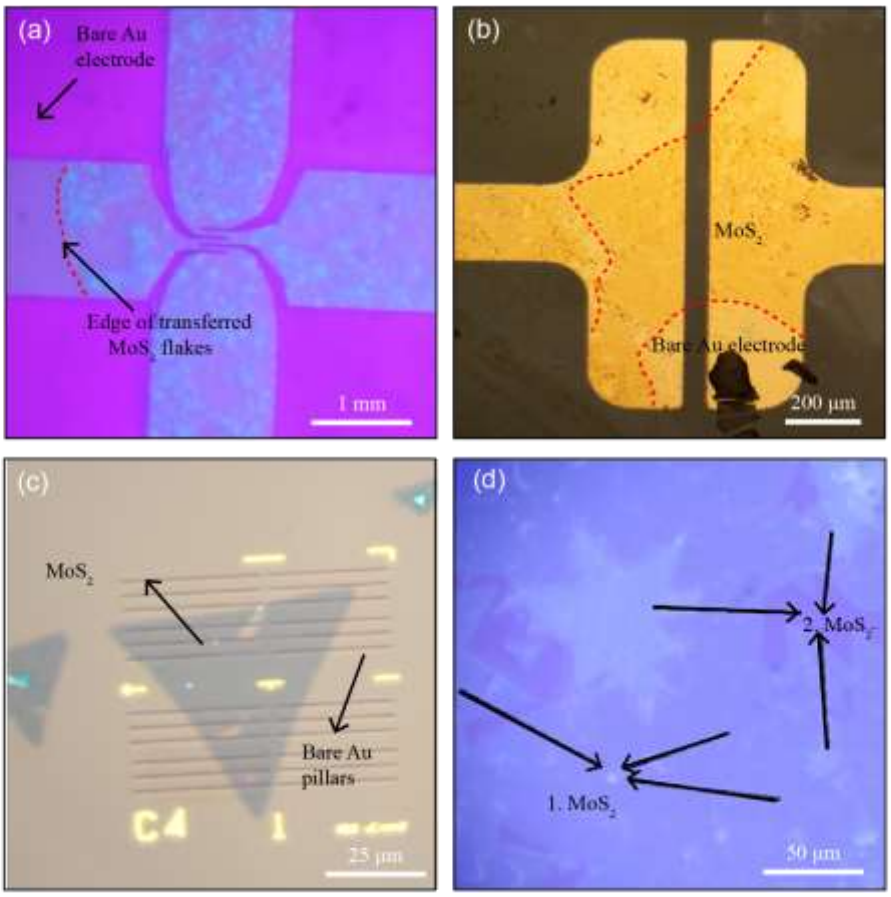

Figure 36. *Optical microscope images of transferred 2DM s via stamping method. (a) Flakes of MoS_2 monolayers transferred on electrodes fabricated by e-beam lithography for transport characterisation, (b) Sheet of MoS_2 transferred on electrodes fabricated by stencil lithography. (c) Flake of MoS_2 monolayer transferred onto Au pillars fabricated by e-beam lithography for local strain inducement, (d) Heterostructure constructed by MoS_2 transfer on top of the second layer of MoS_2.*

3.1.2. Electrochemical transfer

The electrochemical method has been previously employed for transferring Gr and hBN from metal substrates such as metallic single-crystal, e.g., Ir and Au, or metallic foils, e.g., Cu and Ni.[62,164,165] In contrast to the stamping method, electrochemical transfer employs reactive chemicals. However, it provides an alternative for removing 2DMs from metallic substrates, for which the stamping method has certain setbacks.[166] Previous reports of electrochemical methods used for transferring Gr and other 2DMs have made significant progress and detailed optimization of transfer parameters, which ensured a minimum of all defects in transferred 2DMs.

In our work, we have built a setup for electrochemical transfer based on previous reports, but with certain modifications of parameters and improvements needed for different 2DMs we investigated. We used a two-step electrochemical method to transfer 2DMs, such as Bo, Gr, and MoS_2/Gr, grown on Ir single-crystal and Cu foils. By applying potential difference on metallic substrate and platinum foil, which are immersed into NaOH solution, 2DMs with supporting PMMA layer above are separated from the substrate by intercalation and in case of foils with a certain amount of etching. This method is often called "the bubbling method" due to the formation of the small hydrogen bubbles at the metallic interface, which gradually expands across the surface of the metal substrate between 2DM.[167] A one-step electrochemical process was used for transfer from metallic foils (i.e., Cu foil), while a two-step electrochemical process was used for transfer from single-crystals (i.e., Ir (111)). In the case of foils, a certain amount of substrate can be etched due to voltage differences in NaOH or any similar solution. As a result, there is no need for the intercalation step used in the case of single-crystals prior to the delamination step. Also, with foils, reduced amounts of voltage difference are applied, resulting in smaller bubble size and lower reactivity to ensure that too much of the foil does not get etched.

A detailed scheme of the 2DM transfer via electrochemical method is demonstrated in the example of Bo, as illustrated in **Figure 37**. Step **(a)** represents Bo grown onto Ir single-crystal, but as previously mentioned, any other metallic substrate could be used. Step **(b)** shows the first electrochemical step, which is used in the case of single-crystals but can be skipped in the case of foils. The sample, Ir crystal with Bo on top (Bo/Ir) is immersed in a solution with a 100:1 ratio of MECN (methyl cyanide) and TOABr (tetra-n-octylammonium bromide). There, the Ir crystal acts as a cathode at a negative potential and a platinum foil, immersed in the same solution, acts as a positive anode. Upon application of a potential difference of 1.9 V between

the electrodes, intercalation of TOA^+ ions occurs.[168] The purpose of this step is to loosen the chemical bond between Bo and Ir substrate. Next, PMMA (~100 µL) is put on top of the sample and left to dry and solidify, as illustrated in step **(c)**. PMMA has a role of a carrier film providing mechanical support to the Bo layer in subsequent transfer steps.

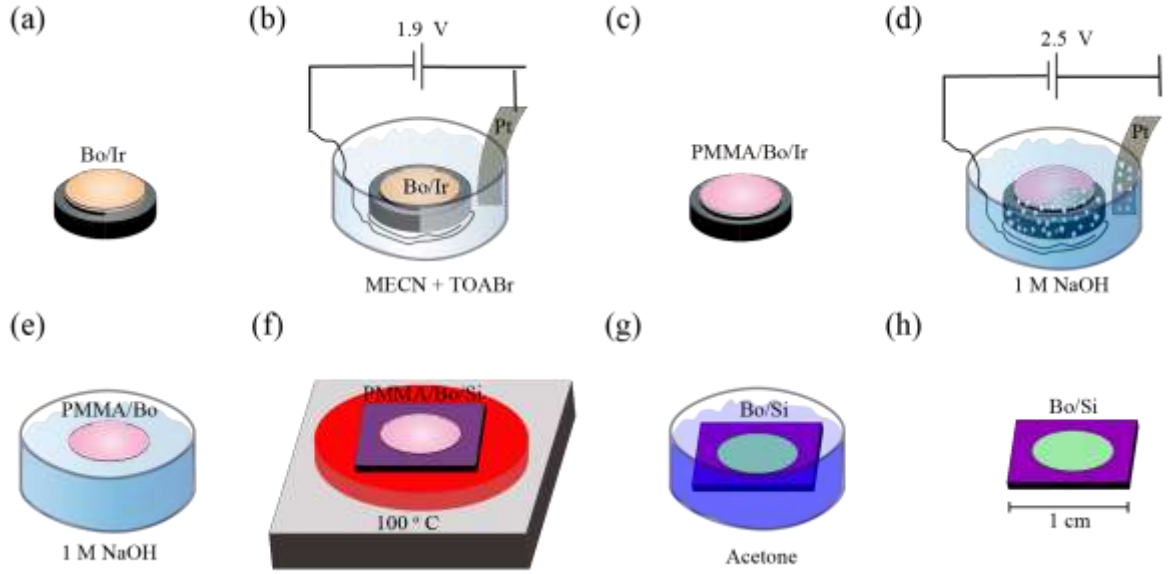

Figure 37. *Illustration of Bo electrochemical transfer from Ir single-crystal. (a) Bo is grown on top of the hat-shaped Ir single-crystal. (b) First electrochemical step during which intercalation occurs. (c) After intercalation surface is coated with PMMA. (d) Second electrochemical step during which delamination occurs. (e) As a result of delamination, PMMA with Bo is left floating on the solution's surface. (f) PMMA and Bo are scooped form the solution with the arbitrary substrate and placed on a hotplate to reduce wrinkles and folds. (g) PMAA is removed by immersing in acetone. (h) The process result is Bo transferred to the arbitrary substrate, e.g., Si wafer.*

After that, the second electrochemical step follows, where the PMMA/Bo/Ir (the cathode) is immersed in 1M NaOH solution together with the Pt foil (the anode). The sample is immersed gradually and with a tilt of 30° - 90° to improve the separation of PMMA/Bo. Next, a ramping potential difference of up to 2.5 V is applied, causing bubbles formation at the interface of Ir crystal and Bo, as shown in step **(d)**. With the formation of bubbles, PMMA/Bo gradually separates from the substrate (typically within 90 seconds), leaving it floating, as shown in step **(e)**. Subsequently, PMMA/Bo is thoroughly rinsed in deionized (DI) water and scooped with a piece of Si wafer (or any other substrate if desired). PMMA/Bo/Si is then placed on a hot plate for 30 minutes at 100° C, as shown in step **(f)**, to minimize residual chemicals and reduce transfer-induced wrinkling.[66] Afterwards, PMMA is removed by immersing

PMMA/Bo/Si into acetone for ten minutes and subsequent rinsing with DI water, as shown in step **(g)**. Finally, as a result of the entire process, Bo is left on top of an oxidized Si wafer Bo/Si, as shown in step **(h)**.

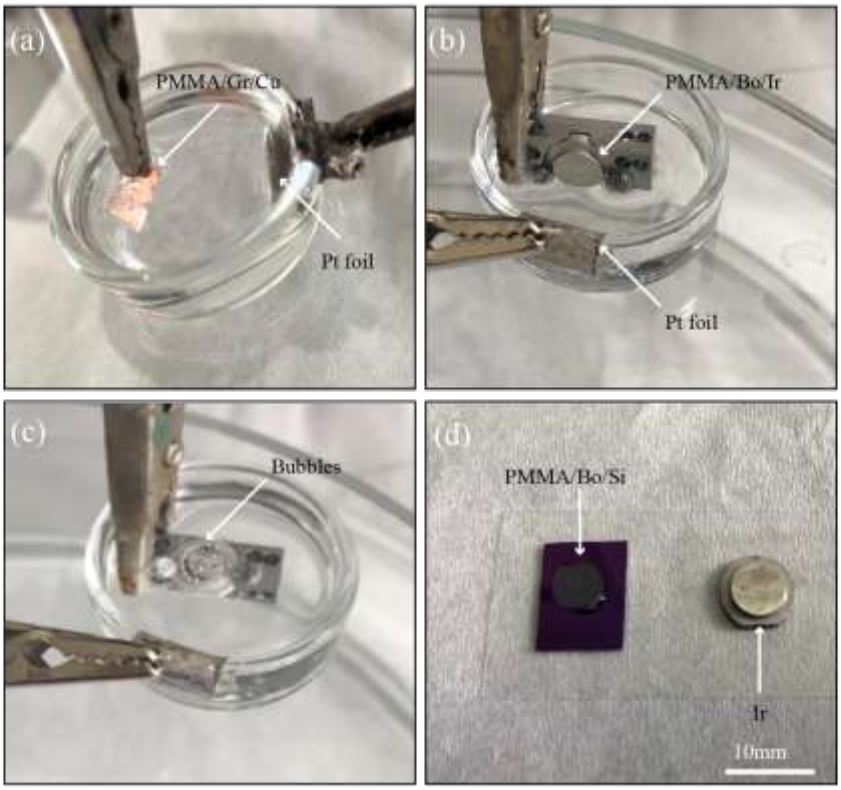

Figure 38. *Photographs of the transfer process from metallic substrates. (a) Transfer of Gr from Cu foil on which it was grown. (b) Transfer of Bo from Ir single-crystal on which it was grown. (c) Formation of the bubbles during the delamination step of Bo from Ir single-crystal. (d) PMMA/Bo layer scooped with Si wafer after electrochemical transfer from Ir single-crystal.*

Photographs of the transfer process of Gr from foil are shown in **Figure 38(a)** and transfer of Bo from single-crystal on **Figure 38(b)**. In addition, the formation of bubbles during the delamination step can be seen in **Figure 38(c)**. Finally, PMMA with Bo removed from Ir single-crystal is shown in **Figure 38(d)**. It can be seen that the shape of the transferred layer of PMMA/Bo is the same as the substrate on which it was grown, indicating that the size of the transferred Bo, or any other 2DM, is only limited by the size of the substrate on which 2DM was grown. To speed up delamination, we have scratched the edge of the surface to remove PMMA and open space for bubble penetration. Additionally, we have induced small waves on the surface by blowing air into the solution with a micropipette, to promote the separation of PMMA/2DM from the substrate.

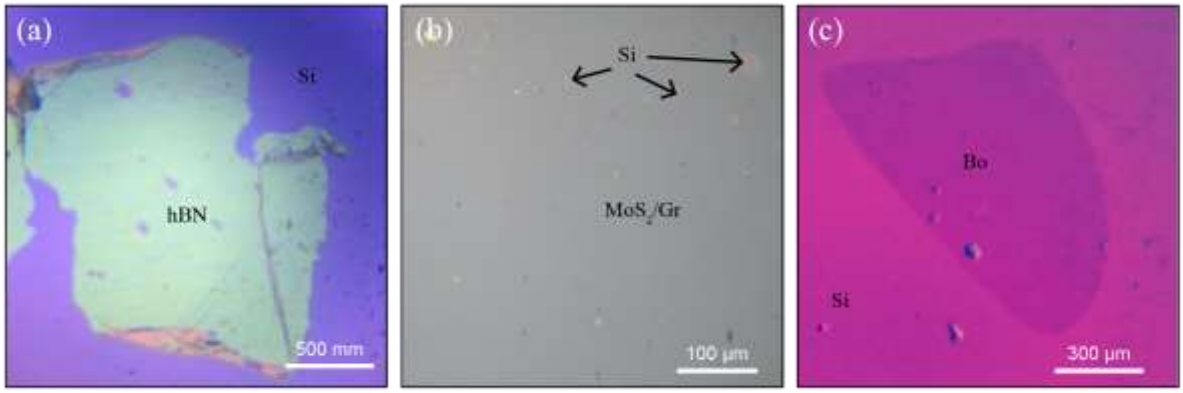

Figure 39. *Images taken by optical images of transferred 2DMs onto Si wafer via electrochemical transfer. (a) hBN transferred from Cu foil. (b) MoS_2 / Gr heterostructure transferred from Ir(111) single-crystal. (c) Bo transferred from Ir (111) single-crystal.*

First inspection of the transfer success was carried by optical microscope for a quick check of the transferred material. Better insight can be gained by employing AFM or SEM which is described in the following chapters regarding the characterisation of transferred materials and devices fabricated from them. In our work, electrochemical delamination was employed to transfer Gr, Bo, hBN, and MoS_2/Gr heterostructure from Ir (111) single-crystal and Cu foils.[133,138] **Figure 39(a)** shows an optical image of a transferred hBN monolayer grown on Cu foil. This method was used to transfer MoS_2/Gr heterostructures, as shown in **Figure 39(b),** and for transferring chemically reactive materials as Bo, as shown in **Figure 39(c)**.

Depending on the substrate and the 2DMs, slight variations in the potential difference, selection of solutions and polymers were used to improve the success rate of the transfer.[62] Further improvements for our method of transfer can be divided into three groups: (i) Optimization of voltage ramping rates and final values during electrochemical steps of the transfer, which affect the size of hydrogen bubbles and with that also the volatility of the electrochemical steps, (ii) Utilization of a second polymer, which would be placed above the first supporting layer (PMMA in our case), one could achieve better mechanical stability of transfer which would minimize folding of the PMMA, (iii) Utilization of polymers other than PMMA as mechanical support, as well as the use of polymer removers other than acetone.

3.2. Lithography

3.2.1. Stencil lithography

Stencil lithography with mechanical masks provides a fast method for contact fabrication on an arbitrary substrate with any shape with limited minimum dimensions in the micrometer range.[169] Basis of stencil lithography is the physical prevention of deposited material from reaching certain areas of the substrate on which electrodes are fabricated. In our work, mask with an arbitrary shape was placed on top of the substrate and subsequently placed into the metal deposition chamber. After the thermal evaporation, mask was removed, leaving the metal only in the substrate regions left exposed, i.e., in the cut areas of the mask, as the illustration in **Figure 40** shows. We have used thermal evaporation system for metal deposition in our work, but any other similar method, such as sputtering, can be used.

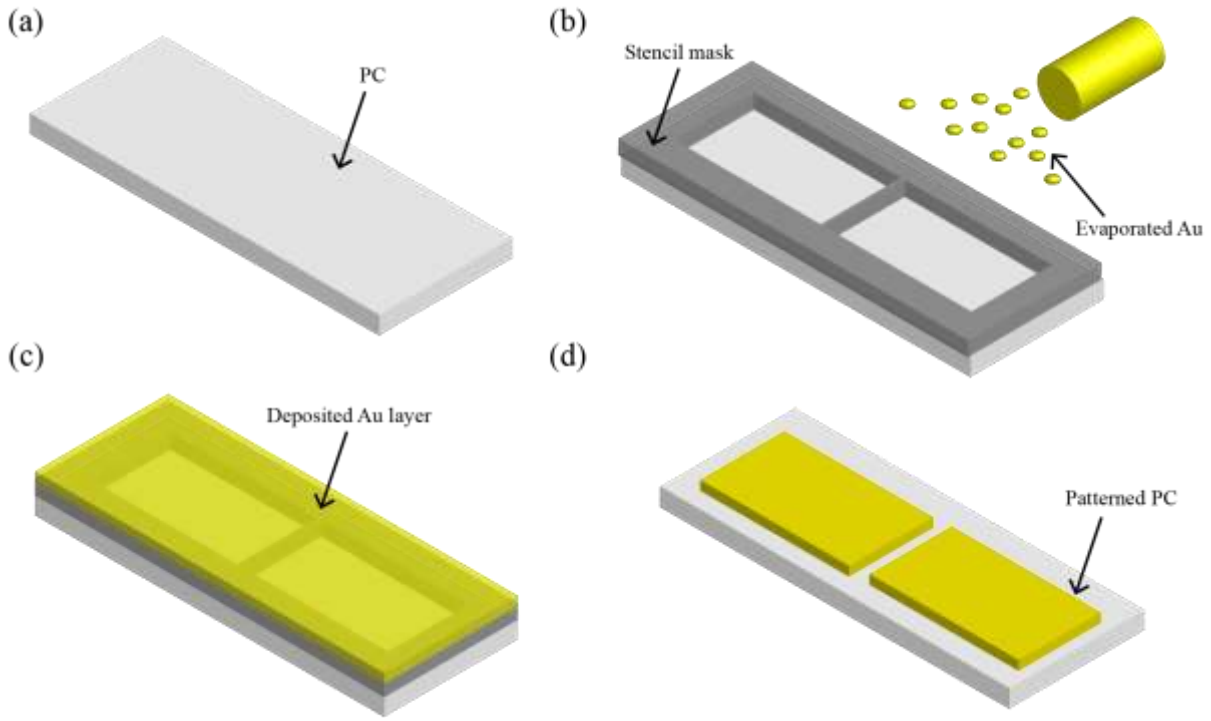

Figure 40. *Scheme of stencil lithography. (a) Bare PC substrate. (b) The stencil mask is positioned on top of the substrate, after which the sample is placed in a metal evaporator chamber. (c) Evaporated Au layer covers the whole surface of the sample. (d) After removing the stencil mask, Au is left on the areas unprotected by the mask, leaving Au electrodes with the configuration designed with the stencil mask.*

Masks used as stencils were custom-made or bought from commercial suppliers, which can adapt their product for specific requests given the shape of the contacts. Generally, two

shapes were used for the need of this research, simple custom-made square configuration yielding electrodes illustrated in **Figure 41(a)** or bought foils with two expanding fin providing electrode configuration illustrated in **Figure 41(b)**.

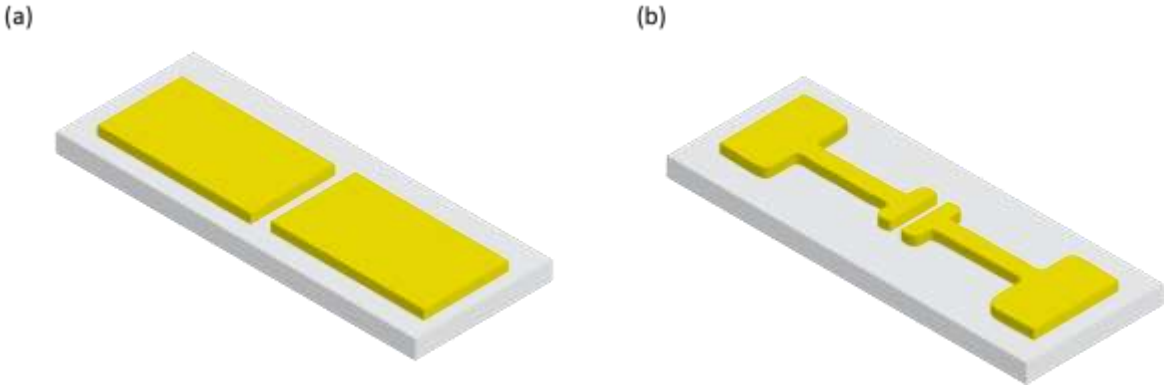

Figure 41. *Schematic representation of configuration of the electrodes. (a) Custom-made shape, (b) Bought stencil shape.*

The most significant benefits of this method are the fabrication speed and the avoided usage of any chemicals. Because the mask used for the process was repeatedly used, there was no need for mask design and fabrication each time, which is one of the most time-consuming steps for e-beam lithography. In case of targeted fabrication of electrodes on specific positions on the substrate, for example, in the areas covered with 2DMs, masks were delicately placed under the optical microscope on desired positions and fixed with a small amount of tape or any thermally resistant glue. However, when 2DMs that are targeted had the same lateral size as the gap between the electrodes, targeting specific areas was to much time-consuming. In those cases, 2DMs were transferred on top of the contacts with the method described in the previous section.

In the case of stencil lithography, the substrates were arbitrary (i.e., Si wafer and PC sheet) with no limitations regarding conductivity or reactivity with various solvents, that presents a setback for e-beam lithography. After the process, electrodes had the shape defined by mask, and their thickness was determined by the duration of the metal deposition, which was monitored in situ with a QCM sensor. In **Figure 42(a)** optical image and **(b)** SEM image of fabricated electrodes are shown, while **(c)** shows an AFM image of the electrode edge. After deposition of the materials, the success of the process was determined by inspection via various microscopes. An optical microscope was used to quickly determine whether the electrodes have the desired shape and whether channels between electrodes are clean or have some contaminations. SEM and AFM were employed to gain more detailed information on the

morphology of the electrodes, their uniformity, and the thickness of the deposited metal. Usually, during the evaporation, metal gets accumulated around mask features, resulting in increased height on the edge of the electrodes.[169]

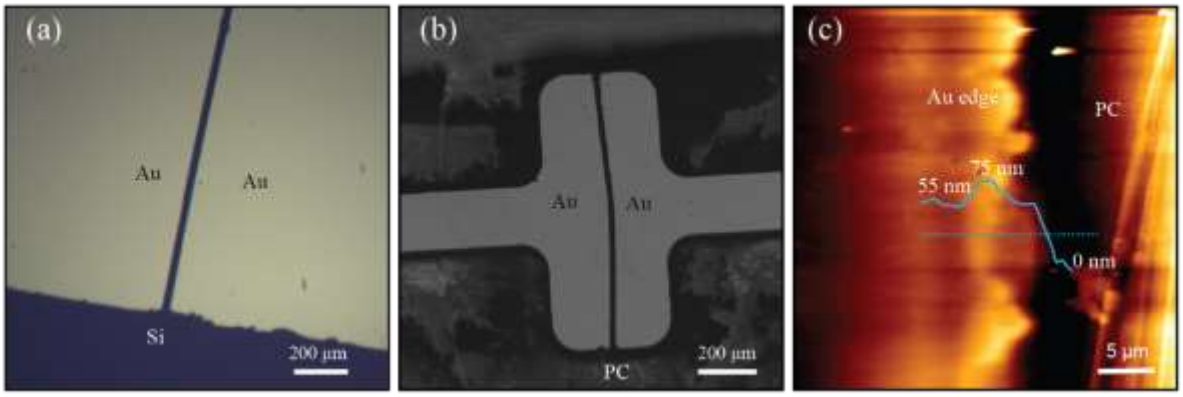

Figure 42. *Images of electrodes patterned on by stencil lithography. (a) Optical microscope image of electrodes fabricated on Si wafer with custom-made masks. (b) SEM image of electrodes fabricated on PC with bought masks. (c) AFM topograph of Au edge on PC, with a line-scan, indicated by a blue dashed line, taken over the edge of electrode of thickness around 55 nm.*

3.2.2. E-beam lithography

E-beam lithography is a method that utilizes polymer reactivity upon irradiation with an electron beam, usually generated with an electron microscope. In that polymer, the pattern can be imprinted with selective exposure. A schematic illustration of e-beam lithography is shown in **Figure 43. Figure 43(a)** shows the first step, placing a drop of polymer sensitive to an e-beam, e.g., PMMA or CSAR were bought from the All resists company. After dropping 50µL to 100µL of polymer, the sample is spin-coated to achieve uniform distribution around 2000 rpm – 3000 rpm depending on the wanted thickness of the coated layer, as shown in **Figure 43(b)**. Subsequent to spin-coating, the sample is placed on the hotplate on temperatures around 100°C for 5 to 30 minutes to promote solidification of the coated polymer, as shown in **Figure 43(c)**. In the case of e-beam lithography on highly insulating substrates, the additional conductive polymer is placed over the polymer for patterning, with the same three steps used for the first layer. The conductive polymer is used to promote the diffusion of excess electrons, resulting in improved resolution of the process. Following the initial steps, the sample is placed in an SEM chamber for e-beam exposure. The electron beam is adjusted previously to ~10 mm WD and beam size around of approcimately 100 nm and set for BI exposure of ~10. After that,

the exposure location is set with an adequate dose of 90 – 250 μC/cm^2, depending on the polymer used.

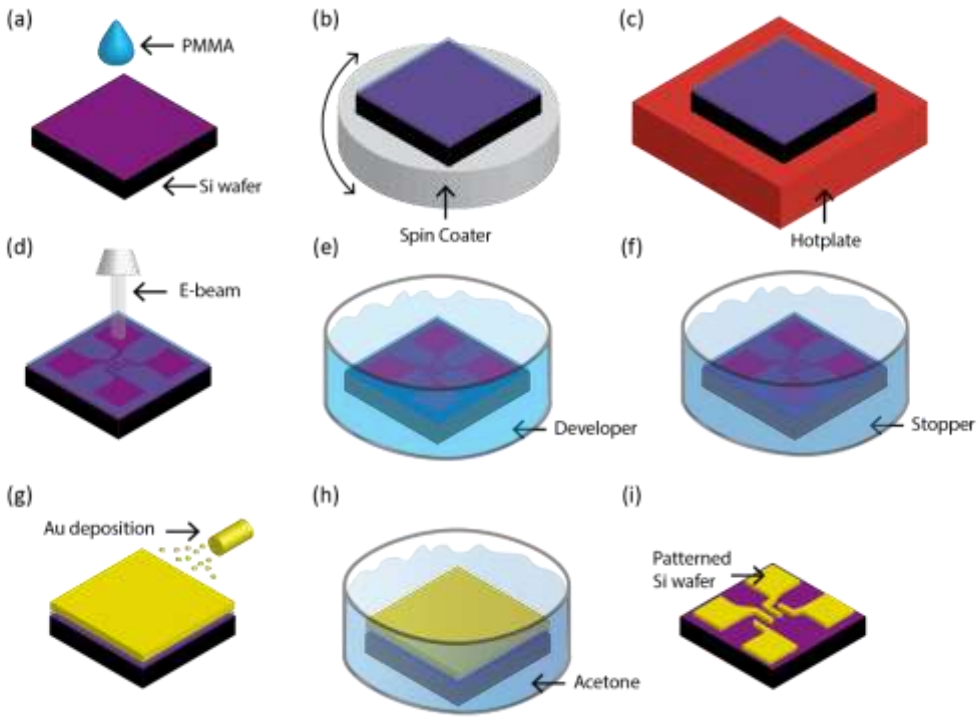

Figure 43. *Scheme of e-beam lithography. (a) A 50 μL drop of PMMA is placed on the Si/SiO$_2$ wafer. (b) Afterwaards the sample is spin-coated for uniform distribution of PMMA. (c) Sample is heated on a hotplate to promote solidification of the PMMA. (d) PMMA layer is patterned by e-beam. (e) After e-beam exposure, the sample is placed into a bath of developer solution. (f) Subsequently a sample is placed into a bath of stopper solution. (g) Au is deposited on the surface of the sample. (h) PMMA layer is removed by rinsing into acetone bath. (i) After removal of PMMA layer, Au is left with shape and positions patterned into PMMA layer.*

Lithography is done in the areas previously defined with CAD software, incorporated with the SEM microscope interface, as shown in **Figure 43(d)**. In case of targeted patterning, e.g., placing electrodes over a specific flake of 2DM, the sample is imaged with SEM to acquire the exact position of targeted flakes before polymer coating. To achieve precise positioning, three objects that will be visible after coating are imaged with SEM with exact coordinates to form a coordinate system used in CAD software. After coating, the same three objects are located, and coordinates are aligned with previously acquired ones. In CAD software, one can import SEM images with exact locations and create a pattern in software that will be imprinted into the polymer, as shown in **Figure 44(a)**. Following the e-beam exposure, the sample is placed in developer solution to promote the removal of polymer in the areas exposed to the e-

beam, as shown in **Figure 43(e)**, and subsequently into stopper solution to prevent further disintegration of the polymer, as shown in **Figure 43(f)**.

As a result, exposed areas of polymer are removed from the surface, leaving a patterned shape with respect to targeted flakes of 2DMs, as shown in **Figure 44(b)**. Next, samples with patterned polymer are rinsed with DI water and placed into a metal evaporation chamber, during which evaporated metal covers the whole surface of the sample, as shown in **Figure 43(g)**. In the end, the sample is rinsed with acetone or placed into a bath for 30 minutes to remove polymer and excess deposited metal over it, as seen in **Figure 43(h)**. In addition, the sample can be rinsed in other removers or heated up to 70°C to improve the lift-off step. The result of the entire process is deposited metal in the areas patterned with e-beam, as illustrated **in Figure 43(i)**. In the case of targeted patterning, electrodes are placed in the exact position and shapes created in CAD software, as shown in **Figure 44(c)**.

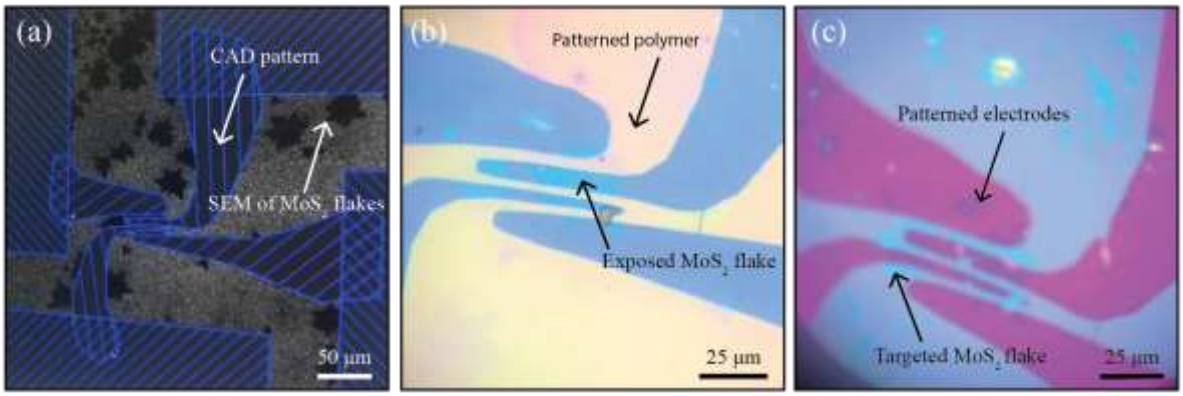

Figure 44. *Process for targeted e-beam patterning. (a) Screenshot of CAD design pattern with imported SEM image with coordinates of targeted MoS_2 flakes. (b) Optical microscope image of the patterned polymer after e-beam exposure and chemical processing. (c) Optical microscope image of fabricated Au contacts on the targeted MoS_2 flake.*

As previously mentioned, electrodes can be fabricated on many substrates, including oxidized Si wafer and PC sheet used as a primary choice for fabrication of devices through this thesis. **Figure 45(a)** shows an array of patterned electrodes on top of a bare oxidized Si wafer damaged during the lift-off step, as visible by scratches and residual material in the vicinity of electrodes. An example of good lift-off of an array of electrodes ready for use is shown in **Figure 45(b)**, and one set of electrodes for transport characterisation is displayed in **Figure 45(c)**. As previously stated, electrodes can be fabricated directly on 2DM, or 2DM can be transferred on them subsequently. With e-beam lithography, nm-size structures can be patterned, which is three to four orders of magnitude less than with stencil lithography. Usage

of various solutions in this process and exposure to e-beam can influence 2DM if they are present in the process.[170,171] That can be avoided by transferring 2DMs onto patterned substrates via any of the previously described methods.

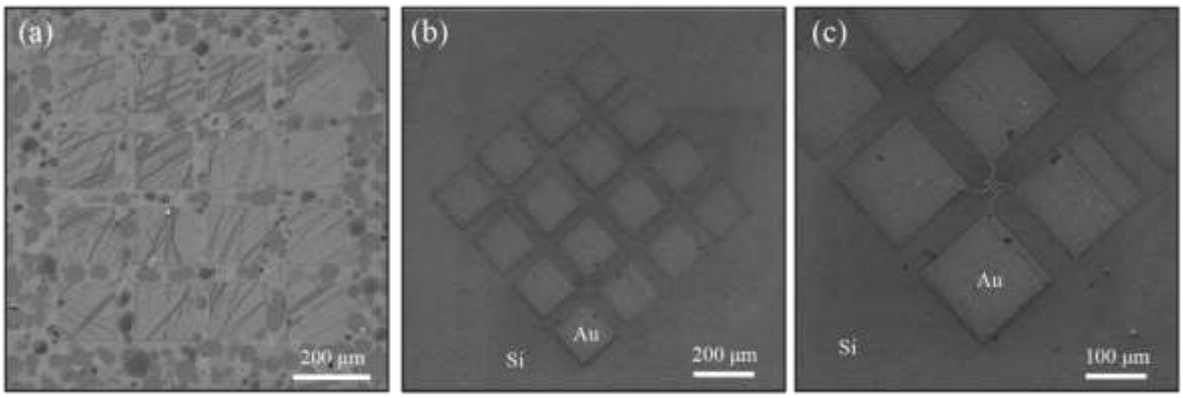

Figure 45. *Examples of e-beam lithography. (a) SEM image of an array of electrodes on the clean substrate with an unsuccessful, partial lift-off. (b) SEM image of an array of electrodes with a successful lift-off. (c) Zoomed in SEM image of patterned electrodes in fin configuration for transport characterisation.*

Chapter 4

Characterisation prior to strain application

This chapter discloses characterisations of Bo, Gr, MoS_2 monolayers, and MoS_2/Gr heterostructure before applying any strain to them. A comprehensive study of their properties at ambient environment and in pre-strain state is required to determine which materials would be suitable for the sensors and transistors. Materials were characterised on their growth substrates, and subsequently on the substrates they were transferred to or on which they were incorporated into devices. For instance, various types of MoS_2 samples are characterised by AFM and SEM, and by Raman and PL spectroscopy prior to employing them for any devices. After electrodes are fabricated or after the 2DMs are transferred to a second substrate, samples are again characterized with the same techniques to carefully determine which samples and specific batches are suitable for further processing. After the first round of characterisations, devices based on 2DMs are invetigated. Materials conductivity and mobility in FET configuration are determined and doping effects are investigated by PL spectroscopy.

4.1. Bo

4.1.1. Bo on Ir (111)

One of the key questions for exploiting Bo are its ambient stability and the possibility of mechanical manipulation due to its reactivity. Therefore, after ambient exposure, Bo on Ir(111) was characterized with SEM, AFM, and Raman spectroscopy.

SEM can provide an overview of the Bo surface on Ir single-crystals, on which samples were grown, as seen in **Figure 46(a)**. With higher magnification, substrate terraces are distinguishable, as shown in **Figure 46(b)**, but the Bo monolayer is not easily resolved. Although no detailed information on Bo quality is gained with SEM, one can determine which substrate areas are suitable for further analysis with AFM.

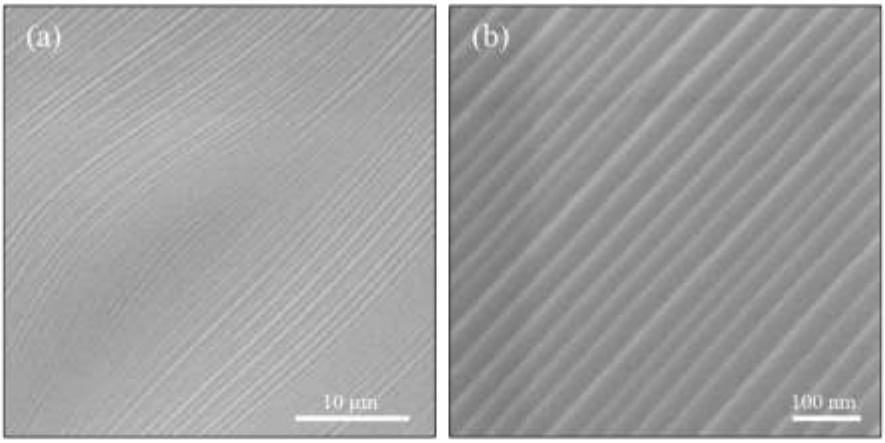

Figure 46. *SEM image of Bo on growth substrate. (a) Bo on Ir single-crystal. (b) Zoom in at Bo on Ir single-crystal.*

AFM measurements confirm that essentially the entire surface is covered with a monolayer of Bo, in agreement with the study by Omambac et al., where a similar synthesis approach has been employed.[36] This is visible in a large-scale topographic image in **Figure 47(a)**, where Bo spans over many terraces. The corresponding phase image, shown in **Figure 47(d)**, confirms full coverage and the absence of other materials on the surface. However, it should be noted that Bo can oxidize when exposed to air, as has been shown by *ex-situ* XPS measurements of the χ_6 polymorph.[36] Studies of other polymorphs have shown that only a portion of B atoms get oxidized upon exposure to air, and oxidation is found to be much more pronounced at Bo island edges.[39,47,48,172,173] By considering that our sample dominantly consists of fully covered Bo regions, void of free edges, we presume that our Bo sample is not necessarily fully oxidized.

Segregation-assisted epitaxial growth of Bo is known to result in the repositioning of Ir steps and the formation of wide terraces bounded by step bunches.[36] This is also evident from the line profile shown in **Figure 47(g)**, extracted from the area indicated by an arrow in **Figure 47(a)**. The profile shows that the height difference between neighboring Bo-covered terraces ranges up to 30 Å. Since the monoatomic step height on the Ir(111) surface is measured to be 2.4 Å,[174], it is easy to calculate that the step bunch, in this case, contains as many as thirteen Ir monoatomic steps. Additionally, Ir step bunches intersect under different angles, which is not a feature of clean Ir surfaces and is also attributed to Bo growth process. Generally, *ex-situ* AFM characterisation indicates that exposure of Bo to air did not induce any notable morphological changes in the material. It is also important to note that no growth-induced wrinkles have been observed for Bo on Ir(111), similar to hexagonal boron nitride (hBN) on

Ir(111)[134] and in contrast to Gr on the same substrate.[175,176] This finding signifies a rather weak interaction between Bo and Ir, or a negligible mismatch of thermal expansion coefficients of Bo and Ir.

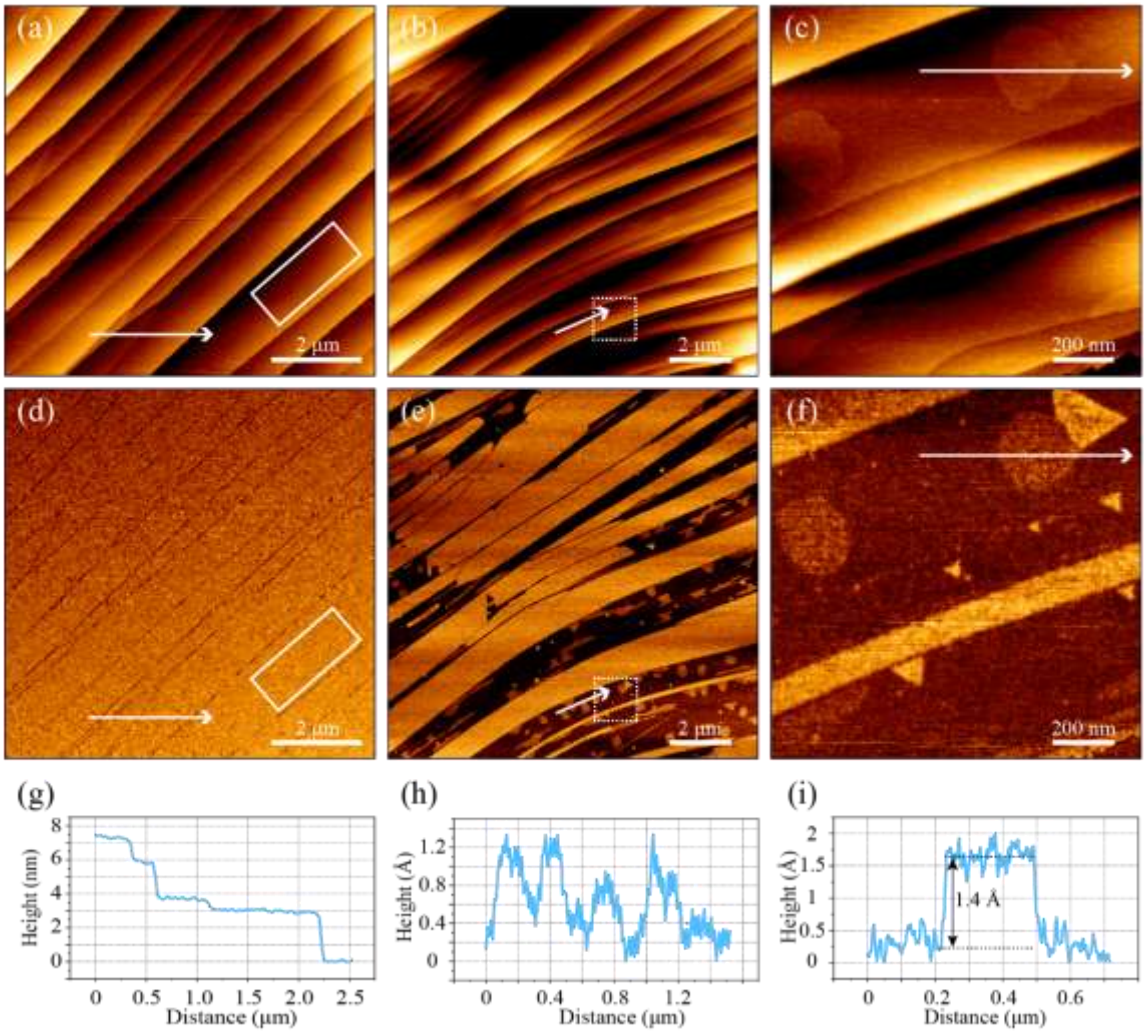

Figure 47. *AFM imaging of Bo on Ir crystal. (a) Area with a full Bo coverage, white rectangle indicates region inspected for roughness analysis. (b) Area partially covered with Bo sheets and isolated Bo islands. (c) Zoom-in into the area marked in (b) by a white dashed square, with isolated Bo (circular in shape) and residual hBN islands (triangular in shape). (d), (e) and (f) Phase images of (a), (b) and (c), respectively. (g), (h) and (j) Line profiles from (a), (b) and (c), respectively, as indicated by arrows. Image flattening was performed prior to profile extraction. [Adopted from Ref.* [133]*].*

Systematic AFM scanning across the entire sample surface was performed to find regions with sub-monolayer Bo coverage. Such regions enable topographic AFM characterisation inaccessible in full-coverage regions, such as Bo height measurement. Those

regions are scarce and were dominantly located close to the physical edge of the Ir crystal. One such region is shown in **Figure 47(b)**, **(e)** and **(h)** (topography, phase, and line profile, respectively), where partially covered Ir terraces, sometimes decorated with individual Bo islands, can be seen. These features are apparent in the AFM phase image, where dissimilar materials yield different contrasts. The observation of a typical terrace-filling flat material morphology, which has been identified before in LEEM,[36] confirms that the layer covering the Ir surface is indeed Bo.

A zoom-in of the region indicated in **Figure 47(b)** and **(e)** by a dashed white square is shown in **Figure 47(c)** and **(f)** (topography and phase, respectively). There, individual Bo islands can be clearly resolved, especially in the phase image. A topographic line profile across one such island is shown in **Figure 47(i)**, yielding Bo height of 1.4 Å. However, it is important to note that our measured Bo height varied from 0.9 to 1.5 Å, depending on the tip and the image acquisition parameters used. Such variations are a known property of AFM imaging of 2DM s.[177] For comparison, the reported AFM height of Bo on Cu(111), which is categorized as more weakly bound system,[135,136] is 3 Å.[178] In our work, Gr height on Ir(111) single-crystal was in range of 0.6 to 1.2 Å. In addition to the individual Bo islands, regions with $\Theta_{Bo} < 1$ sometimes contain small triangular islands with two distinct, 180°-rotated orientations, as visible in **Figure 47(f)**. These are ascribed to remnants of hBN formation on Ir, which can locally occur due to the nature of the segregation-enhanced Bo growth mechanism: the competition between hBN formation and hBN disintegration accompanied by boron dissolution and resurfacing.[36,134] hBN islands essentially vanish as the Bo coverage increases.

4.1.2. Bo on Si/SiO$_2$ wafer

After Bo transfer to Si wafer, via electrochemical transfer described in detail in subsection **3.1.2.**, SEM, AFM, and Raman were employed again. In contrast to Bo on Ir, SEM inspection can provide more details after the transfer to a Si wafer.

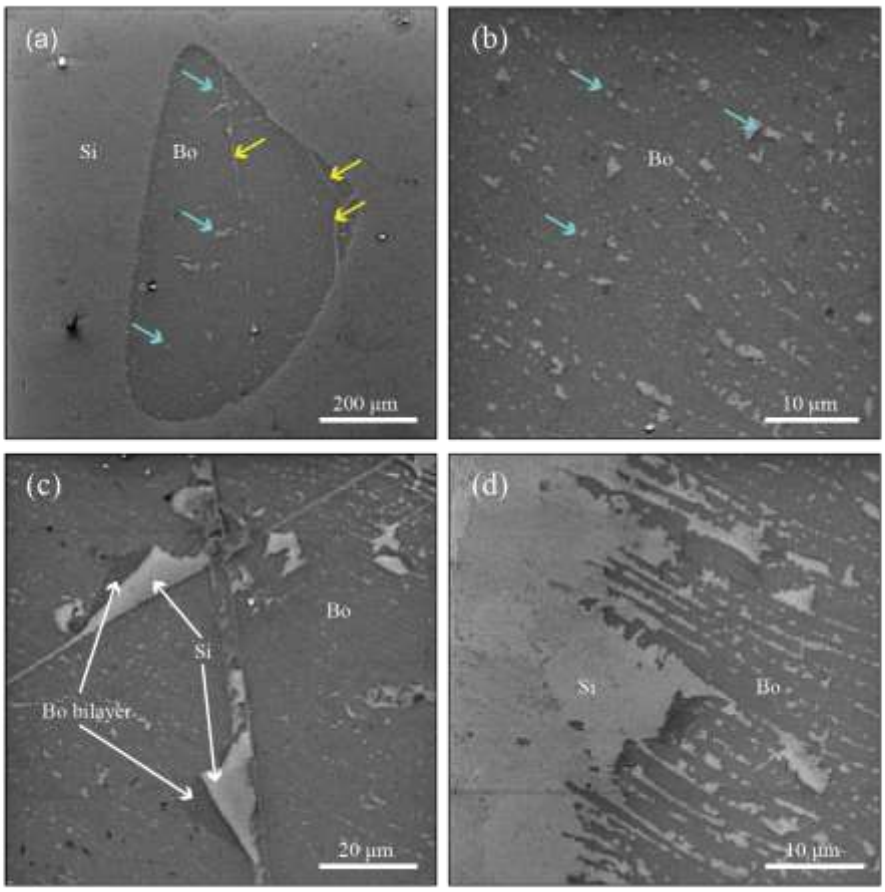

Figure 48. *SEM images of Bo after transfer to Si wafer. (a) Largest transferred Bo fragment. (b) Magnified view of the central region of transferred Bo. (c) Magnified view displaying self-overlapped segments of transferred Bo. (d) Magnified view of the edge of the transferred Bo. [Adopted from Ref.* [133]*].*

One of the largest transferred Bo flakes is shown in **Figure 48(a)**, where the entire flake appears homogeneous, apart from a few larger cracks and holes (see yellow and cyan arrows, respectively). As a result of transfer volatility and Bo reactivity, in regions with bare Ir tearing of surrounding Bo can start, resulting in the Bo sheet's fragmentation. A zoom-in into the central region of the flake is shown in **Figure 48(b)**, where additional smaller holes can be resolved. These holes appear to be distributed along a series of almost parallel lines that are several micrometers apart. The arrangement of these curvy lines and their direction is strikingly reminiscent of the distribution of Ir step-bunches prior to Bo transfer, as shown in **Figure 46**.[36] Thus, most obvious seems that holes in the transferred Bo dominantly appear on locations where Bo/Ir exhibited structural imperfections and possibly different binding - in this case, related to Ir step bunches formed during growth. It is plausible that Bo located at the Ir step bunches is strained and chemically more reactive, and therefore more easily damaged during

electrochemical treatment and mechanical manipulation. In other words, most of the defects in transferred Bo stem from inhomogeneity of the synthesis substrate, rather than from the transfer procedure itself. Similarly, substrate step-edges were found to imprint onto Gr transferred from Cu foils.[164] Several folds have been identified where the Bo layer overlapped onto itself and locally formed a bilayer, as clearly distinguishable in **Figure 48(c)**. At the edge of the transferred Bo flake, the number of holes and cracks in the layer increases, as visible in **Figure 48(d).** This can be expected, since etching and/or tearing of the Bo layer took place there, as described in more detail on AFM measurements below.

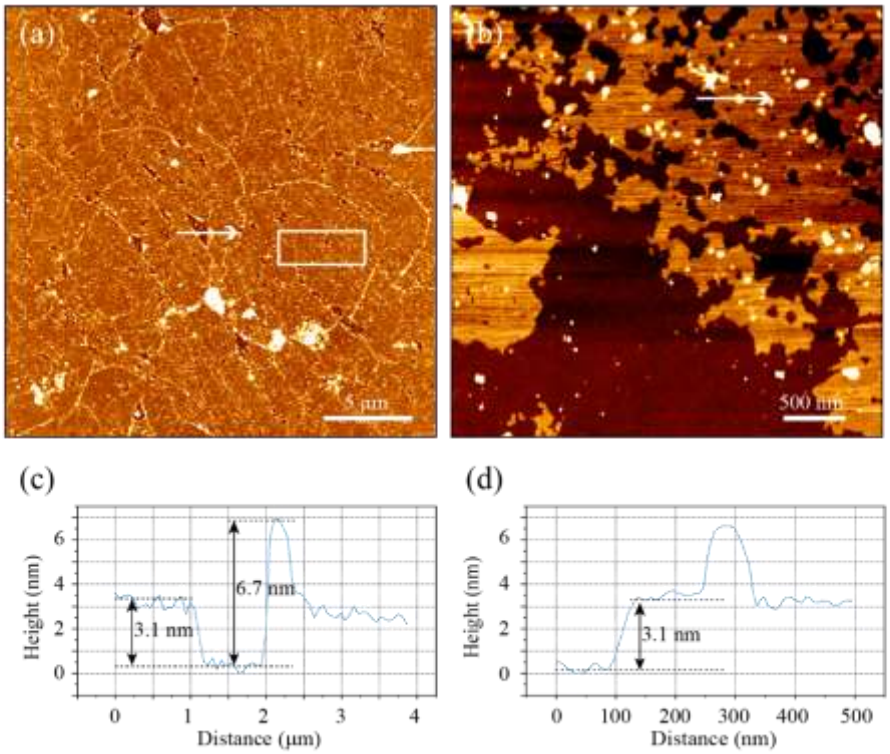

Figure 49. *AFM imaging of Bo after the transfer to an oxide-covered Si wafer. (a) Topography of the central region of the largest transferred Bo flake, where a white rectangle indicates the area inspected for roughness analysis. (b) Topography of the edge of the largest transferred Bo flake. (c) and (d) Line profiles extracted from panels (a) and (b) (as marked by arrows), respectively, with heights of the transferred monolayer and bilayer Bo indicated. [Adopted from Ref.* [133]*].*

AFM image in **Figure 49(a)** provides an even better resolution of the transferred Bo layer than the SEM. Overall, the sample is flat and free of large-scale defects and thickness inhomogeneities, which indicates that our transfer method did not leave any notable mesoscopic PMMA contamination on the Bo layer. In addition to the holes visible with SEM, quasi-1D defect lines are observed, again mirroring previously discussed Ir step-bunch regions. No

conclusive evidence is found of transfer-induced wrinkling of Bo. However, several folds have been identified where the Bo layer overlapped onto itself and locally formed a bilayer, as confirmed from the corresponding profile shown in **Figure 49(c)**. Such folds are also clearly distinguishable in the SEM image in **Figure 46(e)**. At the edge of the transferred Bo flake, the number of holes and cracks in the layer increases, as visible in **Figure 46(f)** and **Figure 49(b)**. This can be expected, since etching and/or tearing of the Bo layer took place there, as described previously. The same processes most likely resulted in the accumulation of excess material in the form of bright protrusions visible in AFM topography, extending up to 10 nm in height. **Figure 49(b)** and the corresponding line profile in **Figure 49(d)** allow determination of the height of the transferred Bo, which is 3.1 nm. This measured Bo height is more than an order of magnitude larger than the height of Bo on Ir(111).

Besides already discussed variations in AFM height measurements,[177] a dominant factors which could contribute to such an apparently large Bo height increase after the transfer are different substrate and the adsorption of various chemical species the sample surface, both during and after the transfer. During the transfer, adsorption of atoms and molecules from different solutions to the basal plane of Bo is plausible. In particular, water molecules originating either from exposure to air or from the transfer procedure can form thin layer of different thickness depending on surface affinity for water adsorption (hydrophilic or hydrophobic). Such water layer can significantly influence the measured height of Bo on Ir and on oxide-covered Si, as has been demonstrated for Gr on SiO_2.[179]

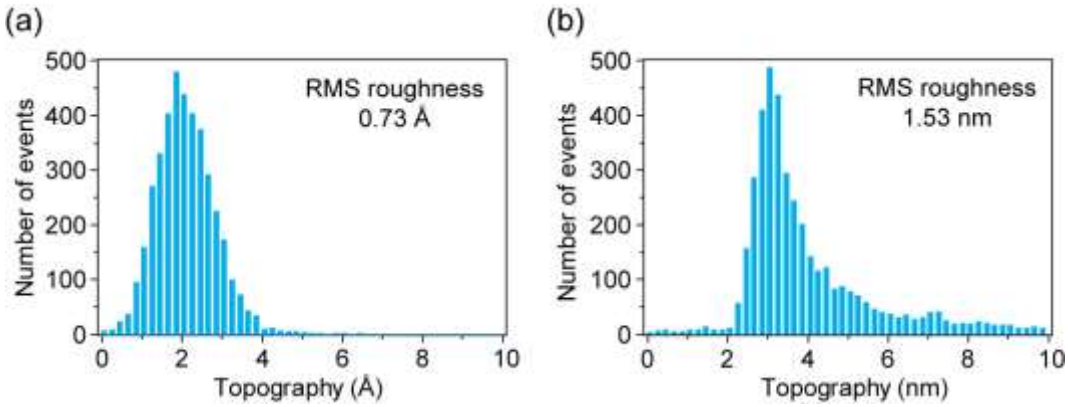

Figure 50. *Histograms of height distribution of (a) Bo/Ir and (b) Bo/Si, extracted from areas indicated by white rectangles in* ***Figure 47(a)*** *and* ***Figure 49(a)****, respectively. RMS roughness values are indicated for both cases. Note different units on the x-axes. [Adopted from Ref.* [133]*].*

Surface roughness (here quantified as root mean square value, RMS roughness) of pre- and post-transfer Bo have been calculated from AFM images, and respective height distribution

histograms are shown in **Figure 50.** RMS roughness of Bo/Ir is 0.73 Å and 15.3 Å of Bo/Si. Roughness of Bo/Ir obtained in our measurement is comparable to roughness of Bo on Cu(111) of 0.43 Å,[178] and signifies a smooth surface of an epitaxially grown 2DM. An increase by a factor of ~20 after the Bo transfer is due to the presence of cracks and fragments in the transferred Bo, as well as the nanoscopic remnants of different chemicals and solvents used in the transfer procedure.

4.1.3. Raman spectroscopy of Bo

For final confirmation of Bo ambient stability and transfer success, Raman spectroscopy has been done, and results were compared to DFT calculated spectra of a freestanding borophene.[133] Raman measurements of Bo sheets can be found in the literature,[48,180,181] but the technique is still not firmly established as a standard Bo characterisation tool, as in the case of, e.g., Gr. Ideally, Raman spectroscopy could also be used for the identification of different Bo polymorphs. In line with this, we used DFT to calculate vibrational modes and Raman spectra of a freestanding Bo layer (Bo_{free}) and we also experimentally measured Raman spectra of Bo/Ir and Bo/Si. The respective data is presented in **Figure 51**. A large number of Raman peaks can be discerned in all spectra, in accordance with the large unit cell of the Bo χ_6 polymorph which contains 25 B atoms.[135] Many peaks of the Bo/Ir spectra show a good overlap with the peaks of the Bo/Si spectra [**Figure 51(b)** and **(c)**, see vertical green stripes]. This signifies that the transfer of Bo layer has been successful, preserving the original crystal structure of Bo in the transfer process. Importantly, no PMMA signal has been detected in the Bo/Si spectra, indicating that PMMA residuals have been removed from the material.

Besides very good correspondence between the Raman spectra of pre- and post-transferred Bo, the majority of experimentally obtained peaks in **Figure 51(b)** and **(c)** have their counterparts in the calculated spectra of freestanding Bo sheet (Bo_{free}), shown in **Figure 51(a)**. The correspondence between Bo/Ir and Bo_{free} peaks signifies that Bo is weakly bound to the Ir surface. Indeed, observing distinct Raman peaks in the Bo/Ir system indicates that Bo-Ir interaction is weak in air-exposed samples, as it has been shown that the Raman spectra of 2DMs can be quenched if the binding to the metal substrate is strong.[62,182]

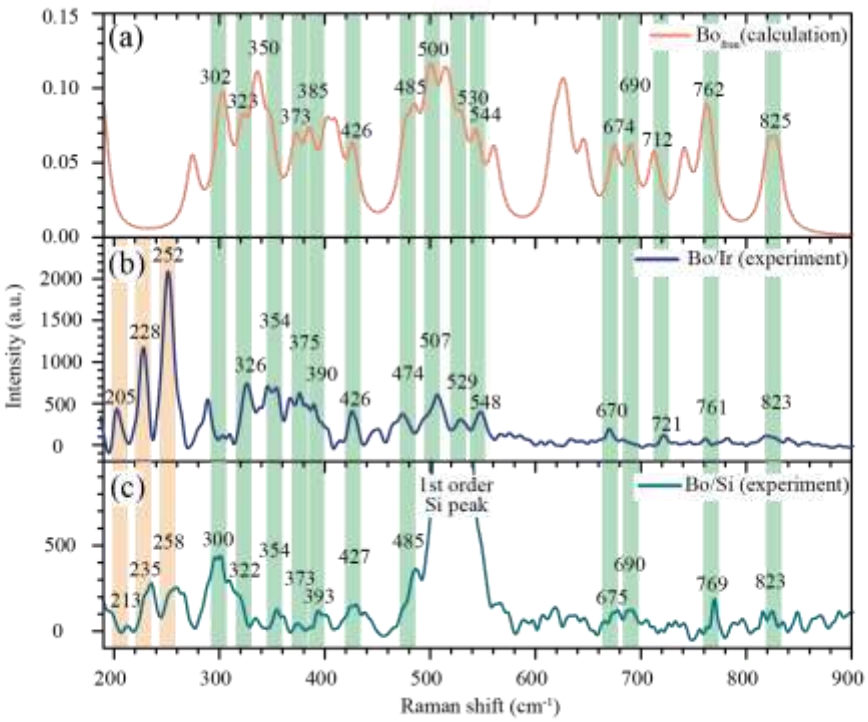

Figure 51. *Raman characterisation of Bo. (a) DFT-calculated Raman spectrum of a freestanding Bo layer (Bo$_{free}$). (b) Measured Raman spectra of Bo/Ir (after background subtraction) and (c) of Bo/Si. Vertical colored stripes are guides to the eye which indicate common Raman modes. Energies (in cm^{-1}) of indicated Raman modes are given as numerical values in each panel. [Adopted from Ref.* [133]*].*

Despite overall good agreement between our experiments and DFT calculations, some discrepancies can also be found. Experimental low-energy Raman modes (peaks marked by orange vertical stripes in) are not reproduced well in DFT calculations of Bo$_{free}$, which has also been seen for the χ_3 and β_{12} Bo polymorphs on Ag(111).[180] When bound to the substrate, new Raman modes may become activated in Bo due to different factors such as reduction of symmetry[92,183,184] or interaction with the substrate.[185] The energy of these so-called Raman interaction modes is substrate-dependent,[185–188] which is in line with the shifts of low-energy peaks in Bo/Ir and Bo/Si. The energy positions of other Raman modes are expected to be substrate-dependent to some extent. An obvious example of this is the B_g mode at ~300 cm^{-1} shown schematically in **Figure 52(a)**, exhibiting out-of-plane motion of B atoms. Besides the 300 cm^{-1} mode, **Figure 52** illustrates corresponding phonon modes of Bo which were identified in measured Raman spectra on both substrates.

It should be noted that on the high-energy part of the spectra, Raman peaks of Bo/Ir exhibit reduced intensity and lager widths. Atomic motions of the two representative modes, at

~760 cm^{-1} and ~820 cm^{-1} and both of Ag symmetry, are schematically shown in **Figure 52(e)** and **(f)** respectively, displaying clear in-plane motion of B atoms. The absence of pronounced Raman peaks associated with these modes can be explained by enhanced interaction between B-B stretching vibration modes with the boron σ electronic states when metal substrate is present.[189] Such signal attenuation can also lead to apparent merging of closely-spaced Raman peaks, as visible for the ~820 cm^{-1} modes in **Figure 51**.

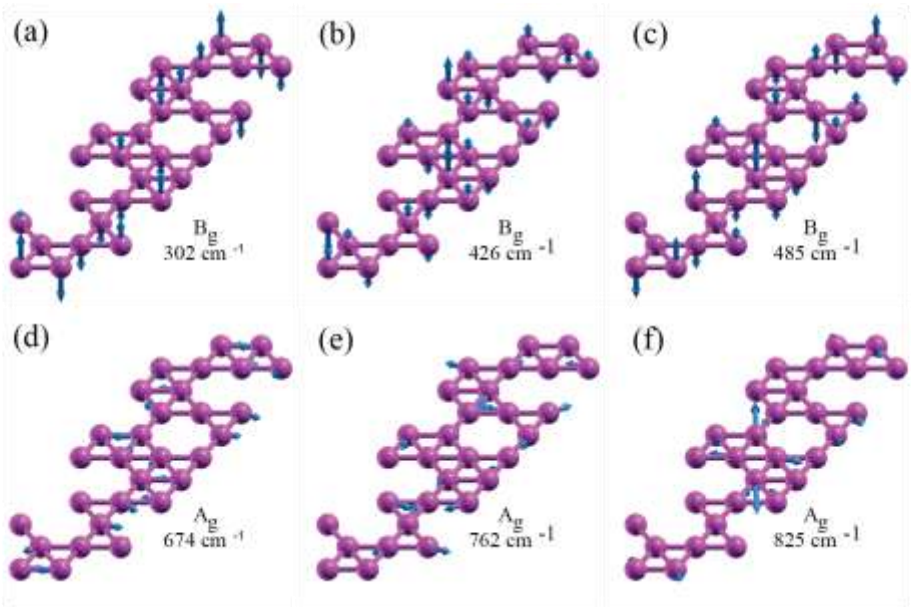

Figure 52. *Perspective view of six calculated Raman active modes for the freestanding Bo χ_6 polymorph. (a-c) B_g symmetry modes and (d-f) A_g symmetry modes with indicated energies for each mode. The blue arrows and their lengths denote the directions and relative amplitudes of atomic vibrations, respectively. [Adopted from Ref.* [133]*].*

Even though the same Raman peaks can be identified in Bo/Ir and Bo/Si spectra, they are found at slightly different energies (of the order of 10 cm^{-1}) and have different relative intensities. Energy shifts are expected due to the alterations in interaction and doping induced by the change of the substrate and the chemical environment (i.e., the presence of adsorbates originating from the transfer process). For example, Raman mode shifts have been identified for organic and oxygen adsorbates on Bo.[190,191] Also, strain release within Bo upon the transfer is a possible candidate for the observed energy shifts.[135,175,188] From the technical side, high laser power needed to detect Raman scattering increases the temperature of the sample, which also changes the Raman peak positions of atomically thin materials depending on the type of the substrate.[192] Peak intensity decrease can also be caused by strain release during the

transfer,[193] or by defects and compositional modifications of Bo during different steps of the transfer,[62,194,195] driven by chemical reactivity of Bo already discussed above. Overall, based on the AFM and Raman data, we conclude that the transferred material is an as-grown Bo layer, likely decorated with foreign species originating either from air exposure or contact with solvents during the transfer process.

4.2. Gr and MoS_2/Gr heterostructure

4.2.1. Gr

Early scientific reports on mechanical manipulation and device utilization of 2DMs were mainly based on Gr since it was the first discovered 2DM. For instance, Gr has been experimentally present for over a decade longer than Bo. Gr was used primarily in our work to test and calibrate our constructed setups (mostly electrochemical transfer and transport characterisation setups). For this purpose, in-house grown Gr on Ir(111) and purchased Gr on Cu foil were used. In addition, Gr on Ir(111) was also used as a growth substrate for MoS_2 islands. MoS_2/Gr heterostructure was investigated in a similar way as Bo, with optical and morphology characterisation techniques.

SEM was used to determine the success of synthesis or transfer by quickly inspecting characteristic features for Gr. In the case of growth on Ir, the presence of Gr can be identified from to the formation of the wrinkles, as shown in **Figure 53(a)**, which are standard signatures of Gr grown on single-crystals.[128] They are a sign of relaxation of compressive stress, which builds up during cooling due to Ir and Gr's different thermal expansion coefficients.[196] Electrochemical method, described in detail in subsection **3.1.2.**, was employed to transfer Gr monolayers from Ir single-crystal and Cu foil. During the transfer, additional wrinkles or other morphological modifications of the Gr sheet can occur, as discussed in the previous section for Bo transfer.[62,63,195] For device utilization, the quality of the Gr must not be degraded during this transfer process.[197] In our work, SEM is used to determine the presence of contaminations, folds, cracks, or holes in transferred Gr. An example of a transferred Gr sheet from Cu foil to Si wafer is shown in **Figure 53(b)**.

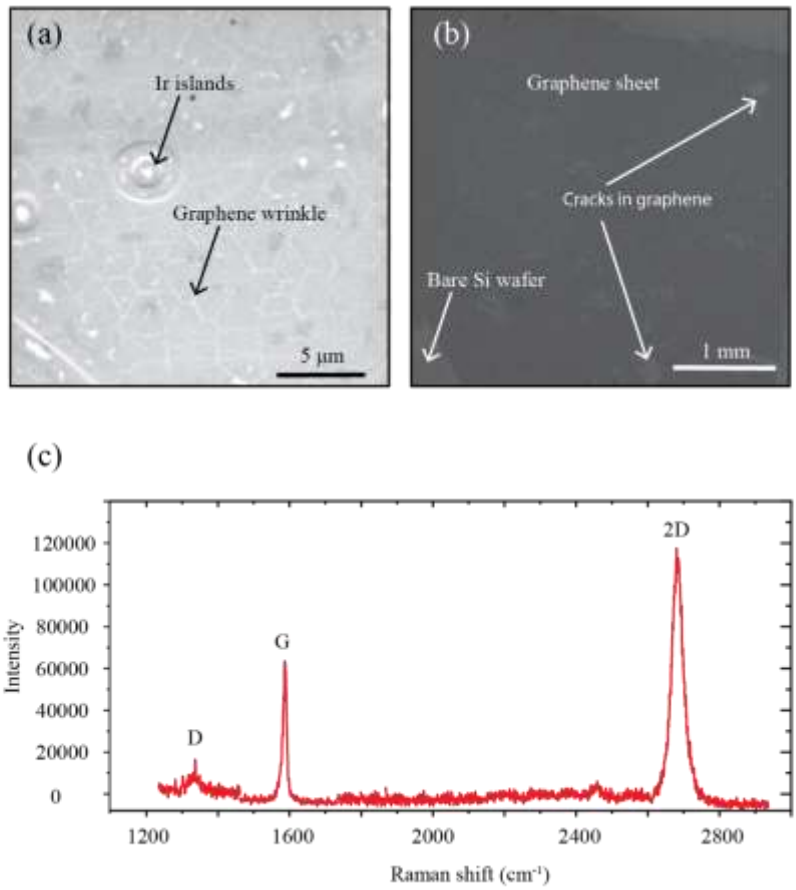

Figure 53. *SEM and Raman of Gr monolayer. (a) SEM image of Gr on top of Ir substrate, (b) SEM image of Gr sheet transferred from Cu foil to Si wafer. (c) Raman spectra of Gr transferred from Cu foil on Si wafer.*

In our work, Raman spectroscopy was used for Gr monolayer and heterostructures to identify the existence of Gr subsequent to transfer. The optical characterisation of Gr is based on inspection of the Gr's two characteristic Raman peaks, G and 2D. By observing their change, i.e., peak position and ratio of their intensities, one can conclude possible degradation caused by the transfer process or some other manipulation. Generally, the third characteristic D peak, is closely related to the defect amount in the material.[198]

Samples used for transport characterisation of Gr were fabricated by electrochemical transfer of Gr from Cu foil onto Si wafer with patterned Au electrodes. Samples were analyzed by Raman spectroscopy to determine the quality of the material due to the fact that those samples were obtained from commercially available suppliers. **Figure 53(c)** shows the characteristic Raman spectrum of the transferred large-scale Gr sheet, with indicated 2D, G, and D peaks. The main morphological reasons for D peak existence were cracks induced during the transfer, shown in **Figure 53(b)**. For the ideal case with minimum defects, the G/2D

intensity ratio should be around 30%, while for the samples we used the ratio was closer to 40%.[199] It is important to note that Gr on Cu foil was purchased on cm-size foils and protected by PMMA. The sample was cut into smaller pieces in the following months, and although Gr was coated with PMMA to prevent degradation in time, certain spectra modifications are probably caused by a long period between the synthesis and utilization.[198] The existence of the D and the ratio of G/2D peaks indicate that the sample underwent certain degradation. Most likely structural modification or chemical contamination of the pristine Gr was caused by long ambient exposure, transfer, or PMMA removal; however, their amount was low enough to utilize Gr for FETs.

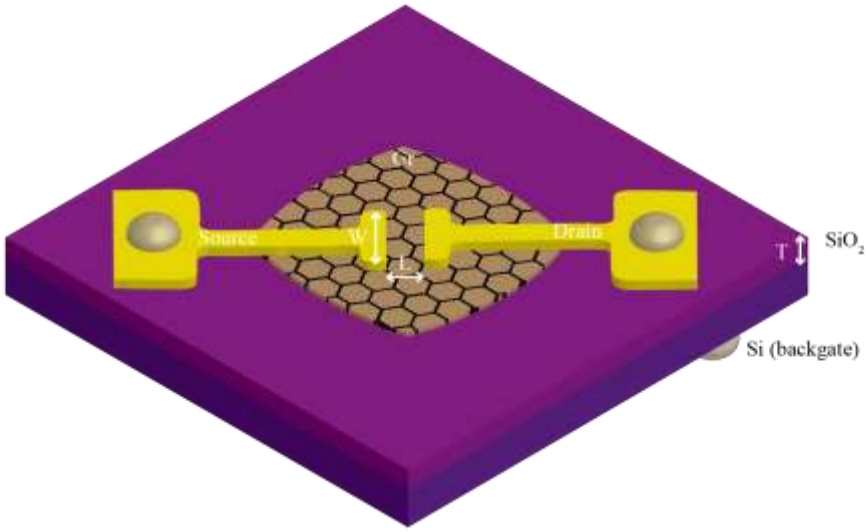

Figure 54. *Schematic of Gr FET configuration.*

After optimization of its transfer, Gr sheets on Si wafers were used for FET fabrication, as shown in **Figure 54**. Gr monolayer sheet was transferred from Cu foil, as depicted in **Figure 53(b)**, while electrodes were fabricated with e-beam lithography. Gr FET channel length and width were 100 μm and 10 μm, while the used substrate was a Si wafer with an oxide layer of 85 nm thickness. Transfer characteristic I_{DS}-V_{BG} is shown in **Figure 55(a)**, where the ambipolar nature of the device is visible. Higher voltages were not used because dielectric breakdown often occurred on them. Output curves at several constant gate voltages while changing source-drain voltage are shown in **Figure 55(b),** with evident p-type behavior as current I_{DS} decreases with an increasing positive V_G. Gr transistors are often p-doped due to adsorbates such as oxygen and water molecules on the Gr surface or as a result of device fabrication and transfer, which cause a large Dirac point shift towards the positive direction.[200] Calculated carrier mobilities were around several hundreds of $cmV^{-1}s^{-1}$, an order of magnitude lower than usual

and three orders of magnitude lower than best reported Gr mobilities.[16,201] Lower values could be due to degradation previously discussed in Raman measurements, but also due to contact resistance with Au/Cr electrodes or backgate configuration.[5]

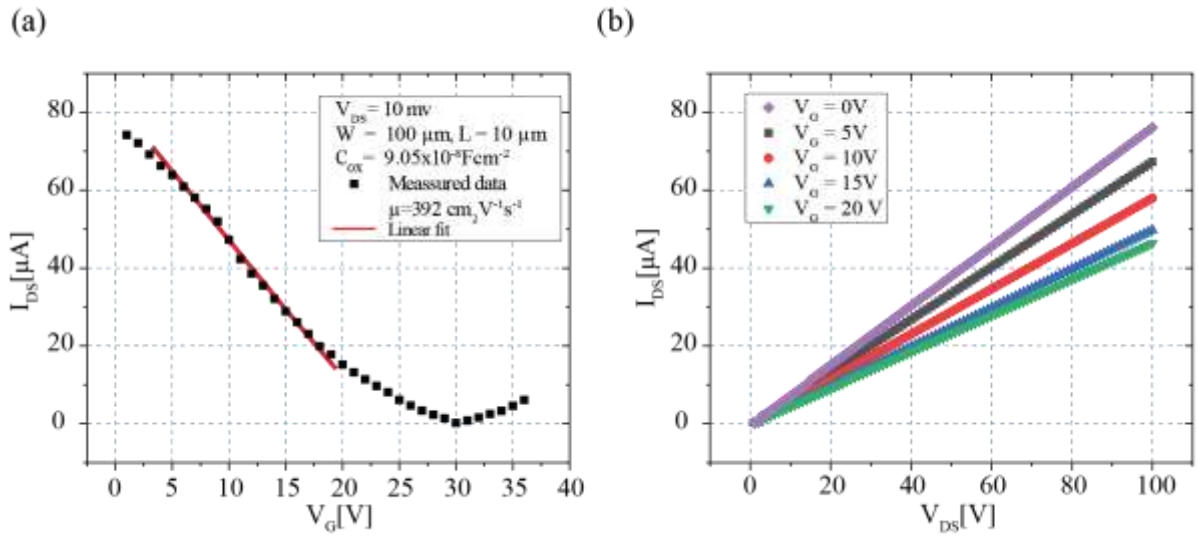

Figure 55. *Characteristic Gr FET I-V sweeps. (a) Gr FET transfer characteristics with constant V_{DS} and varying V_G. (b) Gr FET transfer characteristics with constant V_G and varying V_{DS}, under different gate voltages.*

4.2.2. MoS_2/Gr heterostructure

Gr grown on Ir(111) was used as a substrate for synthesizing MoS_2/Gr heterostructure as described in section **2.1.** Similarly, like with Bo and Gr only, electrochemical transfer was exploited to move the heterostructure from Ir to Si wafer. Even though the electrochemical transfer was employed for Gr, in the case of a heterostructure with small MoS_2, it was not known whether the MoS_2 islands will be removed in the transfer and could they survive without the loss of quality. Therefore, we have employed the same characterisation techniques before and after the transfer, from which AFM measurements provide the most useful morphological inspection, as MoS_2 islands were nm-sized.[138]

Figure 56(a) shows an overview of the heterostructure sample, with 22% coverage of MoS_2, which is determined by AFM analysis. Gr wrinkles are marked with a blue arrow and residual Mo clusters with green arrows. MoS_2 islands are nm-sized with dendritic contours that formed upon merging of the growing MoS_2 islands.[130,137] The height of MoS_2 islands is approximately 1 nm, as seen from the line profile in **Figure 56(d)**. Compared to in situ STM

measurements (disclosed in Ref. [138]), the thickness is enlarged mainly due to water adsorption, which is forming a thicker film on MoS_2 than on Gr as a result of the more significant water affinity.[177,202] To determine the Gr thickness, an area with a bare substrate is located, i.e., the etched part during synthesis was found, as illustrated in **Figure 56(b)**. The etching of the Gr happens due to a chemical reaction with the sulphur under increased pressure and temperature.[89] It is important to note that etching is not common and it generally occurs on larger Ir(111) terraces.[138] On the line profile shown in **Figure 56(e)** thickness of Gr flake is determined to be approximately 0.6 nm. It is important to note that 10%-20% thickness deviations were measured, depending on the tip and acquisition parameters used. **Figure 56(c)** shows a more detailed zoom-in of MoS_2 islands and a partially etched area of the Gr sheet. In **Figure 56(f)** size distribution of MoS_2, determined by threshold height in processing software, is fitted with

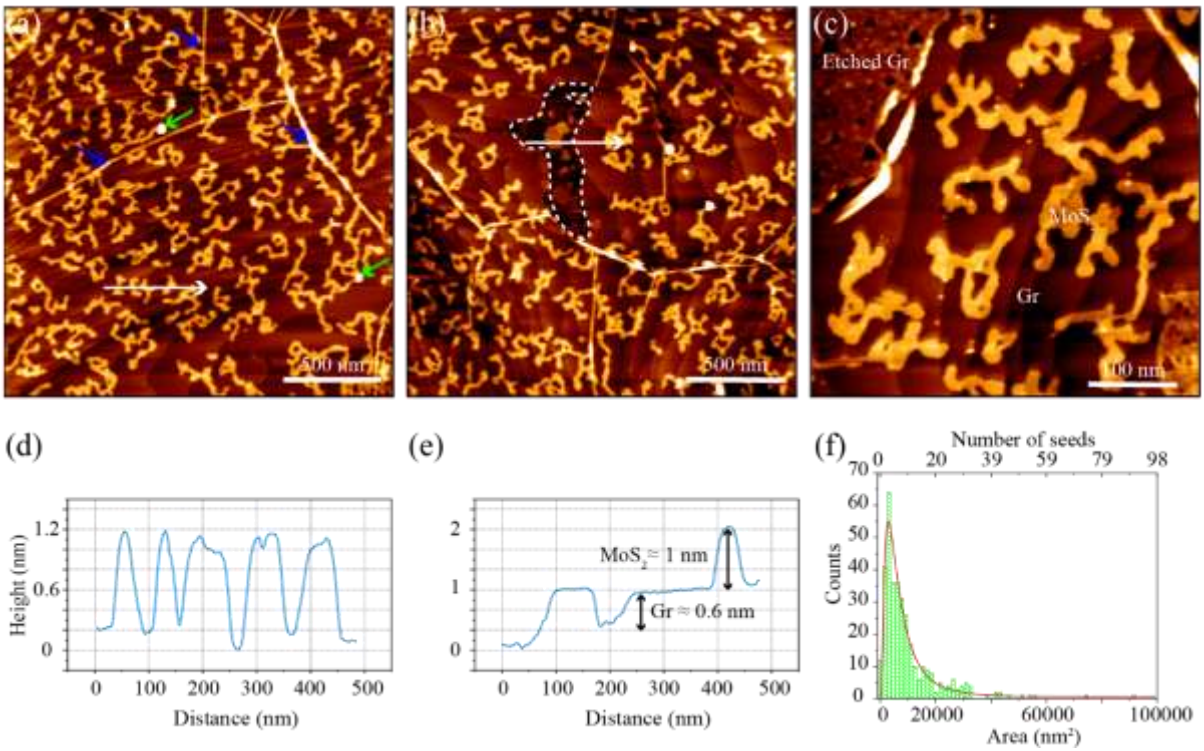

Figure 56. *MoS_2/Gr heterostructure on Ir(111), after extraction from UHV. (a) AFM image of the heterostructure, with clearly visible Gr wrinkles marked by the blue arrows and contaminations marked by the green arrows. b) AFM image with the etched Gr area, indicated by a dashed white contour. (c) AFM image of MoS_2 islands and etched Gr in upper left and bottom right corner. (d) and (e) Line profiles indicated with a white arrow on (a) and (b), respectively. (f) Distribution of MoS_2 island sizes (histogram) and fit to a log-normal distribution (red line). [Adopted from Ref. [138]].*

a log-normal distribution from where the average size of MoS_2 island is ~ 6000 nm^2, i.e., six seeds, where each seed (starting grain for MoS_2 monolayer growth) is estimated to 1000 nm^2 with *in-situ* STM.[138,203]

Heterostructure was transferred on a Si wafer by the electrochemical delamination method, described in subsection **3.1.2**.. AFM measurements were performed to determine the state of the MoS_2 islands after the transfer. In **Figure 57(a)** topography overview of the transferred sample is shown. Few defects are induced by transfer, primarily holes (marked by cyan arrows) and PMMA contaminations (marked by green arrows). The largest holes are most likely induced in the place of the etched Gr and uncovered Ir surface, where surrounding Gr was additionally scraped during electrochemical processes. At the same time, contaminations are circular in shape with different sizes up to a few hundred nm, a characteristic form of residual PMMA.[65,195] Thickness of the Gr sheet was determined to be approximately 1.5 nm from the line profile depicted in **Figure 57(c)**. A line profile was taken over one of the larger holes in Gr to ensure that the AFM tip was indeed measuring the bare Si wafer. With systematic analysis in multiple areas, we have confirmed that over 95% of the Gr sheet has been transferred. The thickness of MoS_2 islands was approximately the same as before transfer, as shown in the line profile in **Figure 57(d)**. An increase in the measured thickness of Gr after the transfer is expected because various solutions used in the transfer process can lead to unintentional intercalations and changes in water affinity between substrate and Gr sheet.[65] Additionally, (as shown in detail in Ref. [138]) optical characterisation was done to confirm the transfer's success, which shows a quality Gr Raman and MoS_2 PL signal after transfer to the Si wafer.

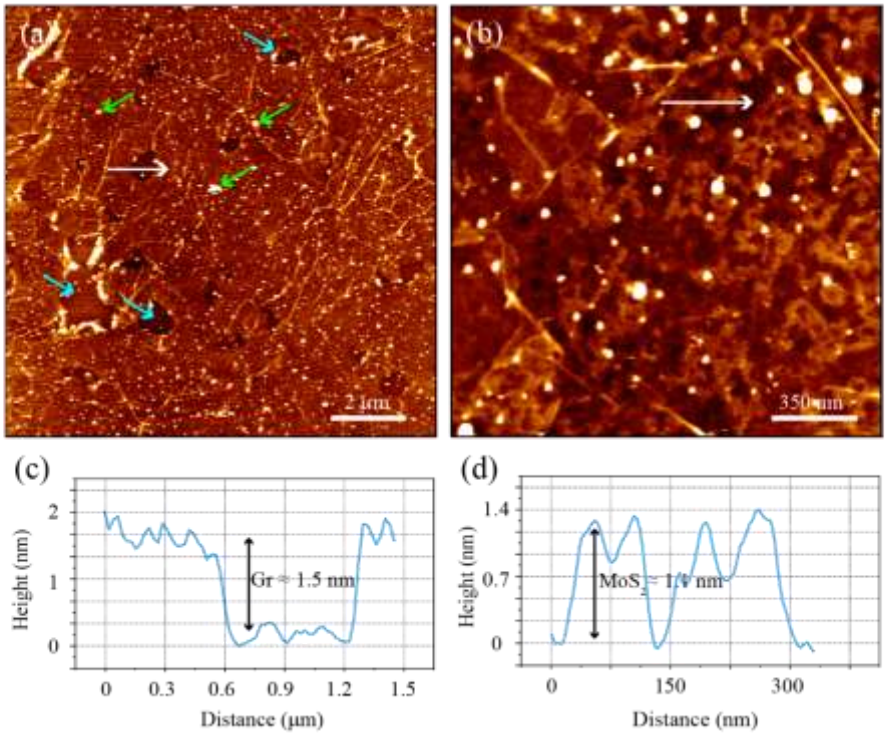

Figure 57. *Transferred MoS_2/Gr heterostructure. (a) AFM image of topography overview of the transferred heterostructure, with contaminations marked with green arrows and holes in Gr with cyan arrows. (b) Zoom in AFM image of transferred heterostructures with islands of MoS_2 distinguishable in topography. (c) Line profile showing thickness of Gr layer, indicated with white arrow on (a), (d) Line profile showing thickness of MoS_2 islands after transfer of heterostructure, indicated with a white arrow in (b). [Adopted from Ref.* [138]*].*

4.3. MoS_2

4.3.1. MoS_2 morphology

CVD-grown MoS_2 monolayers, as isolated flakes or full-coverage sheets, were characterised with surface characterisations prior to optic or transport measurements or their utilization for any devices. Their size and quality varied from batch to batch of the synthesis, and by employing SEM, one can rapidly inspect the whole sample surface. Large-scale overview images were used to pinpoint areas of the surface with flakes suitable for further processing. An example of an overview image of a surface with different flake sizes and shapes is shown in **Figures 58(a)** and **(b)**. A closer inspection can quickly determine in which areas flakes started to coalesce, as shown in **Figure 58(c),** or in areas in which the flakes have uniform

morphology, as shown in **Figure 58(d)**. Flakes or sheets with variable properties can be obtained depending on the variations of growth procedures, precursor delivery and quantity.[122]

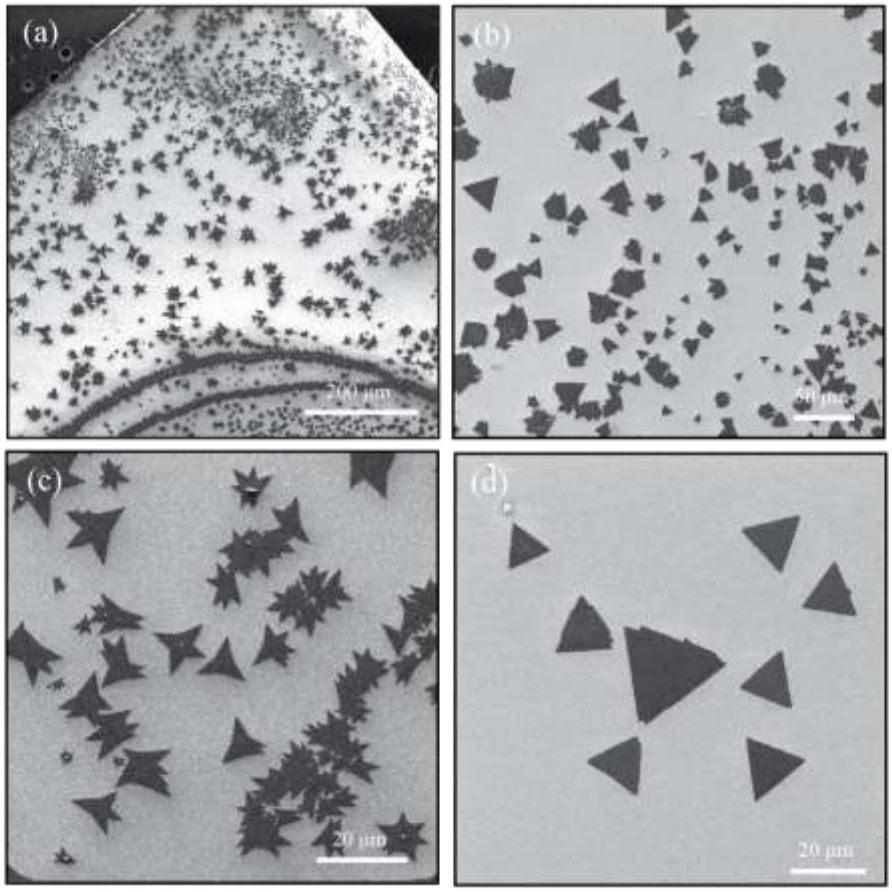

Figure 58. *Overview SEM images of MoS_2. (a) Large scale inspection of Si wafer with CVD grown flakes of MoS_2, (b) Closer look of the area with various shapes and sizes of the flakes, (c) Area with flakes starting to coalesce into a sheet, (d) Isolated triangular shape flakes of MoS_2.*

The most observed defects in MoS_2 samples are cracks, multilayers and surface decorations. Cracks are shown in **Figure 59(a)** and **Figure 59(b)**, while zoom-in on one of the cracks is shown in **Figure 59(c)**. Cracks are primarily induced at the cool-down of the sample after synthesis due to different thermal expansion coefficients for SiO_2 and MoS_2.[124] In addition, as seen in **Figure 59(d)** and **Figure 59(e)**, samples can often have different edge types or multilayers that usually start to form the center. Decreasing the sulphur evaporation rate and hence its partial vapor pressure during growth changes the geometry from dendritic to concave. For monolayer MoS_2, its final shape will be related to the growing rate of different edge terminations. The most commonly observed edge structures are Mo zigzag (Mo-zz) terminations and S zigzag (S-zz) terminations, which occur in excess of one of the elements

during synthesis.[204] Additionally, samples often have decorations on the edges as shown in **Figure 59(f)** and on the areas in which two flakes merged as shown in **Figure 59(g)**, where most likely oxygen or water adsorbed at the free atomic bonds on the edges or grain boundaries after ambient exposure.[205]

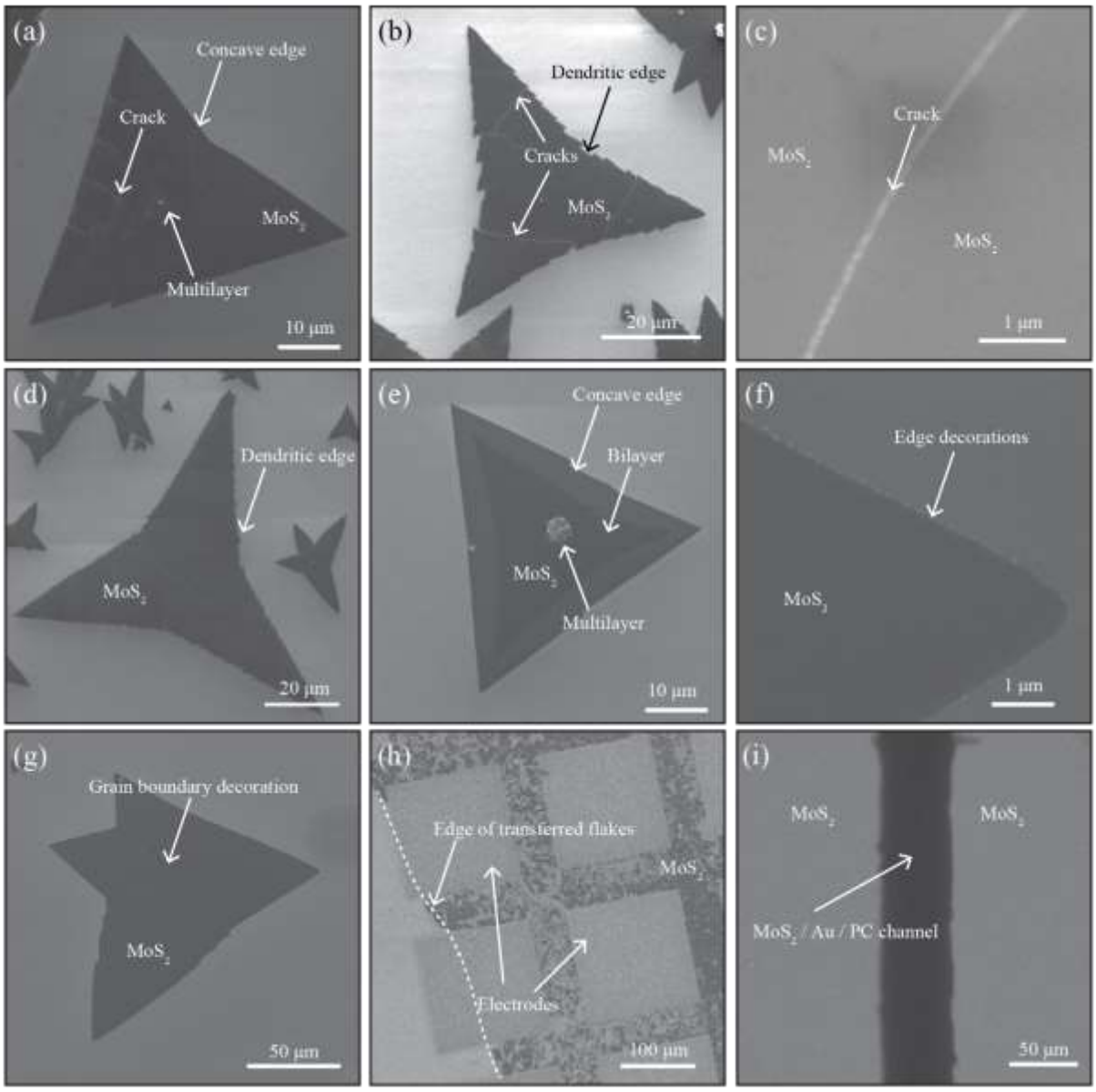

Figure 59. *SEM images of examples of various MoS_2 samples. (a) MoS_2 flake with cracks and multilayer at the center. (b) MoS_2 flake intersected with cracks. (c) Zoom in to one of the cracks. (d) MoS_2 flake with the dendritic edge. (e) MoS_2 flake with formed bilayer and multilayer formation at the center. (f) MoS_2 flake with edge decorations. (g) MoS_2 flake with surface decorations at grain boundaries. (h) Transferred MoS_2 flakes on top of Au electrodes at Si wafer. (i) Transferred MoS_2 sheet on top of Au electrodes on PC sheet.*

Generally, the best MoS_2 samples regarding defects number are flakes with sizes less than a micrometer, while larger flakes have various defects. Furthermore, larger flakes are often not grown from a single seed; instead, they are formed by merging neighboring smaller flakes, causing an increased chance for defects, as shown in **Figure 59(g)**. However, when larger flakes merge into a sheet, morphology enables new current paths in MoS_2 during transport measurements, which can avoid defects such as cracks. As a result, MoS_2 large monolayer sheets proved to be the best for device utilization (as will be demonstrated in subsection **4.3.3.**). **Figure 59(h)** shows an example of transferred monolayer flakes on a Si wafer on top of the electrodes fabricated by e-beam lithography. **Figure 59(i)** shows a sheet of MoS_2 monolayer on top of Au electrodes fabricated by stencil lithography on a PC sheet. Unfortunately, SEM does not provide insightful information on sample quality due to the charging effect on PC sheets.

A more detailed analysis of 2DM contaminations and degradation after ambient exposure or transfer is possible with AFM. **Figure 60(a)** shows the morphology of the MoS_2 flake on Si/SiO_2, where it can be seen that contaminations tend to adsorb on the flake's edge. AFM was also employed to investigate the intermediate step while MoS_2 was still on PDMS (after pick-up from the growth substrate but before the stamping step of the transfer), as shown in **Figure 60(b)**. MoS_2 can be more easily resolved from PC on phase-contrast images due to large substrate roughness, as shown in **Figure 60(c)**. Generally, it can be seen that stamping moves contaminations from the substrate and that it can result in the appearance of new cracks. As previously discussed, the polymer support layer can locally deform during transfer, which induces new cracks and enlargement of old ones.[66] After MoS_2 transfer from the synthesis substrate, those contaminations are transferred together with MoS_2 and new contaminations from PDMS used in the transfer, as shown in the AFM topography of the MoS_2 sheet at PC in **Figure 60(d)**. Typically, MoS_2 follows substrate morphology, which can be confirmed by similar RMS values of MoS_2 and substrate for each case (Si, PDMS and PC). The measured AFM thickness of MoS_2 can increase after the transfer, from approximately one nm (on Si wafer) to a couple of nanometers (if transferred on flat Si) or several tens of nanometers (if transferred on PC with Au electrodes). The main reasons for such an increase are stronger interaction with the growth substrate and formed water layer or other adsorbents at the interface of 2DM and transfer substrates.

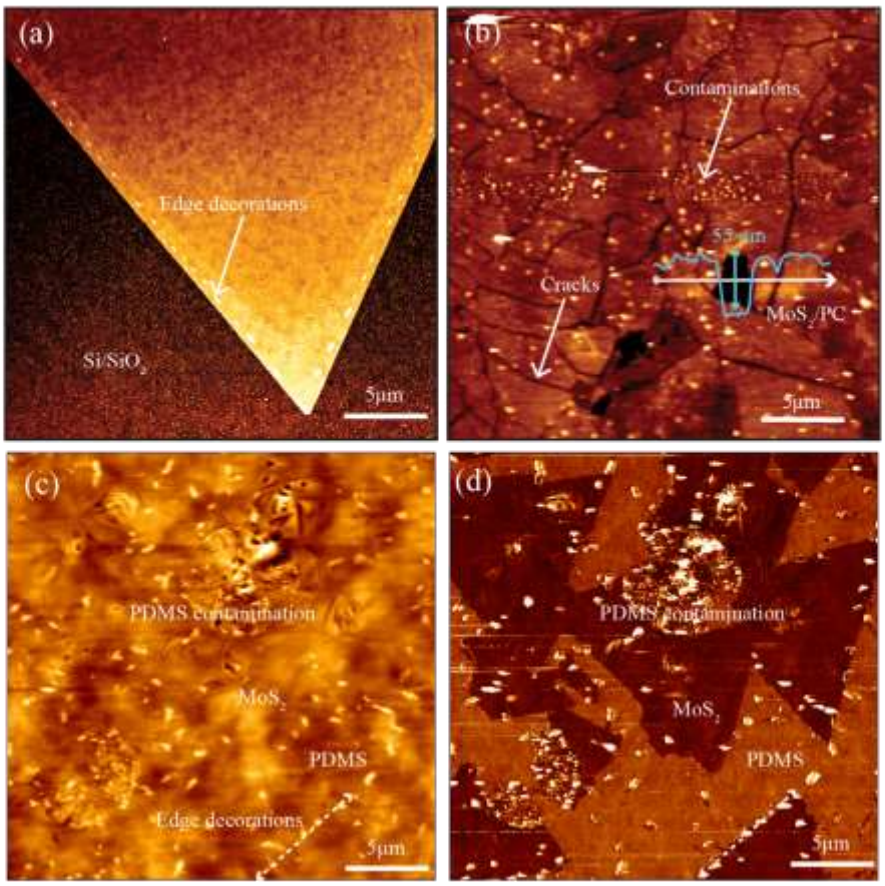

Figure 60. *AFM images of MoS_2 monolayer. (a) MoS_2 flake on Si/SiO_2 with visible contaminations from the exposure to ambient after synthesis. (b) AFM topograph of MoS_2 on PDMS, with a white dashed line indicating the contamination alignment with the flake edge. (c) AFM phase-contrast image of the same area depicted in (b). (d) Transferred MoS_2 sheet on PC with distinguishable cracks and contaminations.*

4.3.2. PL of MoS_2

As previously discussed, optical characterisation provides information on many different properties in 2DMs. In our work, we have focused on PL spectroscopy of samples as it is dominated by signatures of excitons, which are highly sensitive to material modifications. PL spectra of MoS_2 were fitted on three Lorentzians (A and B excitons and A^- trion), as shown in **Figure 61**. Some batches resulted in samples with pronounced kink on their right side of A exciton, designated to the trions. For good quality samples, A and B exciton peaks were located at 660 nm and 620 nm, respectively, while trion peak is on slightly higher wavelengths (lower energy in eV) than A exciton, in agreement with previous reports by Mak et.al..[24]

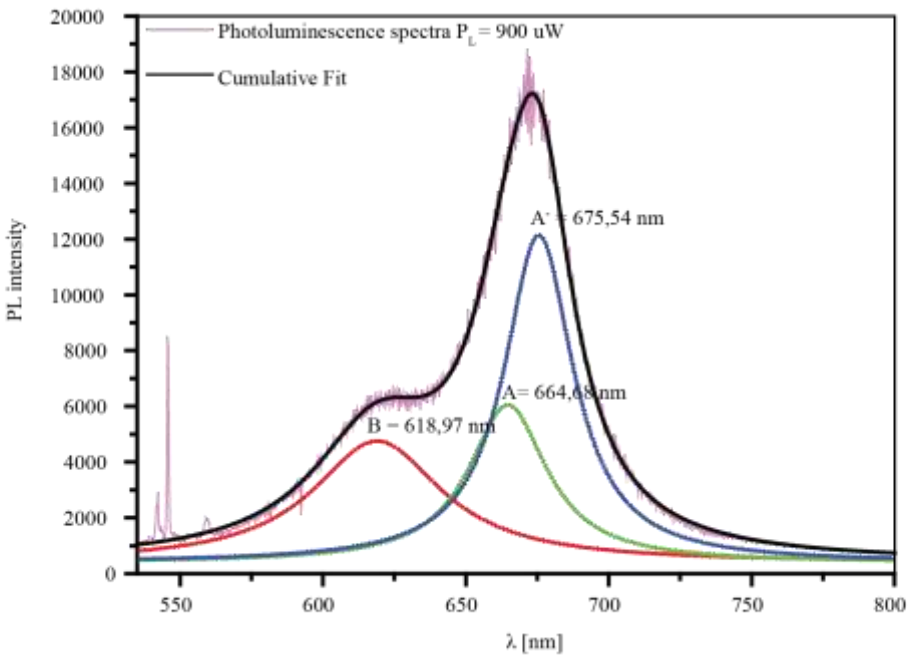

Figure 61. *PL spectra of CVD-grown MoS_2 monolayers, fitted with three Lorentzians (A and B exciton plus A^- trion peak).*

Standard methods for the enhancement of material properties in industry, such as ion implantation, are not exploitable with 2DMs. Instead, various other doping mechanisms are used, from chemical and charge transfer to molecular and strain doping.[206] In our work, we have inspected how photodoping and electric field doping influence on optical properties of MoS_2 monolayers. We have investigated the effect of photo-induced doping, achieved by varying laser power used for illuminating the sample. The dependence of the PL signal on laser power is shown in **Figure 62(a)**, where it can be seen that the PL intensity rises with an increase of photoexcitation. After initial fits that showed a mismatch between the cumulative fit of the measured data under different laser powers, more attention was dedicated to the broadening of A exciton in the red part. That broadening is due to the existence of trions whose energy is near A exciton. For more detailed analysis, measured spectra were normalized and fitted with three Lorentzians. Furthermore, when normalized spectra are analyzed, a notable redshift of A exciton is notable, as shown in **Figure 62(b)**. That shift is mainly due to the increase in the population of trions, evidently seen in **Figure 62(c)**. At lower laser powers, such as 1μW and 5 μW, the most dominant is an exciton peak, while by increasing the laser power exciton peak lowers, and the trion peak becomes dominant. One of the plausible reasons for trion increase under higher laser power is that the additional charges are optically created from defects in SiO_2 and are subsequently transferred to the MoS_2.[207]

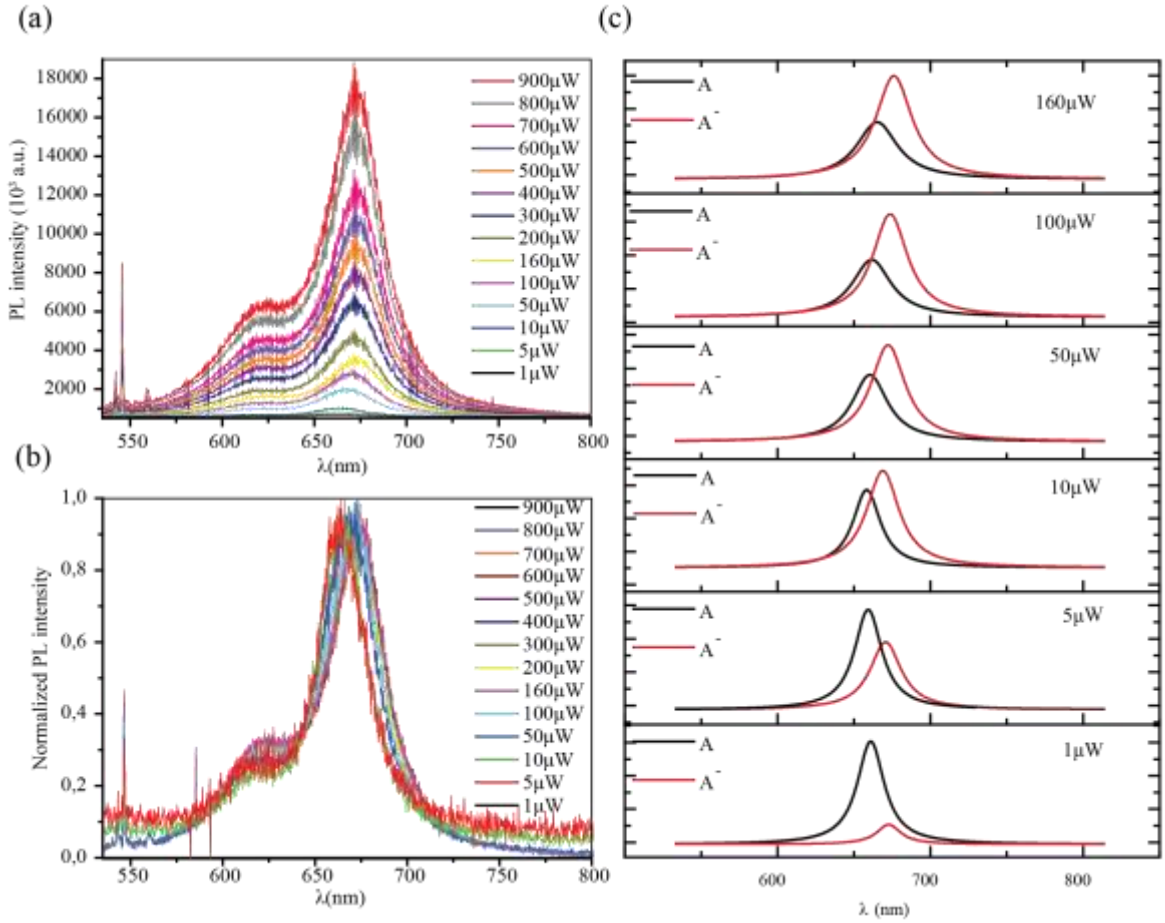

Figure 62. *PL spectra of MoS_2 monolayer for different laser powers. (a) PL dependence o laser power. (b) Normalized PL spectra. (c) Fitted A exciton and A^- trion peaks in dependence on laser power.*

Additionally, PL spectra were measured with no applied gate voltage and on symmetric values at a positive and negative voltage. SMU was used to apply voltage between one electrode (source or drain) fabricated on top of the MoS_2 monolayer, and Si substrate which is separated with SiO_2 layer from MoS_2, as schematically shown in **Figure 54**. PL spectra were measured under applied voltage difference and, like in the case of photodoping, intensity rises with the positive voltage increase and drops with negative electric fields applied, as depicted in **Figure 63(a)**. Furthermore, redshift on higher voltage is visible by checking normalized values of PL spectra, depicted in **Figure 63(b)**. However, the effect is not as pronounced as in photodoping because voltage only up to 8V was used, due to issues with the dielectric breakdown of the SiO_2 layer. Fitted data for A exciton and A^- trion is shown in **Figure 63(c)**. Interestingly, on the lowest voltages applied, trion population was highest, while on higher voltages, A exciton was dominant. To conclude the true nature of the trion/exciton ratio, a more detailed analysis that

would include higher voltages and temperature dependence would be needed.[151] However, our results show that with an electric field, trion population and optical response of MoS_2 can be controlled, as in agreement with previous reports.[24]

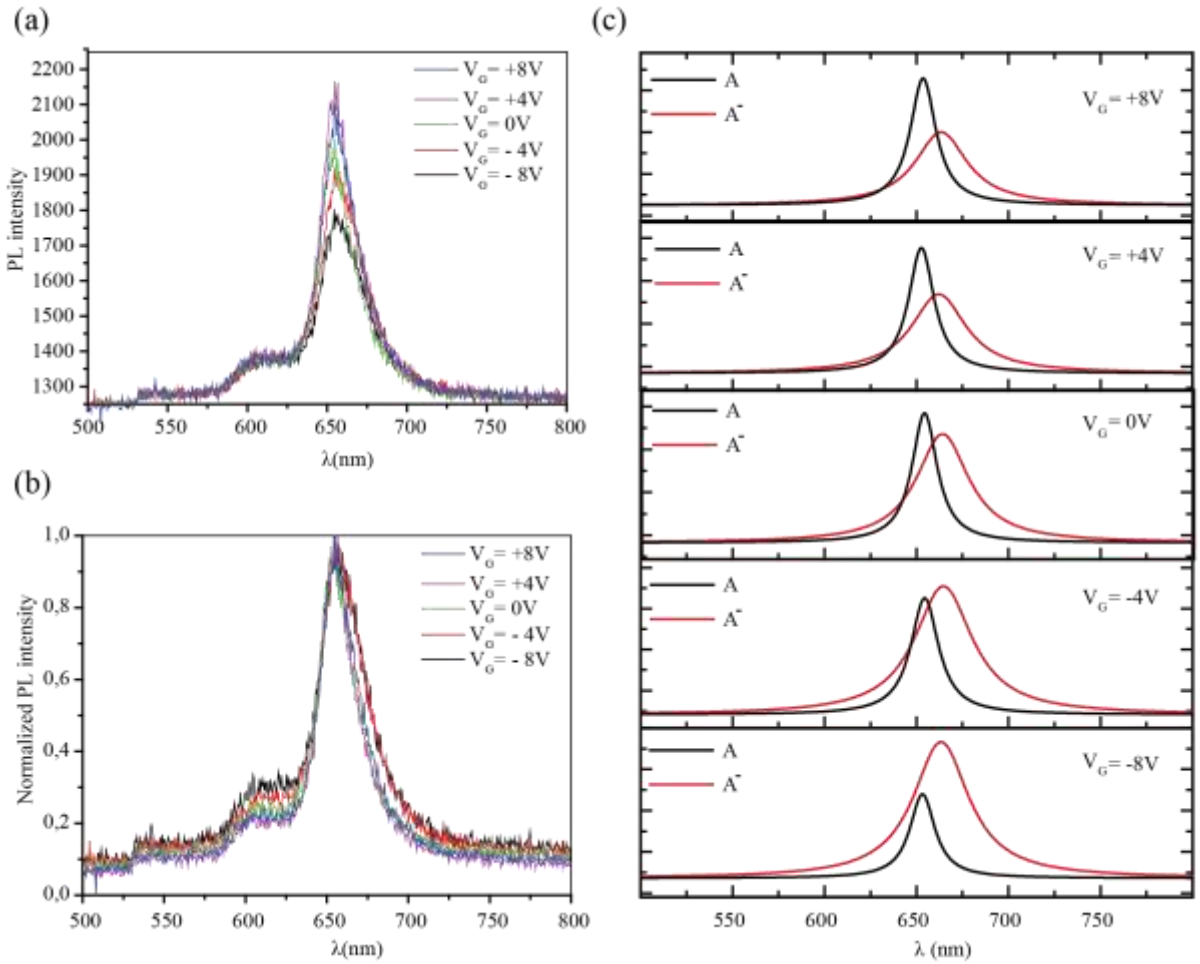

Figure 63. *PL spectra of MoS_2 monolayer for different gate voltages. (a) PL dependence on gate voltages applied. (b) Normalized PL spectra. (c) Fitted A exciton and A^- trion peaks in dependence on the gate voltage.*

4.3.3. MoS_2-based FET

FETs based on MoS_2 monolayers on Si wafer, were characterised in vacuum and ambient conditions by the setup described in subsection **2.5.3.**. The same backgate configuration as for Gr, described in subsection **4.2.1.** was employed. FET channels were fabricated with lengths from 10 µm to 100 µm and widths from 5 µm to 1500 µm. For mobility measurements, I-V sweeps were done, with constant drain-source voltage V_{DS} 10 mV or 100 mV and gate voltage sweeps up to 10 V or 100 V, depending on the Si wafer used and oxide thickness.

Characteristic MoS_2 transfer and output curves are depicted in **Figure 64(a)** and in **Figure 64(b)**, where I_{DS}-V_G and I_{DS}-V_{DS} are shown, respectively. Derived mobility is μ = 3cm $V^{-1}s^{-1}$ while the on-off ratio is 10^5. Those values are lower by two orders of magnitude than the best reports of MoS_2 FETs, mainly because those devices were fabricated with top-gate electrodes whose configuration and dielectric layer are superior to the back-gate devices in 2DMs.[29] It is important to note that devices did not always reach saturation point due to dielectric breakdown, which would occur on higher voltages necessary for most of the samples. After annealing samples at 100 °C in vacuum, samples‘ performence would improve somewhat, as depicted in **Figure 64(a)**, with the increased mobilities and on-off ratio up to five times. Such a process improves contact resistance, a known challenge for devices based on 2DMs.[208] Also, choosing different electrode metals with lower work function would result in lower contact resistance and Schottky barrier.[209]

Ambient transfer characteristics of FET were also analyzed, with measurements after one, two, and five days from the fabrication of the device, as depicted in **Figure 64(c)**. The mobility decreased by 25% and I_{DS} by 35% after a single day at ambient conditions, but degradation was slowed down and stabilized afterward. Such behaviour is most likely governed by the adsorbent water layer from the air.[209] Some devices had p and some n-type behavior, as seen in the oposite polarity needed for I_{DS} increase shown in **Figure 64(c)** and **(d)**, respectively. MoS_2 monolayers usually exhibit n-type channels.[210] However, there were also many reports on p-type FETs, mainly due to synthesis doping, subsequent substrate charge transfer, or metal electrode engineering.[208,209] First reason for the difference could be found in the variation of CVD growth and ambient conditions, which could lead to different adsorbents or intercalates in 2DM.[211] Additionally, inherent doping could be varied by different Si wafers used.[206] For instance, if Na impurities and O dangling bonds are introduced at the SiO_2 surface, these lead to localized states, which modulate the conductivity of the MoS_2 monolayer from n to p-type.[212] Si wafers were bought from several suppliers with variations in the type of dielectric growth, Si layer doping, and thickness of the oxide layer because of the dielectric breakdown of the SiO_2 layer, which is often reported for 2DM devices.[213] Based on discussed, uncontrolled doping during in-house synthesis and use of Si wafer form different suppliers were most likely causes for n/p type variations in our work.

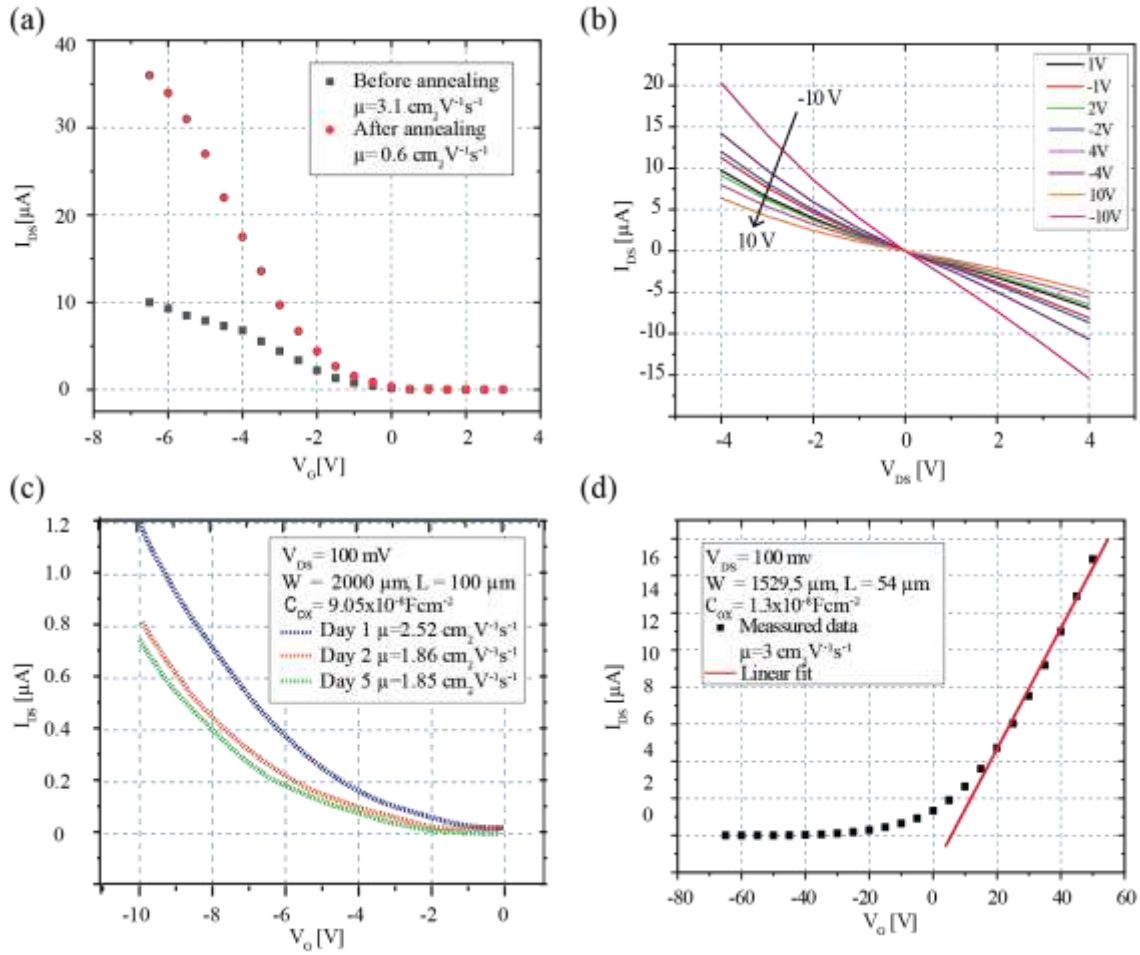

Figure 64. *Room-temperature transport characteristics of the MoS_2 FET device. (a) I_{DS}-V_G transfer characteristic for V_{DS} = 100 mV for the MoS_2 FET with 85nm oxide layer before and after annealing at 100°C. (b) Drain-source bias I_{DS}-V_{DS} output characteristic for different V_G. (c) I_{DS}-V_G transfer characteristic for V_{DS}=100mV for the MoS_2 FET with 85nm oxide layer, measured the first day and following days of ambient exposure after fabrication. (d) I_{DS}-V_G transfer characteristic for the MoS_2 FET with 300 nm oxide layer, with linear regression for mobility determination.*

For characterisation of MoS_2 monolayers, initial devices were fabricated from isolated flakes up to 100 µm win size, as shown in **Figure 59(a)** and **(d)**. Unfortunately, those devices had significant problems due to cracks, which are visible in **Figure 59(c)**, and dielectric breakdown. Additionally, with optical characterisations, there was a lack of spectra reproducibility, indicating that the growth method for small-scale samples is not usable for devices. In the end, full-coverage samples turned out to be a much better option in terms of device fabrication. Devices fabricated from them were functional with some inconsistencies in their doping and optical properties, as shown in the previous two sections.

Chapter 5

Strain-dependent device characterisation

This chapter focuses on the large-scale monolayers of CVD-grown MoS_2 (milimeter lateral size) characterised after the transfer to a suitable substrate for strain-dependent measurements. First, absorption spectroscopy of MoS_2 sandwiched between PDMS and PC was performed at different amounts of uniaxial tensile strain induced by 2-point bending of the substrate to determine how the strain transfer is affected by cracks and grain boundaries which are characteristic features of large-scale samples. Next, the monolayer MoS_2 was transferred on a PC sheet with Au electrodes to determine the suitability of MoS_2 for strain and tactile sensors. This has been done by inspecting the durability and reproducibility of changes in the resistance caused by uniaxial tensile strain induced by 3-point bending for more than 20 cycles lasting longer than 60 hours. Afterward, flexible strained MoS_2 photodetector has been characterized by investigating photocurrent spectroscopy with a 3-point bending stage. Finally, PL spectroscopy was performed to derive maps of local strain variations in monolayers transferred on top of Au electrodes with and without applied strain by 2-point bending.

5.1. Absorbance

To determine in which way the strain propagates through the large scale 2DM, we have investigated the absorbance spectra of CVD-grown MoS_2 sample under uniaxial tensile strain induced by bending. Large-scale CVD-grown MoS_2 samples grown on Si/SiO_2 wafer were used for this task. **Figure 65** shows a schematic illustration of the sample preparation. The first step consists of the pick-up step described in detail in subsection **3.1.1.**. Then, instead of stamping the 2DM on the second substrate, MoS_2 is placed on top of the PC sheet without removing the PDMS. In such a way, PDMS can promote adhesion of the MoS_2 monolayer to the substrate during the strain application.

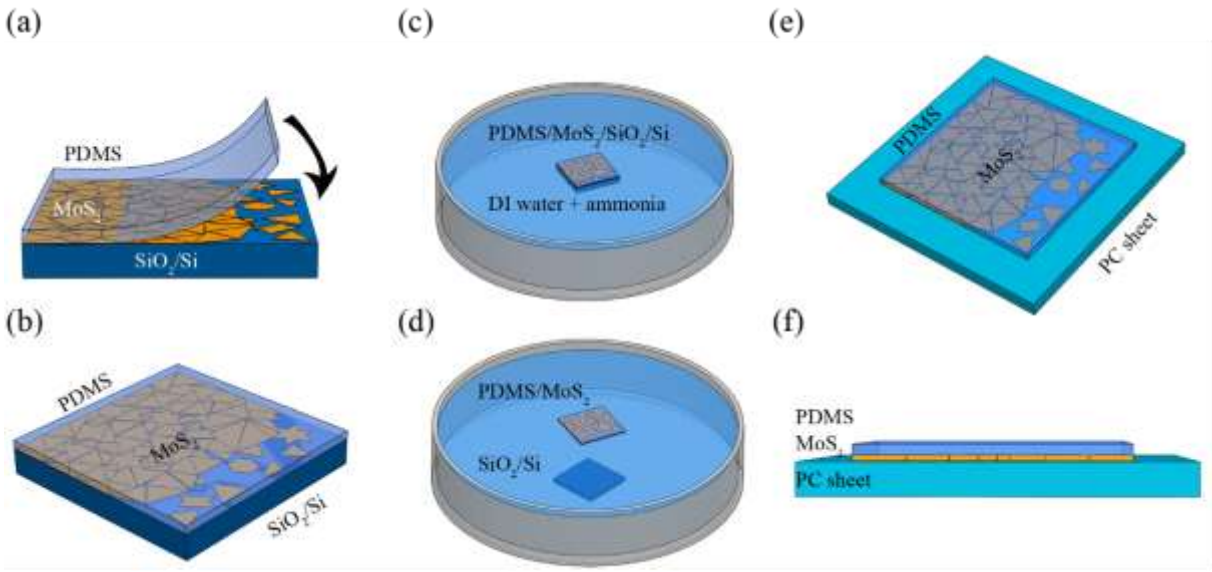

Figure 65. *Sample preparation for absorbance measurements. (a) PDMS film is placed over MoS_2 and Si/SiO_2 substrate. (b) PDMS sticks to the surface of the MoS_2 monolayer. (c) $PDMS/MoS_2/SiO_2/Si$ is placed on top of the DI water and ammonia. (d) The solution slowly intercalates between wafer and PDMS film after which substrate sinks in the solution and PDMS with MoS_2 stays floating on surface. (e) PDMS film is retracted from the solution and after that covered with a PC sheet in a way that MoS_2 flakes are placed in between PDMS and PC. (f) Side-view of the $PDMS/MoS_2/PC$ sample. [Adopted from Ref.* [139]*].*

After preparation, the $PDMS/MoS_2/PC$ sample is placed in a 2-point bending stage with access to the optical characterisation setup, as shown in **Figure 66(a)**. The spatially resolved absorption spectra were derived from positions indicated by a red line in **Figure 66(b)** that shows white light reflectance image of the sample surface on which the cracks of MoS_2 are visible. Absorption spectra were analysed at different steps, while gradually increasing strain up to a maximum value of 1.6 % and subsequent strain decrease. Additionally, angle-resolved SHG (second harmonic generation) measurements were performed (described in detail in Ref. [139]) to determine the exact position of the grain boundaries over the monolayer, as shown in **Figure 66(c)**. It can be seen from the derived map that spatially resolved spectra, indicated by a red line, were taken over multiple cracks and grain boundaries.

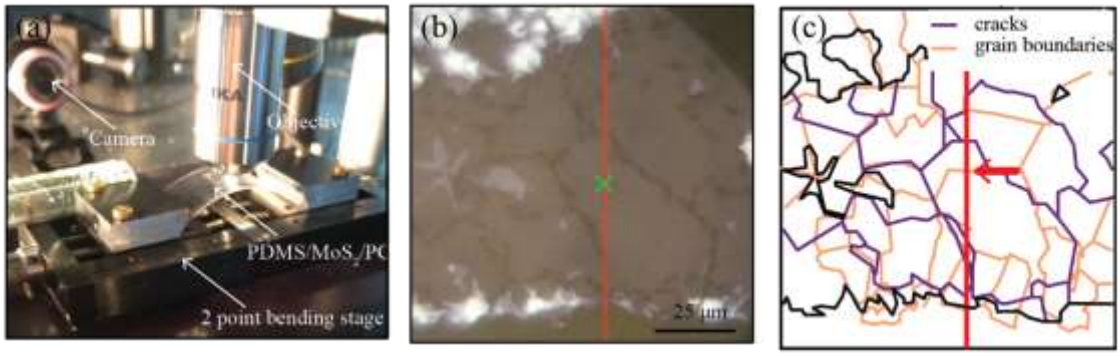

Figure 66. *Large scale PDMS/MoS_2/PC sample. (a) Sample strained with 2-point bending stage. (b) White-light reflection image of the sample. The red line indicates positions at which spatially resolved absorption spectra were taken, while the green cross indicates the position from which spectra shown in Figure 67(a) were acquired. (c) Map of cracks and grain boundaries of the same sample area, acquired by angle-resolved SHG. The black lines indicate the edge of the monolayer. [Adopted from Ref.* [139]*].*

The positions of A and B exciton peaks are determined from the absorption spectra at different strain values, as shown in the spectra depicted in **Figure 67(a)** that were acquired from the position indicated by the green cross in **Figure 66(b)**. With the application of strain, exciton positions are redshifted, as expected. By increasing the strain values, the redshift of the peaks gets more prominent, while after decreasing the strain values to 0 %, the excitons return to initial positions. From where it is evident that uniaxial tensile strain can be applied without permanently changing the MoS_2 properties. GFs for A and B exciton positions were derived from the measurements up to 1% of strain, at values GF_A = -42 meV and GF_B = -38 meV, as shown in **Figure 67(b)** and **(c)**, respectively. It can be seen that the values for strain up to 1.2 % are in agreement with the derived GF. In contrast, at higher values, the extracted excitonic positions deviate from the linear trend, which indicates that the monolayer sheet starts slipping for strain values above 1.2 %, and strain is not fully transferred to MoS_2 anymore.

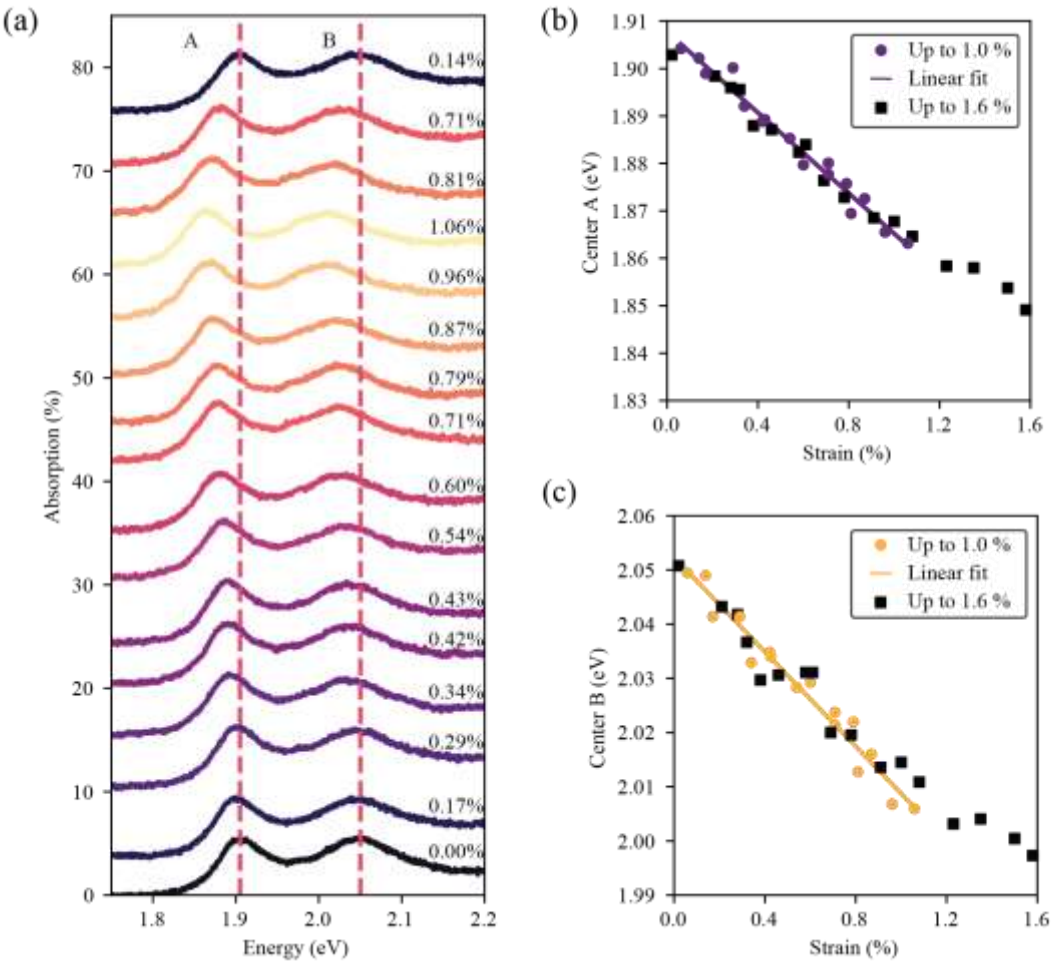

Figure 67. *Absorption spectra and determined GF values for A and B exciton of strained MoS_2. (a) Absorption spectra of the sample for increasing and decreasing levels of uniaxial tensile strain (color-coded) Position of the A and B exciton for 0% strain are indicated with red dashed lines to enhance the visibility of the redshift at each strain amount. Data was acquired from bottom to top. (b) Positions of A exciton at different amounts of strain with GF_A = -42 ± 2 meV extracted for measurements up to 1.0% of applied strain. (c) Positions of B exciton at different amounts of strain with GF_B = -38 ± 4 meV were extracted for measurements up to 1.0% of applied strain. [Adopted from Ref.* [139]*].*

Spatially resolved absorption spectra under different amounts of strain are shown in **Figure 68**. Absorption spectra were derived along a line that spans multiple cracks and grain boundaries, as shown in **Figure 66(c)**. The redshift decreases for exciton positions around the monolayer cracks, similarly as previously reported for the edges in exfoliated flakes.[91] However, there were no indications that grain boundaries reduce strain propagation in a way determined for the cracks. Subsequent to the first round of measurements performed for values up to 1.06 % of strain, the sample was strained and measured for values up to 1.6 %. Even after

a higher amount of applied strain, there were no new cracks and no expansion of the existing cracks visible. It is important to note that classical bulk semiconductors have breaking points at values less than 1% of strain.[107] At higher amounts of strain for smaller areas surrounded by cracks, there is inhomogeneity of the strain indicated by the decrease of the exciton position redshift. Inhomogeneity drastically rises at the highest strain, as indicated by white arrows in **Figure 68(e)**. Although cracks minimize strain transfer for smaller areas, with areas larger than 20 µm, there is enough of the surface in contact with the substrate for adequate strain transfer. Positions indicated by green arrows in **Figure 68(e)** exhibited homogeneity of the absorbance spectra even at the highest applied strain.

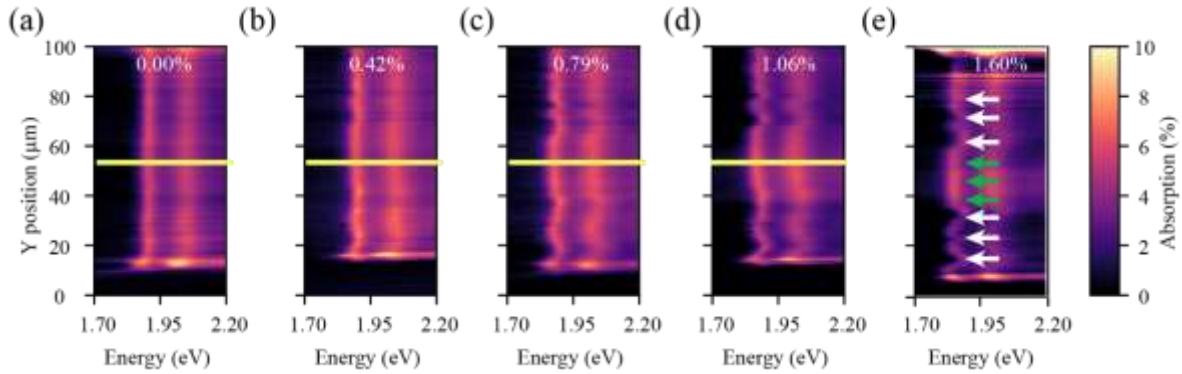

Figure 68. *Spatially resolved absorption spectra under five different levels of strain: 0%, 0.42%, 0.79%, 1.06%, and 1.60% on (a), (b), (c), (d), and (e), respectively. The spectra were measured along the red line in* ***Figure 66****(b). The horizontal yellow line indicates the position where the spectra shown in* ***Figure 67****(a) are extracted. In panel (e), white arrows indicate drastic spatial inhomogeneity of spectra, in contrast to an area marked by a green arrow. [Adopted from Ref.* [139]*].*

We conclude that grain boundaries do not interfere with strain propagation in large-scale 2DM monolayer sheets. The absorbance uniformity was maintained even at the highest strain values if no cracks were in the vicinity. Slippage of MoS_2 sheet is mainly caused by cracks that induce local strain variations, which drastically enhance for higher strain values and result in 2DM slippage. We emphasize that those cracks are inherent from the fast changes of the thermal gradient present during the growth and are not induced by strain. Those cracks can be avoided with a more delicate growth procedure involving slower changes of the thermal gradients.[214] Our results confirm that large-scale CVD-grown monolayers possess the same mechanical quality as exfoliated flakes and are a perfect platform for strained optoelectronic devices and strain sensors.[139]

5.2. Resistance

A large-scale MoS_2 sheet was transferred via stamping transfer from a Si wafer on a PC sheet with pair of Au/Ti electrodes fabricated by stencil lithography. Sample resistance was measured while strain was varied, as described in subsection **2.5.1**.

The success of transfer was determined by quick inspection with an optical microscope and reflectance spectroscopy.[154] As previously discussed, CVD-grown monolayer sheets can contain multilayers, which occur in the middle of the seed or at intersecting grains of MoS_2. Therefore, before starting any I-V measurements, reflectance spectroscopy was employed in multiple spots in the channel to confirm that the transferred MoS_2 sheet is a monolayer. The reflectance spectrum in **Figure 69(a)** shows measured data and resultant fits for the A (652 nm) and B (608 nm) exciton. Additionally, AFM measurements were performed to determine sample morphology. Majority of the monolayer sheet was uniformly transferred without any significant damage, as shown in **Figure 69(b)**. Contaminations, most likely PDMS residue from the transfer, scarcely cover the MoS_2 surface. However, certain contamination arises from the substrate. In some regions, MoS_2 was not transferred, indicated by a pink dashed line, while in some areas cracks were induced, indicated by a green dashed line in **Figure 69(b)**. Both types of those regions are surrounded by a ring of contaminations, whose morphology most likely causes local blistering of 2DM, resulting in cracks or inadequate transfer.[66,166] An adequately transferred MoS_2 sheet follows the contour of the Au-PC-Au with bending at electrode edges while maintaining relatively uniform morphology in the channel, as shown in the linescan in **Figure 69(c)**. Even though such damaged regions may occur, the rest of the MoS_2 in the channel was adequately transferred, with homogenous morphology and occasional contaminations on top, as shown in the AFM topograph in **Figure 69(d)**.

After the device was fabricated, i.e., MoS_2 was transferred on the electrodes, its I-V characteristics were measured under applied strain, as depicted in **Figure 69(e)**. First, I-V sweeps were performed, measuring the current between two electrodes while varying their potential. This process is repeated for different amounts of uniaxial tensile strain induced by the three-point bending motorized stage described in detail in subsection **2.6.2.**. The resistance vs. strain GF can be determined by measuring I-V sweeps under different amounts of strain. GF of change of the resistance vs. strain is calculated by $GF = (\Delta R/R_0)/\varepsilon$, where R_0 is resistance without applied strain, ΔR change of the resistance under applied strain while ε is the amount of the applied strain.[77]

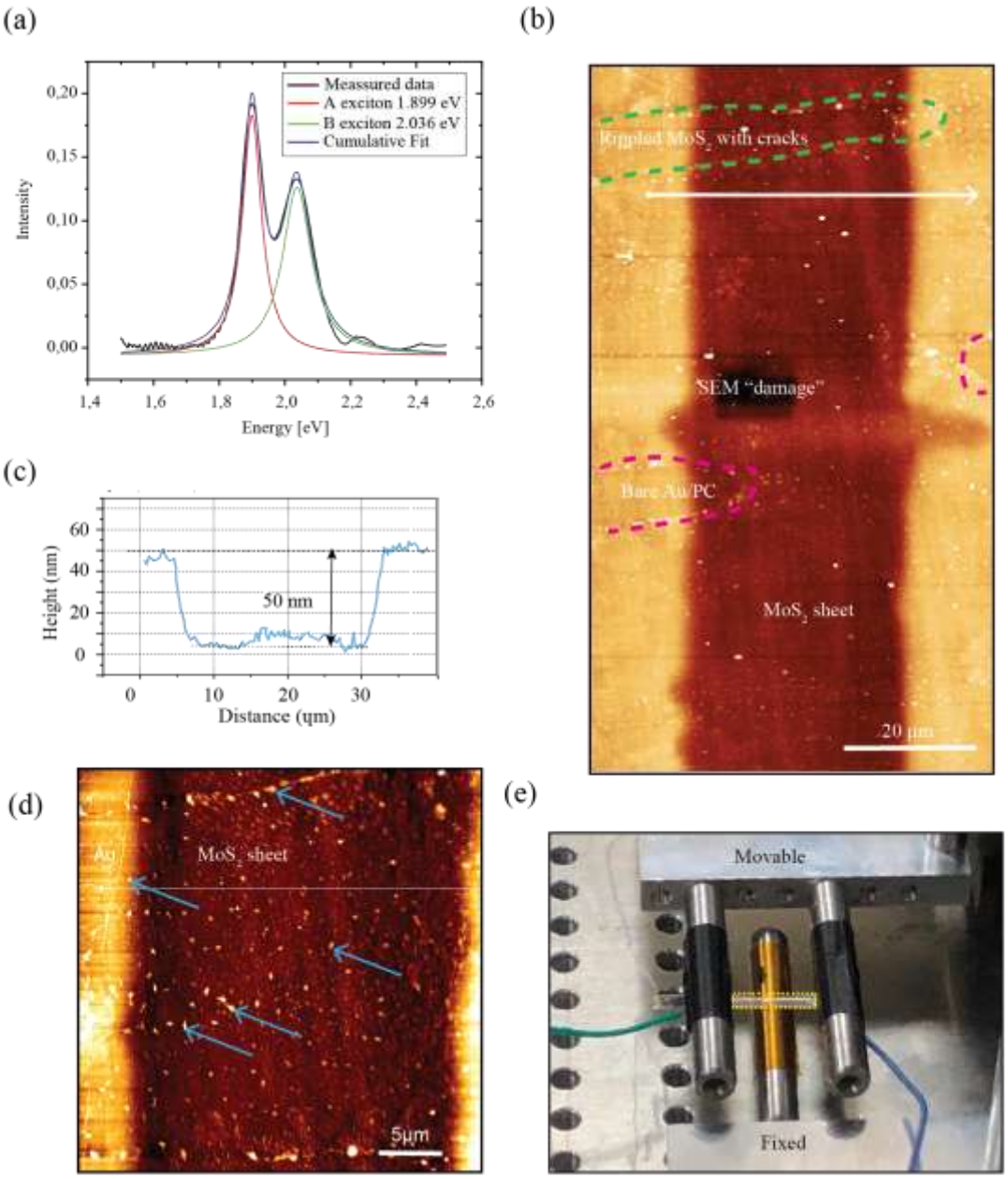

Figure 69. *Pre-strain measurements of MoS_2 on Au electrodes on PC. (a) Microreflectance spectra of MoS_2 monolayer sheet transferred on top of the electrodes on PC sheet. (b) Large area AFM topograph of the sample, with visible SEM-induced damage. Pink dashed lines indicate a bare Au/PC without MoS_2 due to blistering around contaminations, while the green dashed line indicates an area where MoS_2 rippled and cracked due to the same contaminations. (c) MoS_2 line profile taken along the white arrow in (b). (d) AFM topograph of the sample with no visible cracks in 30 µm x 30 µm sized region. Blue arrows indicate transfer-induced contaminations. (e) Three-point bending setup with the sample inserted and highlighted by a yellow dashed rectangle, at 0% strain input.*

Figure 70(a) shows I-V sweeps under different amounts of the applied strain, with a maximum value of 1%. By increasing the tensile strain in the MoS_2, resistance has decreased. The average gauge factor GF for measurement shown in **Figure 70(b)** was calculated as GF = 70 ± 3, which is roughly 60% of GFs previously best reports for MoS_2 monolayers.[77,119] It is important to note that previous reports on monolayers were exfoliated flakes, while on large-scale CVD-grown 2DMs multilayer regions can occur. Moreover, previous reports show that multilayers, such as trilayers, result in lower GF values.[76,77] As a result, our lower GF values could arise from multilayer contributions to device conductivity. However, as previously discussed, reflectance spectra showed that A and B exciton positions correspond to MoS_2 monolayer over the whole channel. So most likely transfer-induced defects disclosed in AFM topographs give rise to the reduction of our GF value.

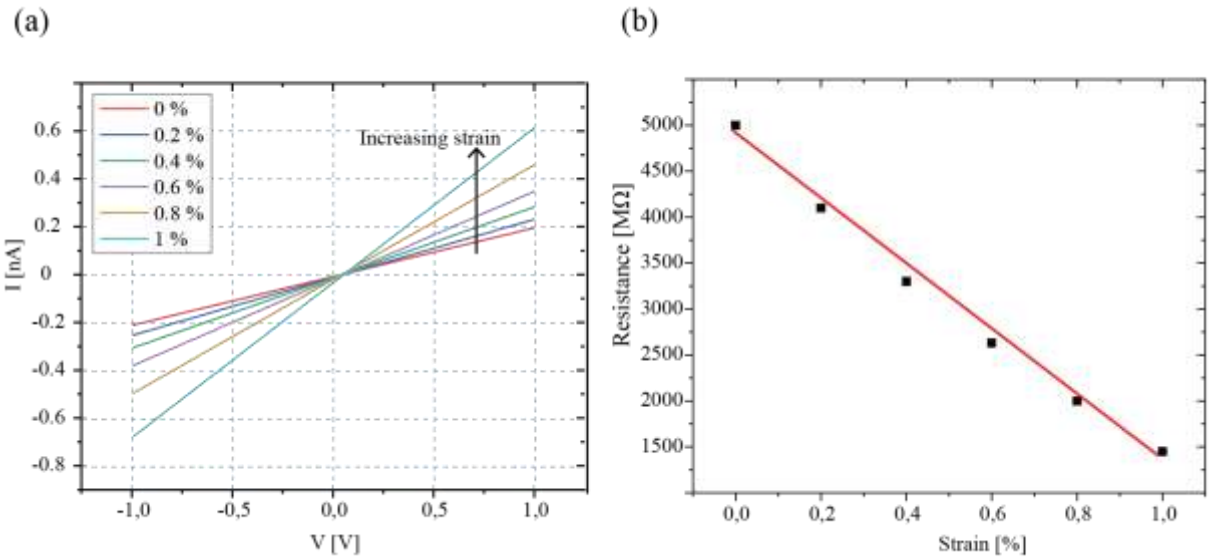

Figure 70. Transport characterisation of MoS_2 monolayer sheet up to 1% of applied strain. (a) I-V characterisation under different levels of applied strain.(b) Resistance vs applied strain.

The sample was tested over a period longer than 60 hours and 20 bending cycles up to 0.6% strain. Each cycle consists of 10 load steps and the subsequent 10 unload steps. I-V sweeps are performed at the start of the load/unload cycle and after each step. As a result, one bending cycle corresponds to 10 load steps while a strain is increased by 0.06% at each step, after which strain is released in the 10 unload steps to 0% of applied strain. That way, 20total I-V measurements correspond to one complete cycle, with the 1st and the 21st measurement at 0% strain and the 11th step at the highest strain level in the cycle. I-V maps of measurement are shown in **Figure 71**, where the Y-axis corresponds to the voltage applied, colour scale indicates the measured current, and X-axis set as step number (top X-axis indicates the corresponding

cycle number instead of step number). Our results indicate that even an unprotected MoS_2 monolayer can be used in strain devices for many cycles and long periods of time under ambient conditions.

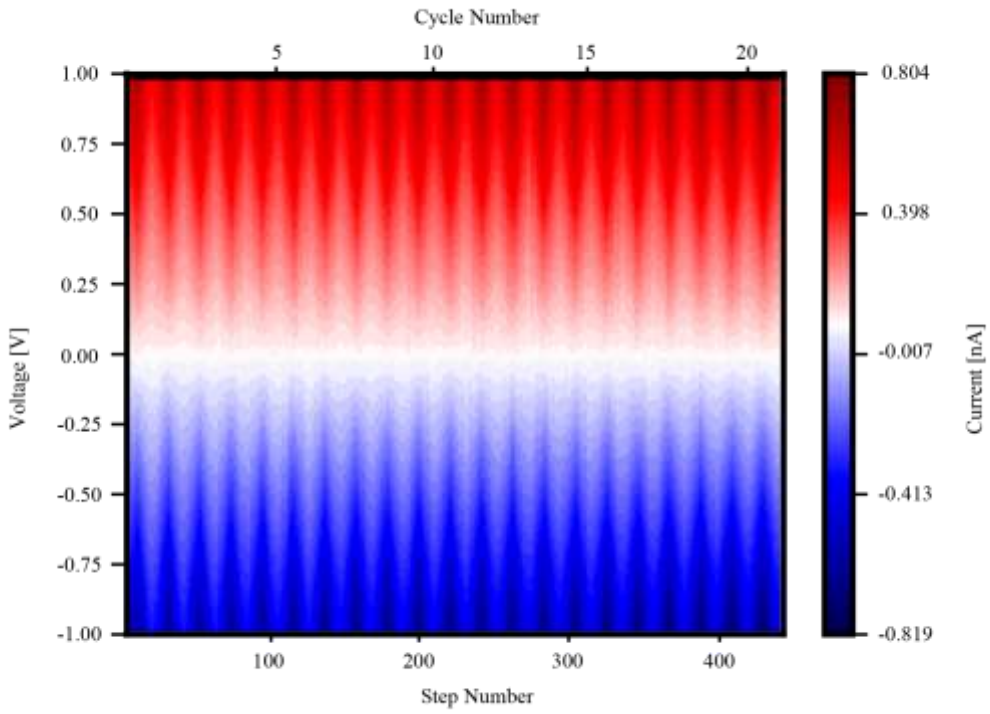

Figure 71. *Transfer characteristic map of MoS_2 on a PC substrate with an applied voltage on the Y-axis, a step number on the X-axis, and colour scale as a measured current. Measurement was done for 20 cycles of bending, where each cycle consists of 21 steps in which strain increases from 0% up to 0.6% and back to 0 %, all in 0.06 % increments, i.e., decrements.*

At each new step, corresponding resistance is calculated from the I-V sweep to determine resistance vs. strain GF. **Figure 72(a)** shows the dependence of resistance on step number for 20 cycles. From there, it can be seen that the resistance decreases with the strain increase (load) and subsequently rises to the starting value when strain is released (unload) after a complete cycle. When comparing values for the first three cycles, it is visible that measurements are stable for each of them. However, in the fourth cycle pronounced drop in resistance happens, of about 10%. Most likely due to the pre-strain release, which manifested in blisters and mismatch of MoS_2 sheet around cracks that are inherent or occurred after transfer of MoS_2.[116,215] Resistance stabilizes in further cycles that were done over the timespan of 60 hours, during which resistance gradually decreased for an additional ~10%. This decrease is most likely dominated by exposure to the environment in which various molecules from the air can bond to the surface of 2DM through time.[82] Stability of fabricated device can be confirmed

by observing gauge factor over time. **Figure 72(b)** shows GF for each half cycle, where an odd number of half-cycle corresponds to applying tensile strain by bending, and an even number of half-cycle to the release of strain to 0%. Even though the GF changes for each new cycle, variations after the first three cycles are less than 8% from an average GF = 66 ± 2, which confirms the stability of the fabricated device over more than 60 operating hours in ambient conditions. Such results endorse the application of large-scale monolayers of MoS_2 as highly precise and stable strain or tactile sensors.

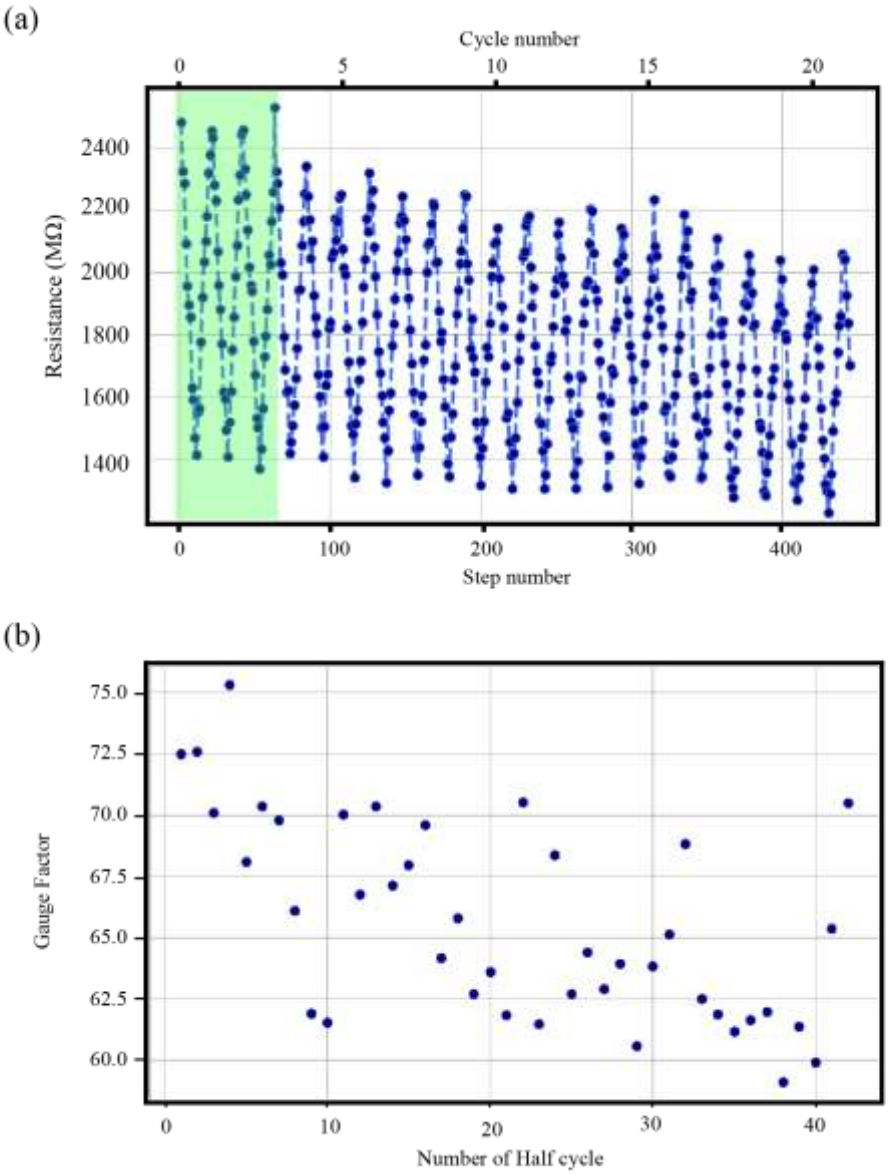

Figure 72. *Resistance and GF of 20 cycles of bending MoS_2 on a PC substrate up to 0.6% of strain. (a) Resistance vs. step number, with indicated cycle number on an upper scale and green rectangle that shows first three cycles after which pre-strain is released. (b) GF of MoS_2 on a PC substrate for each new half cycle over subsequent 20 cycles of bending.*

5.3. Photocurrent

In the same configuration as for the previous section, MoS_2 device was characterized by photocurrent spectroscopy at various amounts of tensile strain, as shown in **Figure 73(a)**. The photocurrent was determined by measuring the current before, during and after illumination by monochromatic light. While a potential of 1 V was applied to the MoS_2 via electrodes, as shown in **Figure 73(b)**. Two types of light sources were used for different spectral ranges and wavelengths. The whole setup we used is described in detail in subsection **2.5.2.**.

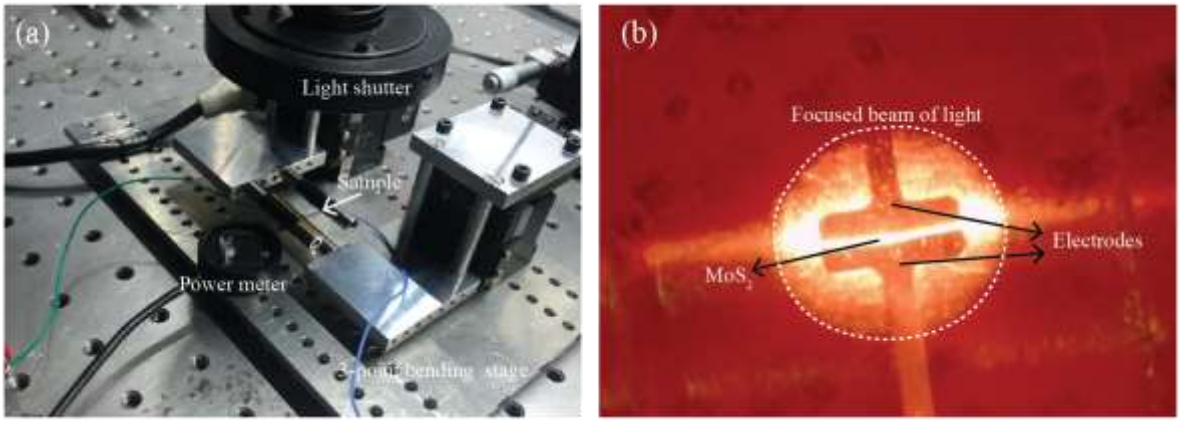

Figure 73. *Photoconductivity measurement of MoS_2 sample at different tensile strains. (a) Photograph of a sample fixed on a three-point bending stage with a light source coupled to the shutter which controls light exposure of the sample. (b) Optical microscope image of the sample under exposure to light.*

Measurement was performed for 30 seconds before exposure, 45 seconds under exposure and 60 seconds after exposure to the LED light. Used LED lights cover the wavelength range from 365 nm to 850 nm. The photocurrent was determined as "on current" subtracted by the "off current" at each selected wavelength. **Figure 74** shows photocurrent generated in MoS_2 monolayer at 0.0%, 0.3% and 0.9% of tensile strain. With the increase of the tensile strain, a notable photocurrent increase and a redshift of exciton energies are visible. Photocurrent generated by exposure to light increased by three times at 0.9% of tensile strain. Such enhancement is seen and investigated in more detail with a second photocurrent spectroscopy setup, as described in the following paragraphs. Device photoresponsivity, ratio of generated photocurrent and the incident illumination power, is negligible for light over 680 nm (cut–off), which signifies that photons do not have enough energy to excite electrons from the valence to the conduction band at wavelengths corresponding to 1.8 eV (680 nm), which coincides with the bandgap of monolayer MoS_2.[216] While on lower wavelengths, higher-energy electrons are

excited, and the photocurrent is generated. The transition most likely increases for higher photon energies, which can be seen in the increase of the photocurrent and subsequently photoresponsivity down to 400 nm excitation wavelength.[217]

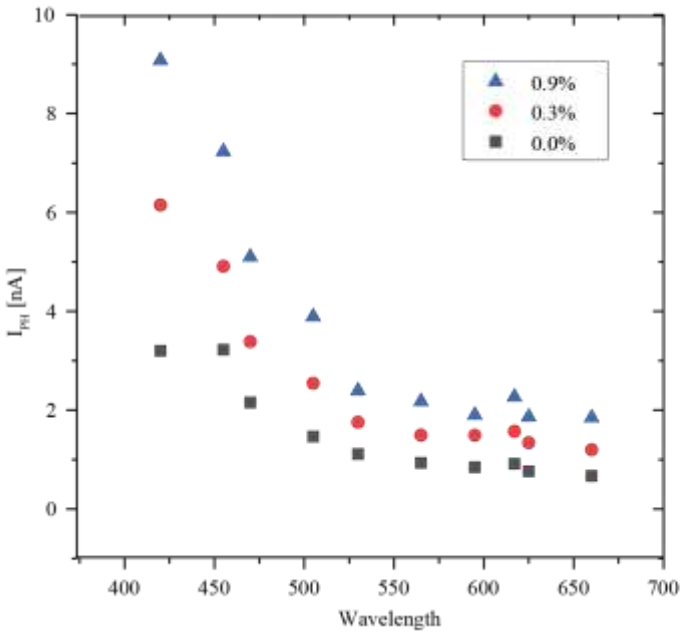

Figure 74. *Photocurrent spectroscopy in MoS_2 monolayer sheet by exposure to the LED light with different wavelengths, at 0.0%, 0.03% and 0.06% of tensile strain.*

For a more detailed inspection of the photocurrent behaviour under strain, a second setup was used in the photon energy range corresponding to exciton energies (580 nm to 700 nm) with illumination wavelengths changed in 5 nm steps. **Figure 75** shows photocurrent measurement by a continuous light source for 0.0%, 0.03%, and 0.09% of induced tensile strain, with the first peak of each curve corresponding to 550 nm and each subsequent peak to 5nm increase of light source wavelength. Even on unprocessed data, it can be seen that the total current increases with an increase of strain. Due to persistent photoconductivity (PPC), after the illumination was terminated, the device's conductance was enhanced and remained in a high-conductivity state during the whole measurement.[218] This delayed phenomenon is governed by the relaxation of the excess electrons in the conduction band to hole-trapped sites.[219] It can be seen that at higher amounts of the applied strain PPC effect is also increased, which results in the larger photo gain at higher tensile strain.

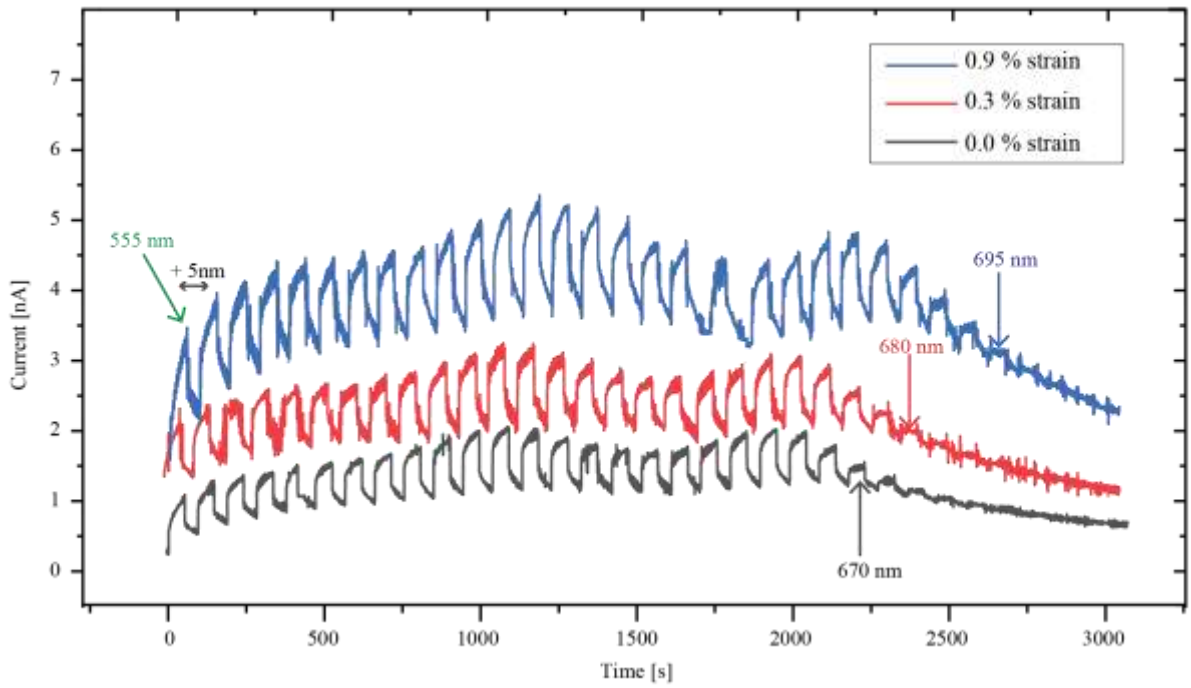

Figure 75. *Continuous measurement of MoS_2 sheet current as a function of time with cyclic exposure to light, where each subsequent peak corresponds to illumination by light with 5 nm higher wavelength than the previous peak. Measurements for 0.0%, 0.03% and 0.06% of strain are shown, where the first wavelength was 555 nm, while cut-off wavelengths are marked correspondingly for each strain value.*

Figure 76 shows the OFF-ON-OFF illumination period with 660 nm wavelength at different strain levels. After illuminating the sample, rapid current growth can be seen, with a slow saturation trend. Rapid response is also seen when illumination is turned off, after which decay starts. Device response time can be derived from the 10%-90% method, as the time that passes from 10% to 90% value of saturation photocurrent.[220,221] In our work, each rise and decay part was fitted with the bi-exponential function to determine the exact amount of generated photocurrent and response time. Other methods of fitting and analysis were also used, but we did not achieve any better fits with other functions.[218] Additionally, by subtracting off current (I_{OFF}=10% $I_{saturation}$) from on current (I_{ON}=90% $I_{saturation}$), the PPC effect can be eliminated from further photocurrent analysis.

Two mechanisms control photocurrent generation, photoconductance and photogating. Through the response time of the device, it can be determined which mechanism is dominant. The typical response time for photoconductance-dominated devices is less than 10 ms, in which case photoexcited electrons and holes are separated by the bias voltage that leads to an increase of the current in the material. The response time for photogating-dominated devices can be

more than 10 s, in which case photoexcited electrons drift due to bias voltage while holes get trapped, and as a result, extra electrons move to the channel. After each drifting electron reaches the drain electrode, one new electron must jump from the source electrode due to charge conservation in the channel. That way, the photoconductive gain is proportional to the ratio between electron drifting time and a hole trapping time. Generally, photoconductive-dominated devices have a fast response time but low photoresponsivity values, while photogating-dominated ones are usually slower but achieve higher values of photoresponsivity. Our devices show a slow response time from ~4 s at 0.0% to ~7 s at 0.3% and ~8 s at 0.9% of strain which indicates that devices are dominated by a photogating mechanism that gets more pronounced with the application of strain.[175]

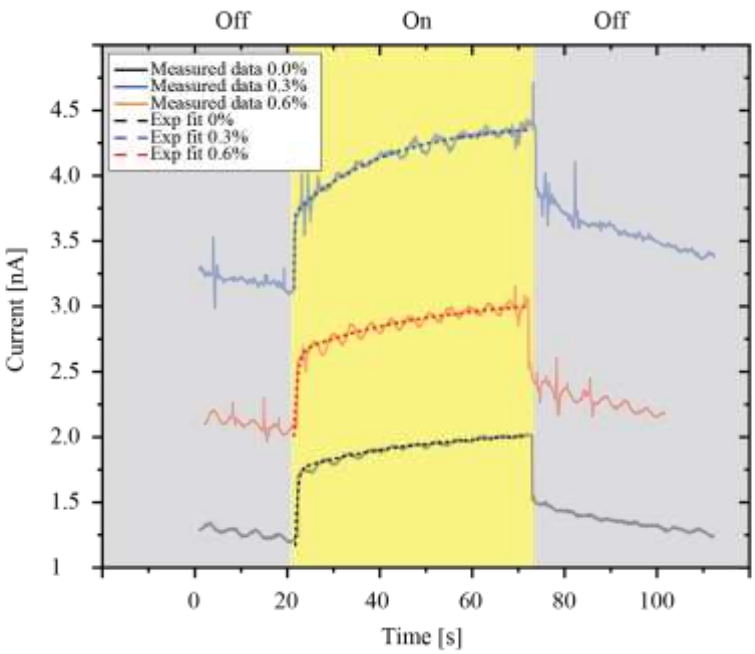

Figure 76. *Photo response of MoS_2 for light illumination of 645 nm, with the light turned on for 45 seconds and switched off afterwards. Measured current and corresponding double exponential fit are shown for 0.0%, 0.03% and 0.6% of tensile strain.*

Figure 77 shows the plot of photocurrent at different amounts of strain for wavelengths from 585 nm to 695 nm. In that wavelength range, energies corresponding to B (604 nm = 2.05 meV) and A (645 nm = 1.92 meV) exciton in MoS_2 are found. Again, like in LED light spectroscopy shown in **Figure 74**, with an increase of tensile strain, photocurrent increases and the spectra undergoes a redshift, which is in accordance with previous reports.[115,119] Each spectrum was fitted with two Lorentzians to determine the amount of the redshift. Corresponding GF calculated for a shift of the A exciton is GF=51±6 meV/%. Such value is in accordance with

previous reports on the same techniques and similar setups, confirming adequate strain transfer during whole measurements.[119,139] It is visible that the device cut-off point due to the red shift of spectra increases to higher wavelengths by application of strain. The cut-off point is a value at which wavelength illumination does not result in photocurrent generation.

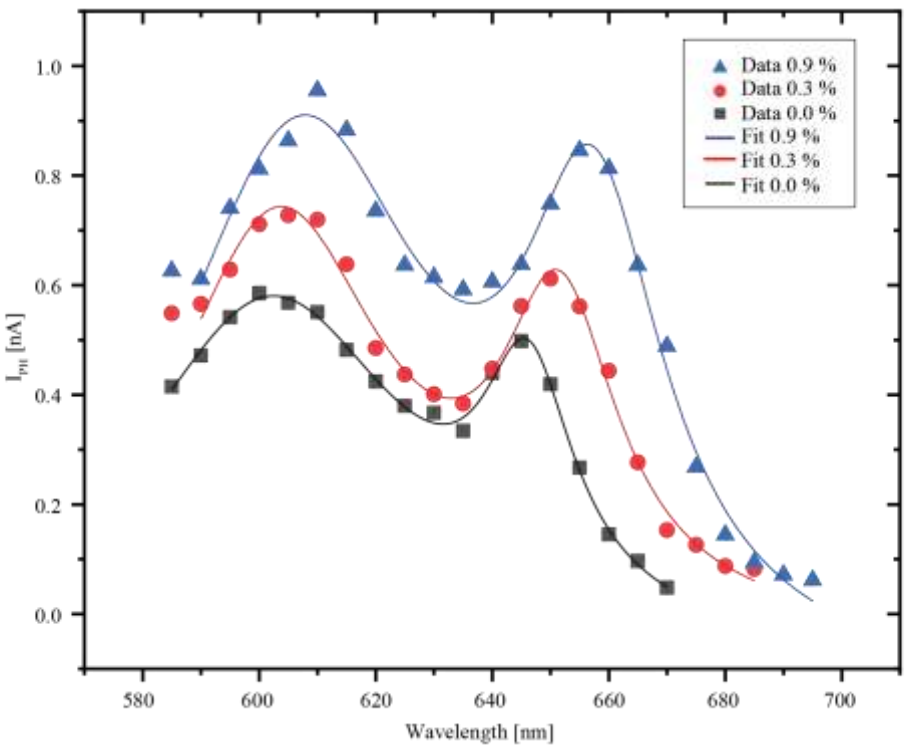

Figure 77. *Photocurrent spectroscopy of MoS_2 monolayer sheet with exposure to a continuous light source with different wavelengths, with 0.0%, 0.03% and 0.06% of tensile strain. Data shows the energy range in which B (604 nm) and A (645) nm exciton peaks are found.*

Our results confirm that MoS_2 photoresponse can be enhanced by applying tensile strain. Photocurrent and photoresponsivity increase by a factor of 3 at 0.9% strain, and the device functionality is broadened to higher wavelengths. Our device is dominated by a photogating mechanism that gets more pronounced by strain, which is visible in the longer response time at higher strain. Most likely, the distance between atoms increases with tensile strain, which prolongs hole trapping in mid-gap states, occurring on grain boundaries and defects.[119,219,222] At the same wavelength and applied voltage, photocurrent increases for higher strain levels. This means that either carrier mobility, which affects the time electron needs to reach drain electrode, or trapping of the holes is increased. Because our response time increases with strain, the trapping of the holes is most likely significant, which causes the photocurrent rise. However, does the number of possible trap states increase, or do holes stay trapped for a longer time, and what exact microscopic mechanism causes the increase of hole trapping is still unclear. Various

papers noticed similar behavior of the photoresponse of strained MoS_2 photodetectors but failed to unambiguously determine that strain is the main factor for such enhancement and exactly which microscopic mechanism could explain such change on different strains.[119,223] Previous reports show that in CVD-grown MoS_2 monolayers highest amount of trap states is around grain boundaries.[222] Grain boundary defects are accommodated mainly through the lattice distortions, and with applied strain, those distortions can get enhanced.[28] In that way, it seems that with the application of the strain, trap states in grain boundaries of large-scale MoS_2 get modified, resulting in a longer period of the hole trapping, which in the end results in increased photo gain at higher levels of strain.

5.4. Photoluminescence

The PL maps of MoS_2 on Au/PC were derived by taking a series of PL point spectra at positions with 0.5 µm steps on the X and Y-axis. Maps were done after a series of sample tests disclosed in the previous two sections. As seen in **Figure 78**, the exciton positions are redshift at the edge of the electrodes, caused by the local MoS_2 bending. Overall, inhomogeneity of PL spectra is probably the result of local strain caused by the morphology of the substrate and the transfer of MoS_2 monolayer. However, it cannot be excluded that the residual strain is partially caused by sample bending during previous characterisations.[224] AFM measurements depicted in **Figure 69** show that the monolayer lays flat over the PC sheet in the middle of the channel and that it is not genuinely suspended over the electrodes. To determine the exact amount of the strain on the surface, the unstrained energy value of A exciton peak was averaged over multiple positions in the middle of the channel, E_A=659 nm. PL values are shifted by -15 nm to values derived for an unstrained sample with photocurrent spectroscopy. The first possible reason for the shift could be that there is some residual strain in MoS_2 from previous measurements performed on the sample. Secondly, the previous reports for the aged TMDs showed that aging of the 2DM can cause a redshift of more than 10 nm.[114,224] Third reason for shift could be related to the PL spectrum not representing the total exciton density of states because photoexcited carriers undergo relaxation processes before recombining radiatively. As a result, the PL spectrum corresponds to the distribution of the lowest exciton energy states, while the photocurrent spectrum represents the distribution of all exciton states.[114] Such alteration in the position of the exciton peaks in MoS_2 monolayers depending on the type of optical spectroscopy (absorption vs. emission) is called Stokes shift.[225,226] As seen in previous reports, Stokes shift can also get modified by strain.[227]

To determine the amount of strain distributed over the sample, deviations that are caused by different substrate should be excluded. For example, the blue shift of 5 meV for the exciton energy values of MoS_2 at Au electrodes (position 3 in **Figure 78**) with respect to the MoS_2 at the PC in the channel (position 1) can be attributed to a difference in nonradiative and radiative exciton decay channels for MoS_2 at different substrates.[228] In correspondence with previously mentioned variations, the amount of the strain caused by bending the monolayer (position 2) is redshifted by -18 ± 6 meV, which would correspond to less than 0.4% of the strain. Redshift caused by local bending on the edges gradually reduces towards the middle of the channel (position 1). Additionally, certain deviations of the central positions at the middle of the channel are probably due to different local strains (variations up to 0.2 %) caused by substrate morphology, most likely governed by contaminations between PC and MoS_2. However, as previously commented, some of those variations could be caused by differences in the substrate interaction.

A map of the FWHM for A exciton is shown in **Figure 78(b)**. Previously, it has been shown that FWHM broadening can be attributed to a change of exciton-phonon coupling due to local strain variations.[114,229] Also, certain broadening of the signal could be a consequence of the defocusing of the optical setup, which can happen with large-scale area maps recorded by step-by-step acquisition. Defocusing is caused by change of the z position of the sample, which can be so drastic that the whole signal is lost. To minimize defocusing, sample was focused as soon as PL intensity dropped by more than 25%. In the end, we cannot exclude that the local deviations of the strain over the same surface are enhanced by the previous slippage of the monolayer, which could have occurred during previous bending experiments of the sample during which strains up to 2 % were applied.

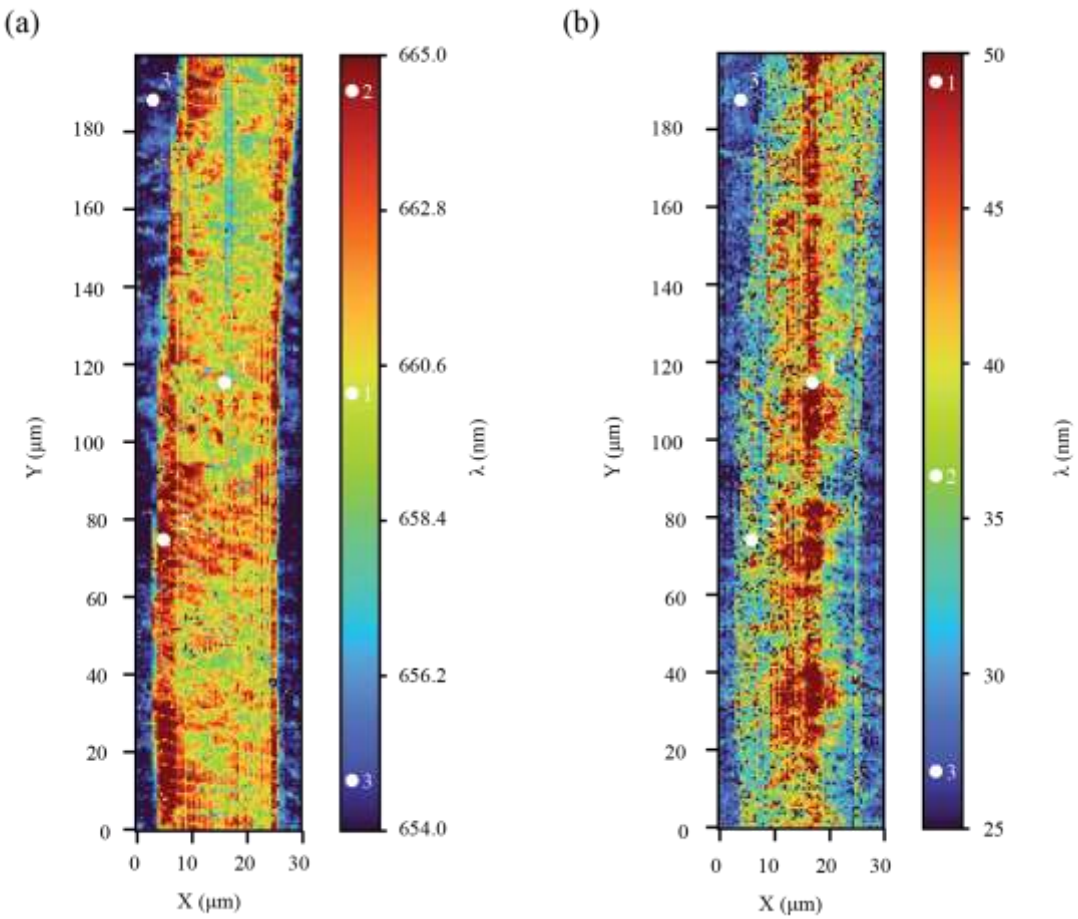

Figure 78. *PL maps of MoS_2 monolayer placed over electrodes on a PC sheet. (a) Map of the A exciton energy positions. (b) Map of FWHM of A exciton peak. Characteristic values for three different areas are marked with 1 for monolayer directly at PC inside of the channel, 2 for a position at which monolayer bends over the edge of the electrodes and 3 for monolayer over the Au electrodes.*

After large area maps of the sample, smaller maps (40 µm x 40 µm) were recorded at 0.0% and 0.9% as shown in **Figure 79(a)** and **(b)**, respectively. At 0.9 % of applied strain, a redshift of exciton position up to -17 meV (+6 nm) can be seen with spatial variations. Such results indicated inadequate strain transfer, as redshift up to -40 meV was expected from photocurrent and absorbance spectroscopy in sections **5.1.** and **5.4.**. There are three possible reasons for lower values. The reduction of the redshift could be caused by the slippage that may have occurred during previous bending experiments through which the sample was subjected to higher strain values. Secondly, as measurements were performed after more than 30 days since fabrication (transfer of MoS_2 on PC with electrodes), aging can induce additional strain in 2DM and decrease redshift.[114,224] Third reason for inadequate strain transfer could be the 2-

point bending employed, which has certain setbacks in contrast to the 3-point bending stage used for previous measurements of the sample with this configuration, such as defocusing and possible movements of the PC edges in respect to manipulators.[75,157]

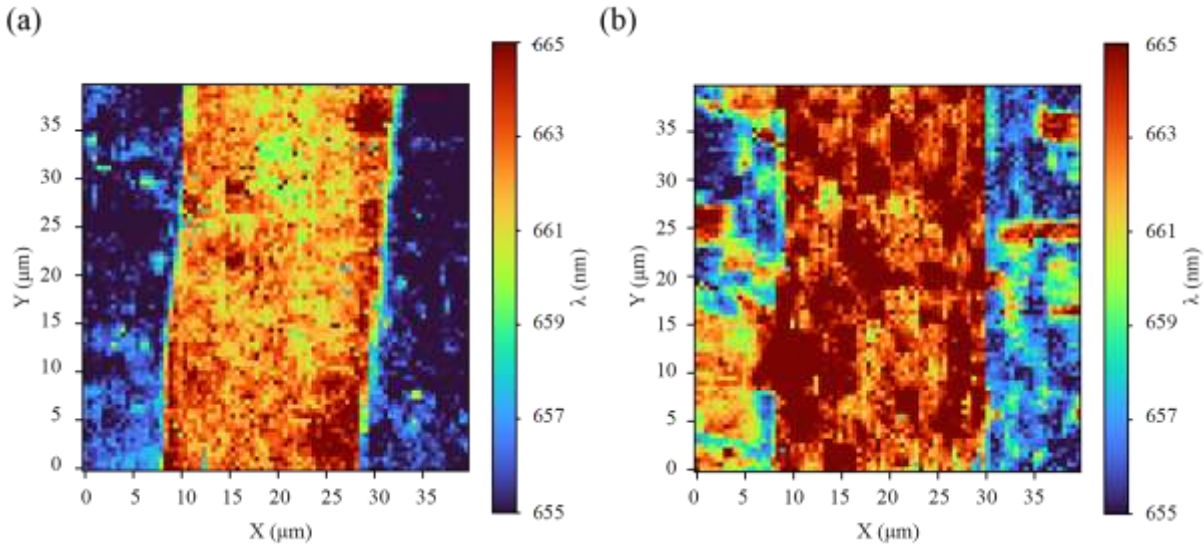

Figure 79. *A exciton position derived from PL mapping. (a) The map at 0% of applied strain. (b) The map at 0.9% of applied strain.*

Chapter 6

Conclusion

Several selected 2DMs, exhibiting substantially different physical and chemical properties were investigated to determine their suitability for flexible electronic devices. Monolayers of Bo, Gr, and MoS_2 as well as MoS_2/Gr heterostructures, were investigated. Morphological and optical characterisations were done for all mentioned materials before and after transferring to a suitable substrate. FETs were fabricated from Gr and MoS_2 monolayers on Si wafer by stencil and e-beam lithography. Ultimately, we have shown that the MoS_2 monolayer on PC can be used as a highly sensitive strain sensor by utilizing optical or electric signal detection. Furthermore, MoS_2 can be used as a flexible photodetector whose performance can be enhanced by the application of strain.

After the synthesis of Bo in UHV by segregation enhanced epitaxy, samples were characterized *ex situ* by AFM, SEM, and Raman spectroscopy to confirm its ambient stability. Afterwards, two-step electrochemical transfer was employed to transfer Bo from Ir(111) crystal to the Si wafer, where the same techniques were used to determine the success of the transfer. Raman spectra on both substrates were compared with DFT calculations of freestanding Bo to verify the quality and ambient stability of the Bo monolayer. A similar approach was applied for the heterostructure of MoS_2/Gr, in which MoS_2 islands were in the range of 100 nm in lateral size. Also, two-step electrochemical method was used to transfer the heterostructure from Ir(111) on a Si wafer, while AFM, Raman, and PL spectroscopy were employed to verify the transfer. Our work presents a method that enables the utilization of such heterostructures at any substrate that would be required for future optoelectronic devices. We have presented that adsorbate-sensitive and complex 2DMs, such as large-scale Bo or MoS_2/Gr heterostructure, could be mechanically manipulated by electrochemical transfer, enabling their exploitation in many devices, including flexible electronics.

Gr monolayers were used mainly as a test 2DM for constructed transfer and transport characterisation setup, which aided optimization of lithography and transfer parameters used for other 2DMs investigated in our work. At the same time, our research focused on MoS_2 monolayers. A variety of CVD-grown MoS_2 samples with different sizes, shapes and quality were analysed. SEM and AFM micrographs have identified many potential complications for

exploiting MoS_2 in any electronic device. Flakes can have different decorations on the edges and grain boundaries, bulky leftovers of precursor, bilayer structures or multilayer areas, and physical cracks. Slightest deviations from ideal growth parameters can lead to drastically different properties, which are not only reflected in morphology observed by AFM and SEM but also in optical and transport properties. We have shown that to utilize those monolayers, cracks, contaminations and other decorations can be avoided by targeted fabrication of the electrodes, e.g., e-beam lithography. Although morphological obstacles can be avoided, the deviations from defect-free MoS_2 are manifested in PL and Raman spectra (intensity, position, and shape of the peaks) or resistance and mobility (derived from I-V of FETs), which can only be avoided by better control of growth parameters. The homogeneity and reproducibility of MoS_2 optical and transport properties can be improved in large-scale samples where isolated flakes coalesce into a continuous sheet. These samples may exhibit the same type of morphology defects as seen for isolated flakes, such as cracks or multilayer areas. However, in contrast to isolated flakes where cracks prevent any current flow through 2DM, with large-scale samples, cracks usually propagate only inside one grain of 2DM, enabling current flow around the defects.

Photodoping and electric field doping of MoS_2 were investigated with PL spectroscopy, during which we demonstrated that the electric field or laser power change can control the trion population. Charged quasiparticles trions present an attractive tool for optoelectronic devices, in contrast to neutral excitons. Finally, we have fabricated MoS_2-based FETs in a back-gate configuration on a Si wafer. We have shown that in exposed configuration, the device operability can be achieved but with lower mobility and on/off ratio values than previously reported values on top-gated MoS_2 FETs.

Due to obstacles occurring with isolated monolayer flakes, large-scale CVD-grown MoS_2 monolayers were chosen for fabricating flexible devices and strain-dependent measurements. The derived GF, obtained from absorbance spectroscopy under applied tensile strain by observing energy positions of A and B exciton peaks in large-scale MoS_2 monolayers sandwiched in PDMS/MoS_2/PC structure, are in agreement with previous reports of similar MoS_2 systems. In addition, we have investigated how strain propagates across the cracks and grain boundaries in large-scale monolayers strained up to 1.6% by the two-point bending stage. We have shown that grain boundaries do not prevent strain transfer while cracks cause a spatially isolated strain decrease in their vicinity. Our results confirm that CVD-grown large-scale MoS_2 monolayers are suitable for flexible and stretchable devices as they can be bent

without damage to the strain values two times larger than the silicon breaking point. The PDMS/MoS_2/PC configuration can be utilised as flexible and stretchable strain detectors or tactile sensors based only on optical signals without needing electrodes.

Furthermore, large-scale MoS_2 monolayers were transferred on PC with Au electrodes (MoS_2/2xAu/PC sensor) to analyse how the transport properties of monolayers change under strain. In agreement with previous reports, our samples exhibit a decrease in resistance with an increase of tensile strain. The resistance of fabricated samples was monitored continuously during repetitive bending cycles, in which increasing tensile strain up to 0.9 % and subsequent strain release were applied. Samples were tested for 20 cycles of bending over a period longer than 60 hours and showed no significant deviations to the resistance GFs. We have demonstrated that large-scale MoS_2 monolayers can be repetitively used as strain detectors by measuring resistance changes in exhibited configuration. In such a configuration, in which the MoS_2 monolayer has a free surface, 2DM can be additionally functionalized and then used as a flexible detector of various chemical compounds or molecules.

With PL maps of the MoS_2/2xAu/PC sensor, we have investigated local strain variations in monolayer and their behaviour under applied external tensile strain. In an unstrained sample, deviations of exciton peaks are caused by local bending of monolayer over the edge of the electrodes and by substrate morphology which can be seen in AFM topographs. On the other hand, the homogeneity of the PL map slightly increases with external strain, probably caused by the flattening of locally strained areas of the monolayer. A more detailed analysis is required to conclude the main reasons for lower calculated GF values of exciton peaks. However, the most indicative is that for 2DMs without encapsulation, a two-point bending setup is somewhat inferior to a three-point bending setup.

In addition, photocurrent spectroscopy was performed on the MoS_2/2xAu/PC sensor at different amounts of the tensile strain up to 0.9%. Fabricated devices exhibited high photoresponsivity and a long response time, which is characteristic of photodetectors dominated by photogating mechanism. We have demonstrated that with the increase of the tensile strain, exciton peaks and whole spectra undergo redshift (GF in agreement with previous reports), which causes an increase in the detection bandwidth. Additionally, we have shown that with tensile strain, the photocurrent and photoresponsivity increase several times at strain values even lower than 1%. Also, response time increased at higher strain, which indicates that enhancement of photoresponsivity is probably caused by the change of trap states and hole trapping time. However, an exact microscopic mechanism that causes enhancement is still to

be determined. We have shown that the MoS_2 monolayer can be utilised as a flexible photodetector. Most importantly, we demonstrated that applying the strain in the monolayer can increase its photoresponse several times compared to an unstrained sample.

References

1. Geim, A. K. & Novoselov, K. S. The rise of graphene. *Nat. Mater. 2007 63* **6**, 183–191 (2007).
2. Castro Neto, A. H., Guinea, F., Peres, N. M. R., Novoselov, K. S. & Geim, A. K. The electronic properties of graphene. *Rev. Mod. Phys.* **81**, 109–162 (2009).
3. Malard, L. M., Pimenta, M. A., Dresselhaus, G. & Dresselhaus, M. S. Raman spectroscopy in graphene. *Phys. Rep.* **473**, 51–87 (2009).
4. Ferrari, A. C. *et al.* Raman spectrum of graphene and graphene layers. *Phys. Rev. Lett.* **97**, 187401 (2006).
5. Schwierz, F. Graphene transistors. *Nat. Nanotechnol. 2010 57* **5**, 487–496 (2010).
6. Novoselov, K. S. *et al.* Two-dimensional gas of massless Dirac fermions in graphene. *Nat. 2005 4387065* **438**, 197–200 (2005).
7. Novoselov, K. S. *et al.* Electric field in atomically thin carbon films. *Science (80-.).* **306**, 666–669 (2004).
8. Moore, G. E. No exponential is forever: but 'Forever' can be delayed! [semiconductor industry]. *2003 IEEE Int. Solid-State Circuits Conf. 2003. Dig. Tech. Pap. ISSCC.* **1**, 20–23.
9. Dennard, R. H. *et al.* Design of Ion-Implanted MOSFET's With Very Small Physical Dimensions. *IEEE J. Solid-State Circuits* **9**, 256–268 (1974).
10. Zhou, S. Y. *et al.* Substrate-induced bandgap opening in epitaxial graphene. *Nat. Mater. 2007 610* **6**, 770–775 (2007).
11. Dvorak, M., Oswald, W. & Wu, Z. Bandgap Opening by Patterning Graphene. *Sci. Reports 2013 31* **3**, 1–7 (2013).
12. Ye, J. *et al.* Bandgap opening in oxygen plasma-treated graphene. *Nanotechnology* **21**, 435203 (2010).
13. Zhang, W. *et al.* Opening an electrical band gap of bilayer graphene with molecular doping. *ACS Nano* **5**, 7517–7524 (2011).
14. Zhu, Y., Ji, H., Cheng, H. M. & Ruoff, R. S. Mass production and industrial applications of graphene materials. *Natl. Sci. Rev.* **5**, 90–101 (2018).
15. Mas-Ballesté, R., Gómez-Navarro, C., Gómez-Herrero, J. & Zamora, F. 2D materials: to graphene and beyond. *Nanoscale* **3**, 20–30 (2011).
16. Akinwande, D. *et al.* Graphene and two-dimensional materials for silicon technology. *Nat. 2019 5737775* **573**, 507–518 (2019).
17. Cheon, G. *et al.* Data Mining for New Two- and One-Dimensional Weakly Bonded Solids and Lattice-Commensurate Heterostructures. *Nano Lett.* **17**, 1915–1923 (2017).
18. Xu, M., Liang, T., Shi, M. & Chen, H. Graphene-like two-dimensional materials. *Chem. Rev.* **113**, 3766–3798 (2013).
19. Haigh, S. J. *et al.* Cross-sectional imaging of individual layers and buried interfaces of graphene-based heterostructures and superlattices. *Nat. Mater. 2012 119* **11**, 764–767 (2012).
20. Wang, Z. *et al.* Biological and environmental interactions of emerging two-dimensional nanomaterials. *Chem. Soc. Rev.* **45**, 1750–1780 (2016).
21. Geim, A. K. & Grigorieva, I. V. Van der Waals heterostructures. *Nat. 2013 4997459* **499**, 419–425 (2013).
22. Siao, M. D. *et al.* Two-dimensional electronic transport and surface electron accumulation in MoS2. *Nat. Commun. 2018 91* **9**, 1–12 (2018).
23. Splendiani, A. *et al.* Emerging photoluminescence in monolayer MoS2. *Nano Lett.* **10**, 1271–1275 (2010).
24. Mak, K. F. *et al.* Tightly bound trions in monolayer MoS2. *Nat. Mater. 2012 123* **12**, 207–211 (2012).
25. Beams, R., Gustavo Cançado, L. & Novotny, L. Raman characterisation of defects and dopants in

graphene. *J. Phys. Condens. Matter* **27**, 083002 (2015).

26. Cheiwchanchamnangij, T. & Lambrecht, W. R. L. Quasiparticle band structure calculation of monolayer, bilayer, and bulk MoS 2. *Phys. Rev. B - Condens. Matter Mater. Phys.* **85**, 205302 (2012).

27. Mouri, S., Miyauchi, Y. & Matsuda, K. Tunable photoluminescence of monolayer MoS2 via chemical doping. *Nano Lett.* **13**, 5944–5948 (2013).

28. Huang, Y. L. *et al.* Bandgap tunability at single-layer molybdenum disulphide grain boundaries. *Nat. Commun. 2015 61* **6**, 1–8 (2015).

29. Radisavljevic, B., Radenovic, A., Brivio, J., Giacometti, V. & Kis, A. Single-layer MoS2 transistors. *Nat. Nanotechnol. 2011 63* **6**, 147–150 (2011).

30. Lopez-Sanchez, O., Lembke, D., Kayci, M., Radenovic, A. & Kis, A. Ultrasensitive photodetectors based on monolayer MoS2. *Nat. Nanotechnol. 2013 87* **8**, 497–501 (2013).

31. Krainak, M. A., Sun, X., Yang, G. & Lu, W. Comparison of linear-mode avalanche photodiode lidar receivers for use at one-micron wavelength. *Adv. Phot. Count. Tech. IV* **7681**, 76810Y (2010).

32. Zeng, H., Dai, J., Yao, W., Xiao, D. & Cui, X. Valley polarization in MoS2 monolayers by optical pumping. *Nat. Nanotechnol. 2012 78* **7**, 490–493 (2012).

33. Chakraborty, C., Vamivakas, N. & Englund, D. Advances in quantum light emission from 2D materials. *Nanophotonics* **8**, 2017–2032 (2019).

34. Zhang, Z., Penev, E. S. & Yakobson, B. I. Two-dimensional boron: Structures, properties and applications. *Chem. Soc. Rev.* **46**, 6746–6763 (2017).

35. Tang, H. & Ismail-Beigi, S. Novel Precursors for Boron Nanotubes: The Competition of Two-Center and Three-Center Bonding in Boron Sheets. *Phys. Rev. Lett.* **99**, 115501 (2007).

36. Omambac, K. M. *et al.* Segregation-Enhanced Epitaxy of Borophene on Ir(111) by Thermal Decomposition of Borazine. *ACS Nano* **15**, 7421–7429 (2021).

37. Liu, X. *et al.* Geometric imaging of borophene polymorphs with functionalized probes. *Nat. Commun. 2019 101* **10**, 1–7 (2019).

38. Hou, C. *et al.* Borophene pressure sensing for electronic skin and human-machine interface. *Nano Energy* **97**, 107189 (2022).

39. Liu, X., Rahn, M. S., Ruan, Q., Yakobson, B. I. & Hersam, M. C. Probing borophene oxidation at the atomic scale. *Nanotechnology* **33**, 235702 (2022).

40. Li, Q. *et al.* Synthesis of borophane polymorphs through hydrogenation of borophene. *Science (80-.).* **371**, 1143–1148 (2021).

41. Li, H. *et al.* Scalable Production of Few-Layer Boron Sheets by Liquid-Phase Exfoliation and Their Superior Supercapacitive Performance. *ACS Nano* **12**, 1262–1272 (2018).

42. Hou, C. *et al.* Ultrastable Crystalline Semiconducting Hydrogenated Borophene. *Angew. Chemie* **132**, 10911–10917 (2020).

43. Lin, H. *et al.* Scalable Production of Freestanding Few-Layer $β$ 12 -Borophene Single Crystalline Sheets as Efficient Electrocatalysts for Lithium–Sulfur Batteries. *ACS Nano* **15**, 17327–17336 (2021).

44. Wu, Z. *et al.* van der Waals Epitaxial Growth of Borophene on a Mica Substrate toward a High-Performance Photodetector. *ACS Appl. Mater. Interfaces* **13**, 31808–31815 (2021).

45. Hou, C. *et al.* Ultrasensitive humidity sensing and the multifunctional applications of borophene–MoS2 heterostructures. *J. Mater. Chem. A* **9**, 13100–13108 (2021).

46. Chand, H., Kumar, A. & Krishnan, V. Borophene and Boron-Based Nanosheets: Recent Advances in Synthesis Strategies and Applications in the Field of Environment and Energy. *Adv. Mater. Interfaces* **8**, 2100045 (2021).

47. Mazaheri, A., Javadi, M. & Abdi, Y. Chemical Vapor Deposition of Two-Dimensional Boron Sheets by Thermal Decomposition of Diborane. *ACS Appl. Mater. Interfaces* **13**, 8844–8850 (2021).

48. Chahal, S. *et al.* Borophene via Micromechanical Exfoliation. *Adv. Mater.* **33**, 2102039 (2021).

49. Mannix, A. J., Zhang, Z., Guisinger, N. P., Yakobson, B. I. & Hersam, M. C. Borophene as a prototype

for synthetic 2D materials development. *Nat. Nanotechnol. 2018 136* **13**, 444–450 (2018).

50. Gao, E. *et al.* Mechanical exfoliation of two-dimensional materials. *J. Mech. Phys. Solids* **115**, 248–262 (2018).

51. Huo, C., Yan, Z., Song, X. & Zeng, H. 2D materials via liquid exfoliation: a review on fabrication and applications. *Sci. Bull.* **60**, 1994–2008 (2015).

52. Sang, X. *et al.* In situ atomistic insight into the growth mechanisms of single layer 2D transition metal carbides. *Nat. Commun. 2018 91* **9**, 1–9 (2018).

53. Kidambi, P. R. *et al.* In situ observations during chemical vapor deposition of hexagonal boron nitride on polycrystalline copper. *Chem. Mater.* **26**, 6380–6392 (2014).

54. Fei, L. *et al.* Direct TEM observations of growth mechanisms of two-dimensional MoS2 flakes. *Nat. Commun. 2016 71* **7**, 1–7 (2016).

55. Şar, H. *et al.* Long-Term Stability Control of CVD-Grown Monolayer MoS2. *Phys. status solidi – Rapid Res. Lett.* **13**, 1800687 (2019).

56. Choudhary, N., Park, J., Hwang, J. Y. & Choi, W. Growth of large-scale and thickness-modulated MoS2 nanosheets. *ACS Appl. Mater. Interfaces* **6**, 21215–21222 (2014).

57. Lasek, K. *et al.* Synthesis and characterisation of 2D transition metal dichalcogenides: Recent progress from a vacuum surface science perspective. *Surf. Sci. Rep.* **76**, 100523 (2021).

58. Hall, J. *et al.* Molecular beam epitaxy of quasi-freestanding transition metal disulphide monolayers on van der Waals substrates: a growth study. *2D Mater.* **5**, 025005 (2018).

59. Lin, Z. *et al.* 2D materials advances: from large scale synthesis and controlled heterostructures to improved characterisation techniques, defects and applications. *2D Mater.* **3**, 042001 (2016).

60. Zavabeti, A. *et al.* Two-Dimensional Materials in Large-Areas: Synthesis, Properties and Applications. *Nano-Micro Lett. 2020 121* **12**, 1–34 (2020).

61. Mannix, A. J., Kiraly, B., Hersam, M. C. & Guisinger, N. P. Synthesis and chemistry of elemental 2D materials. *Nat. Rev. Chem. 2017 12* **1**, 1–14 (2017).

62. Koefoed, L. *et al.* Facile electrochemical transfer of large-area single crystal epitaxial graphene from Ir(1 1 1). *J. Phys. D. Appl. Phys.* **48**, 115306 (2015).

63. Castellanos-Gomez, A. *et al.* Deterministic transfer of two-dimensional materials by all-dry viscoelastic stamping. *2D Mater.* **1**, 011002 (2014).

64. Schranghamer, T. F., Sharma, M., Singh, R. & Das, S. Review and comparison of layer transfer methods for two-dimensional materials for emerging applications. *Chem. Soc. Rev.* **50**, 11032–11054 (2021).

65. Wood, J. D. *et al.* Annealing free, clean graphene transfer using alternative polymer scaffolds. *Nanotechnology* **26**, 055302 (2015).

66. Lu, S. *et al.* Minimizing residues and strain in 2D materials transferred from PDMS. *Nanotechnology* **29**, 265203 (2018).

67. Gurarslan, A. *et al.* Surface-energy-assisted perfect transfer of centimeter-scale monolayer and few-layer MoS2 films onto arbitrary substrates. *ACS Nano* **8**, 11522–11528 (2014).

68. Hong, M. *et al.* Decoupling the Interaction between Wet-Transferred MoS2 and Graphite Substrate by an Interfacial Water Layer. *Adv. Mater. Interfaces* **5**, 1800641 (2018).

69. Deng, S., Sumant, A. V. & Berry, V. Strain engineering in two-dimensional nanomaterials beyond graphene. *Nano Today* **22**, 14–35 (2018).

70. Si, C., Sun, Z. & Liu, F. Strain engineering of graphene: a review. *Nanoscale* **8**, 3207–3217 (2016).

71. Conley, H. J. *et al.* Bandgap engineering of strained monolayer and bilayer MoS2. *Nano Lett.* **13**, 3626–3630 (2013).

72. Castellanos-Gomez, A. *et al.* Local strain engineering in atomically thin MoS2. *Nano Lett.* **13**, 5361–5366 (2013).

73. Zhu, C. R. *et al.* Strain tuning of optical emission energy and polarization in monolayer and bilayer MoS2. *Phys. Rev. B - Condens. Matter Mater. Phys.* **88**, 121301 (2013).

74. Feng, J., Qian, X., Huang, C. W. & Li, J. Strain-engineered artificial atom as a broad-spectrum solar energy funnel. *Nat. Photonics 2012 612* **6**, 866–872 (2012).

75. Carrascoso, F., Li, H., Frisenda, R. & Castellanos-Gomez, A. Strain engineering in single-, bi- and tri-layer MoS2, MoSe2, WS2 and WSe2. *Nano Res. 2020 146* **14**, 1698–1703 (2020).

76. Park, M. *et al.* MoS2-Based Tactile Sensor for Electronic Skin Applications. *Adv. Mater.* **28**, 2556–2562 (2016).

77. Manzeli, S., Allain, A., Ghadimi, A. & Kis, A. Piezoresistivity and Strain-induced Band Gap Tuning in Atomically Thin MoS2. *Nano Lett.* **15**, 5330–5335 (2015).

78. Hui, Y. Y. *et al.* Exceptional tunability of band energy in a compressively strained trilayer MoS2 sheet. *ACS Nano* **7**, 7126–7131 (2013).

79. Boland, C. S. *et al.* PtSe2 grown directly on polymer foil for use as a robust piezoresistive sensor. *2D Mater.* **6**, 045029 (2019).

80. Chen, Y. *et al.* Carrier mobility tuning of MoS2 by strain engineering in CVD growth process. *Nano Res. 2020 147* **14**, 2314–2320 (2020).

81. Yu, S., Xiong, H. D., Eshun, K., Yuan, H. & Li, Q. Phase transition, effective mass and carrier mobility of MoS2 monolayer under tensile strain. *Appl. Surf. Sci.* **325**, 27–32 (2015).

82. Kou, L., Du, A., Chen, C. & Frauenheim, T. Strain engineering of selective chemical adsorption on monolayer MoS2. *Nanoscale* **6**, 5156–5161 (2014).

83. Plechinger, G. *et al.* Low-temperature photoluminescence of oxide-covered single-layer MoS2. *Phys. status solidi – Rapid Res. Lett.* **6**, 126–128 (2012).

84. Carrascoso, F., Frisenda, R. & Castellanos-Gomez, A. Biaxial versus uniaxial strain tuning of single-layer MoS2. *Nano Mater. Sci.* **4**, 44–51 (2022).

85. Mohiuddin, T. M. G. *et al.* Uniaxial strain in graphene by Raman spectroscopy: G peak splitting, Grüneisen parameters, and sample orientation. *Phys. Rev. B - Condens. Matter Mater. Phys.* **79**, 205433 (2009).

86. Roldán, R., Castellanos-Gomez, A., Cappelluti, E. & Guinea, F. Strain engineering in semiconducting two-dimensional crystals. *J. Phys. Condens. Matter* **27**, 313201 (2015).

87. Ryu, Y. K. *et al.* Microheater Actuators as a Versatile Platform for Strain Engineering in 2D Materials. *Nano Lett.* **20**, 5339–5345 (2020).

88. Chaste, J. *et al.* Intrinsic Properties of Suspended MoS2 on SiO2/Si Pillar Arrays for Nanomechanics and Optics. *ACS Nano* **12**, 3235–3242 (2018).

89. Šrut Rakić, I. *et al.* Step-induced faceting and related electronic effects for graphene on Ir(332). *Carbon N. Y.* **110**, 267–277 (2016).

90. Li, Z. *et al.* Efficient strain modulation of 2D materials via polymer encapsulation. *Nat. Commun. 2020 111* **11**, 1–8 (2020).

91. Schmidt, R. *et al.* Reversible uniaxial strain tuning in atomically thin WSe2. *2D Mater.* **3**, 021011 (2016).

92. Chow, C. M. *et al.* Unusual Exciton-Phonon Interactions at van der Waals Engineered Interfaces. *Nano Lett.* **17**, 1194–1199 (2017).

93. Island, J. O. *et al.* Precise and reversible band gap tuning in single-layer MoSe2 by uniaxial strain. *Nanoscale* **8**, 2589–2593 (2016).

94. Baran, D., Corzo, D. & Blazquez, G. T. Flexible Electronics: Status, Challenges and Opportunities. *Front. Electron.* **0**, 2 (2020).

95. Wang, P. *et al.* The Evolution of Flexible Electronics: From Nature, Beyond Nature, and To Nature. *Adv. Sci.* **7**, 2001116 (2020).

96. Xiang, L. *et al.* Recent Advances in Flexible and Stretchable Sensing Systems: From the Perspective of System Integration. *ACS Nano* **14**, 6449–6469 (2020).

97. Wu, W. Stretchable electronics: functional materials, fabrication strategies and applications.

http://www.tandfonline.com/action/journalInformation?show=aimsScope&journalCode=tsta20#.VmBmuzZFCUk **20**, 187–224 (2019).

98. Akinwande, D., Petrone, N. & Hone, J. Two-dimensional flexible nanoelectronics. *Nat. Commun. 2014 51* **5**, 1–12 (2014).

99. Glavin, N. R., Muratore, C. & Snure, M. Toward 2D materials for flexible electronics: opportunities and outlook. *Oxford Open Mater. Sci.* **1**, (2020).

100. Masoud, M., Jaradat, Y., Manasrah, A. & Jannoud, I. Sensors of smart devices in the internet of everything (IOE) era: Big opportunities and massive doubts. *J. Sensors* **2019**, (2019).

101. Shalf, J. The future of computing beyond Moores Law. *Philos. Trans. R. Soc. A* **378**, (2020).

102. Thompson, S. E. & Parthasarathy, S. Moore's law: the future of Si microelectronics. *Mater. Today* **9**, 20–25 (2006).

103. Trung, T. Q., Lee, N.-E., Lee, -E N & Trung, T. Q. Recent Progress on Stretchable Electronic Devices with Intrinsically Stretchable Components. *Adv. Mater.* **29**, 1603167 (2017).

104. Zhou, K. *et al.* Tunable and Nacre-Mimetic Multifunctional Electronic Skins for Highly Stretchable Contact-Noncontact Sensing. *Small* **17**, 2100542 (2021).

105. Zhao, J. *et al.* Highly Sensitive MoS2 Humidity Sensors Array for Noncontact Sensation. *Adv. Mater.* **29**, 1702076 (2017).

106. Jiang, D. *et al.* Flexible electronics based on 2D transition metal dichalcogenides. *J. Mater. Chem. A* **10**, 89–121 (2021).

107. Bertolazzi, S., Brivio, J. & Kis, A. Stretching and breaking of ultrathin MoS 2. *ACS Nano* **5**, 9703–9709 (2011).

108. Kim, J. H., Jeong, J. H., Kim, N., Joshi, R. & Lee, G. H. Mechanical properties of two-dimensional materials and their applications. *J. Phys. D. Appl. Phys.* **52**, 083001 (2018).

109. Park, H. *et al.* Flexible and Transparent Thin-Film Transistors Based on Two-Dimensional Materials for Active-Matrix Display. *ACS Appl. Mater. Interfaces* **12**, 4749–4754 (2020).

110. Lee, G. H. *et al.* Flexible and transparent MoS2 field-effect transistors on hexagonal boron nitride-graphene heterostructures. *ACS Nano* **7**, 7931–7936 (2013).

111. Guo, H. *et al.* Transparent, flexible, and stretchable WS2 based humidity sensors for electronic skin. *Nanoscale* **9**, 6246–6253 (2017).

112. Lemme, M. C. *et al.* Nanoelectromechanical Sensors Based on Suspended 2D Materials. *Research* **2020**, 1–25 (2020).

113. Wu, W. *et al.* Piezoelectricity of single-atomic-layer MoS2 for energy conversion and piezotronics. *Nat. 2014 5147523* **514**, 470–474 (2014).

114. Krustok, J. *et al.* Local strain-induced band gap fluctuations and exciton localization in aged WS2 monolayers. *AIP Adv.* **7**, 065005 (2017).

115. Scalise, E., Houssa, M., Pourtois, G., Afanas'ev, V. & Stesmans, A. Strain-induced semiconductor to metal transition in the two-dimensional honeycomb structure of MoS2. *Nano Res. 2012 51* **5**, 43–48 (2011).

116. Yang, S., Chen, Y. & Jiang, C. Strain engineering of two-dimensional materials: Methods, properties, and applications. *InfoMat* **3**, 397–420 (2021).

117. Meitl, M. A. *et al.* Transfer printing by kinetic control of adhesion to an elastomeric stamp. *Nat. Mater.* **5**, 33–38 (2006).

118. Conti, S. *et al.* Low-voltage 2D materials-based printed field-effect transistors for integrated digital and analog electronics on paper. *Nat. Commun. 2020 111* **11**, 1–9 (2020).

119. Gant, P. *et al.* A strain tunable single-layer MoS2 photodetector. *Mater. Today* **27**, 8–13 (2019).

120. Blake, P. *et al.* Making graphene visible. *Appl. Phys. Lett.* **91**, 063124 (2007).

121. Lin, Z. *et al.* Controllable Growth of Large–Size Crystalline MoS2 and Resist-Free Transfer Assisted with a Cu Thin Film. *Sci. Reports 2015 51* **5**, 1–10 (2015).

122. Senkić, A., Bajo Josip, Antonio, S., Radatović, B. & Vujičić, N. Effects of CVD Growth Parameters on Global and Local Optical Properties of MoS2 Monolayers. *Prep.* (2022).

123. Liao, M. *et al.* Precise control of the interlayer twist angle in large scale MoS2 homostructures. *Nat. Commun. 2020 111* **11**, 1–8 (2020).

124. Han, S. W. *et al.* Interface Defect Engineering of a Large-Scale CVD-Grown MoS2 Monolayer via Residual Sodium at the SiO2/Si Substrate. *Adv. Mater. Interfaces* **8**, 2100428 (2021).

125. Shi, Q. *et al.* Substrate Developments for the Chemical Vapor Deposition Synthesis of Graphene. *Adv. Mater. Interfaces* **7**, 1902024 (2020).

126. Kralj, M. *et al.* Graphene on Ir(111) characterized by angle-resolved photoemission. *Phys. Rev. B - Condens. Matter Mater. Phys.* **84**, 075427 (2011).

127. Van Gastel, R. *et al.* Selecting a single orientation for millimeter sized graphene sheets. *Appl. Phys. Lett.* **95**, 121901 (2009).

128. Coraux, J. *et al.* Growth of graphene on Ir(111). *New J. Phys.* **11**, 023006 (2009).

129. Coraux, J., N'Diaye, A. T., Busse, C. & Michely, T. Structural coherency of graphene on Ir(111). *Nano Lett.* **8**, 565–570 (2008).

130. Pielić, B. Van der Waals epitaxy of two-dimensional transition metal disulphides.

131. Coraux, J., N'Diaye, A. T., Busse, C. & Michely, T. Structural coherency of graphene on Ir(111). *Nano Lett.* **8**, 565–570 (2008).

132. Pielić, B. *et al.* Electronic Structure of Quasi-Freestanding WS2/MoS2 Heterostructures. *ACS Appl. Mater. Interfaces* **13**, 50552–50563 (2021).

133. Radatović, B. *et al.* Macroscopic Single-Phase Monolayer Borophene on Arbitrary Substrates. *ACS Appl. Mater. Interfaces* **14**, 21727–21737 (2022).

134. Petrović, M., Hagemann, U., Horn-von Hoegen, M. & Meyer zu Heringdorf, F.-J. Microanalysis of single-layer hexagonal boron nitride islands on Ir(111). *Appl. Surf. Sci.* **420**, 504–510 (2017).

135. Vinogradov, N. A., Lyalin, A., Taketsugu, T., Vinogradov, A. S. & Preobrajenski, A. Single-Phase Borophene on Ir(111): Formation, Structure, and Decoupling from the Support. *ACS Nano* **13**, 14511–14518 (2019).

136. Cuxart, M. G. *et al.* Borophenes made easy. *Sci. Adv.* **7**, 1–8 (2021).

137. Pielić, B. *et al.* Sulfur Structures on Bare and Graphene-Covered Ir(111). *J. Phys. Chem. C* **124**, 6659–6668 (2020).

138. Jadriško, V. *et al.* Structural and optical characterisation of nanometer sized MoS2/graphene heterostructures for potential use in optoelectronic devices. *FlatChem* **2022**, 100397 (2022).

139. Niehues, I. *et al.* Strain transfer across grain boundaries in MoS2 monolayers grown by chemical vapor deposition. *2D Mater.* **5**, 031003 (2018).

140. Wajid, A. On the accuracy of the quartz-crystal microbalance (QCM) in thin-film depositions. *Sensors Actuators A Phys.* **63**, 41–46 (1997).

141. Chen, Y. Nanofabrication by electron beam lithography and its applications: A review. *Microelectron. Eng.* **135**, 57–72 (2015).

142. Ichinokawa, T., Iiyama, M., Onoguchi, A. & Kobayashi, T. Charging effect of specimen in scanning electron microscopy. *Jpn. J. Appl. Phys.* **13**, 1272–1277 (1974).

143. Ali, A. S. Application of Nanomaterials in Environmental Improvement. *Nanotechnol. Environ.* (2020).

144. Horcas, I. *et al.* WSXM : A software for scanning probe microscopy and a tool for nanotechnology. *Rev. Sci. Instrum.* **78**, 13705 (2007).

145. Cong, X., Liu, X. L., Lin, M. L. & Tan, P. H. Application of Raman spectroscopy to probe fundamental properties of two-dimensional materials. *npj 2D Mater. Appl. 2020 41* **4**, 1–12 (2020).

146. Tan, P. H. *et al.* The shear mode of multilayer graphene. *Nat. Mater. 2012 114* **11**, 294–300 (2012).

147. Tan, P.-H. *Raman Spectroscopy of Two-Dimensional Materials*. vol. 276 (Springer Singapore, 2019).

148. Bonini, N., Lazzeri, M., Marzari, N. & Mauri, F. Phonon anharmonicities in graphite and graphene. *Phys. Rev. Lett.* **99**, 176802 (2007).

149. Wilson, J. A., Di Salvo, F. J. & Mahajan, S. Charge-Density Waves in Metallic, Layered, Transition-Metal Dichalcogenides. *Phys. Rev. Lett.* **32**, 882 (1974).

150. Mak, K. F., Lee, C., Hone, J., Shan, J. & Heinz, T. F. Atomically thin MoS_2: a new direct-gap semiconductor. *Phys. Rev. Lett.* **105**, (2010).

151. Ross, J. S. *et al.* Electrical control of neutral and charged excitons in a monolayer semiconductor. *Nat. Commun. 2013 41* **4**, 1–6 (2013).

152. Pal, S. K. Versatile photoluminescence from graphene and its derivatives. *Carbon N. Y.* **88**, 86–112 (2015).

153. Mak, K. F., Lee, C., Hone, J., Shan, J. & Heinz, T. F. Atomically thin MoS_2: a new direct-gap semiconductor. *Phys. Rev. Lett.* **105**, (2010).

154. Frisenda, R. *et al.* Micro-reflectance and transmittance spectroscopy: A versatile and powerful tool to characterize 2D materials. *J. Phys. D. Appl. Phys.* **50**, (2017).

155. Niu, Y. *et al.* Thickness-Dependent Differential Reflectance Spectra of Monolayer and Few-Layer MoS2, MoSe2, WS2 and WSe2. *Nanomater. 2018, Vol. 8, Page 725* **8**, 725 (2018).

156. Radatović, B. Devices based on layered 2D materials and their heterostructures. *Master thesis* (2016).

157. Çakıroğlu, O., Frisenda, R. & Castellanos-Gomez, A. An Automated System for Strain Engineering and Straintronics of Single-Layer MoS2. *Prep.*

158. Gurarslan, A. *et al.* Surface-energy-assisted perfect transfer of centimeter-scale monolayer and few-layer MoS2 films onto arbitrary substrates. *ACS Nano* **8**, 11522–11528 (2014).

159. Li, H. *et al.* A universal, rapid method for clean transfer of nanostructures onto various substrates. *ACS Nano* **8**, 6563–6570 (2014).

160. Ma, X. *et al.* Capillary-Force-Assisted Clean-Stamp Transfer of Two-Dimensional Materials. *Nano Lett.* **17**, 6961–6967 (2017).

161. Rajapakse, M. *et al.* Intercalation as a versatile tool for fabrication, property tuning, and phase transitions in 2D materials. *npj 2D Mater. Appl. 2021 51* **5**, 1–21 (2021).

162. Hassanpour Amiri, M. *et al.* Doping free transfer of graphene using aqueous ammonia flow. *RSC Adv.* **10**, 1127–1131 (2020).

163. Li, Q., Zhou, Q., Shi, L., Chen, Q. & Wang, J. Recent advances in oxidation and degradation mechanisms of ultrathin 2D materials under ambient conditions and their passivation strategies. *J. Mater. Chem. A* **7**, 4291–4312 (2019).

164. Wang, Y. *et al.* Electrochemical Delamination of CVD-Grown Graphene Film: Toward the Recyclable Use of Copper Catalyst. *ACS Nano* **5**, 9927–9933 (2011).

165. Kim, G. *et al.* Growth of High-Crystalline, Single-Layer Hexagonal Boron Nitride on Recyclable Platinum Foil. *Nano Lett.* **13**, 1834–1839 (2013).

166. Fan, S., Vu, Q. A., Tran, M. D., Adhikari, S. & Lee, Y. H. Transfer assembly for two-dimensional van der Waals heterostructures. *2D Mater.* **7**, 022005 (2020).

167. Gao, L. *et al.* Repeated growth and bubbling transfer of graphene with millimetre-size single-crystal grains using platinum. *Nat. Commun.* **3**, 699 (2012).

168. Paredes, J. I. & Munuera, J. M. Recent advances and energy-related applications of high quality/chemically doped graphenes obtained by electrochemical exfoliation methods. *J. Mater. Chem. A* **5**, 7228–7242 (2017).

169. Vazquez-Mena, O., Gross, L., Xie, S., Villanueva, L. G. & Brugger, J. Resistless nanofabrication by stencil lithography: A review. *Microelectron. Eng.* **132**, 236–254 (2015).

170. Li, F. *et al.* Tuning Transport and Photoelectric Performance of Monolayer MoS2 Device by E-Beam Irradiation. *Adv. Mater. Interfaces* **5**, 1800348 (2018).

171. Clericò, V., Amado, M. & Diez, E. Electron beam lithography and its use on 2D materials.

Nanofabrication (2020).

172. Feng, B. *et al.* Experimental realization of two-dimensional boron sheets. *Nat. Chem.* **8**, 563–568 (2016).

173. Mannix, A. J. *et al.* Synthesis of borophenes: Anisotropic, two-dimensional boron polymorphs. *Science (80-.).* **350**, 1513–1516 (2015).

174. Wolfschmidt, H. *et al.* STM, SECPM, AFM and electrochemistry on single crystalline surfaces. *Materials (Basel).* **3**, 4196–4213 (2010).

175. N'Diaye, A. T. *et al.* In situ observation of stress relaxation in epitaxial graphene. *New J. Phys.* **11**, 113056 (2009).

176. Petrović, M., Sadowski, J. T., Šiber, A. & Kralj, M. Wrinkles of graphene on Ir(1 1 1): Macroscopic network ordering and internal multi-lobed structure. *Carbon N. Y.* **94**, 856–863 (2015).

177. Shearer, C. J., Slattery, A. D., Stapleton, A. J., Shapter, J. G. & Gibson, C. T. Accurate thickness measurement of graphene. *Nanotechnology* **27**, 125704 (2016).

178. Wu, R. *et al.* Large-area single-crystal sheets of borophene on Cu(111) surfaces. *Nat. Nanotechnol.* **14**, 44–49 (2019).

179. Nemes-Incze, P., Osváth, Z., Kamarás, K. & Biró, L. P. Anomalies in thickness measurements of graphene and few layer graphite crystals by tapping mode atomic force microscopy. *Carbon N. Y.* **46**, 1435–1442 (2008).

180. Sheng, S. *et al.* Raman spectroscopy of two-dimensional borophene sheets. *ACS Nano* **13**, 4133–4139 (2019).

181. Ranjan, P. *et al.* Freestanding Borophene and Its Hybrids. *Adv. Mater.* **31**, 1900353 (2019).

182. Starodub, E. *et al.* In-plane orientation effects on the electronic structure, stability, and Raman scattering of monolayer graphene on Ir(111). *Phys. Rev. B* **83**, 125428 (2011).

183. Amsalem, P., Giovanelli, L., Themlin, J. M. & Angot, T. Electronic and vibrational properties at the ZnPc/Ag(110) interface. *Phys. Rev. B - Condens. Matter Mater. Phys.* **79**, 235426 (2009).

184. Scheuschner, N., Gillen, R., Staiger, M. & Maultzsch, J. Interlayer resonant Raman modes in few-layer MoS2. *Phys. Rev. B - Condens. Matter Mater. Phys.* **91**, 235409 (2015).

185. Zhao, Y. *et al.* Interlayer vibrational modes in few-quintuple-layer Bi2Te3 and Bi2Se3 two-dimensional crystals: Raman spectroscopy and first-principles studies. *Phys. Rev. B - Condens. Matter Mater. Phys.* **90**, 245428 (2014).

186. Xiang, Q. *et al.* Unveiling the origin of anomalous low-frequency Raman mode in CVD-grown monolayer WS2. *Nano Res.* **14**, 4314–4320 (2021).

187. Liang, L. *et al.* Low-Frequency Shear and Layer-Breathing Modes in Raman Scattering of Two-Dimensional Materials. *ACS Nano* **11**, 11777–11802 (2017).

188. Velický, M. *et al.* Strain and Charge Doping Fingerprints of the Strong Interaction between Monolayer MoS2and Gold. *J. Phys. Chem. Lett.* **11**, 6112–6118 (2020).

189. Gao, M., Yan, X. W., Wang, J., Lu, Z. Y. & Xiang, T. Electron-phonon coupling in a honeycomb borophene grown on Al(111) surface. *Phys. Rev. B* **100**, 024503 (2019).

190. Li, L. *et al.* Angstrom-Scale Spectroscopic Visualization of Interfacial Interactions in an Organic/Borophene Vertical Heterostructure. *J. Am. Chem. Soc.* **143**, 15624–15634 (2021).

191. Li, L. *et al.* Chemically identifying single adatoms with single-bond sensitivity during oxidation reactions of borophene. *Nat. Commun.* **13**, 1796 (2022).

192. Zhang, X. *et al.* Phonon and Raman scattering of two-dimensional transition metal dichalcogenides from monolayer, multilayer to bulk material. *Chem. Soc. Rev.* **44**, 2757–2785 (2015).

193. Zhang, Y. *et al.* Scaling law for strain dependence of Raman spectra in transition-metal dichalcogenides. *J. Raman Spectrosc.* **51**, 1353–1361 (2020).

194. Ciuk, T. *et al.* Properties of chemical vapor deposition graphene transferred by high-speed electrochemical delamination. *J. Phys. Chem. C* **117**, 20833–20837 (2013).

195. Wong, C. H. A. & Pumera, M. Electrochemical Delamination and Chemical Etching of Chemical Vapor

Deposition Graphene: Contrasting Properties. *J. Phys. Chem. C* **120**, 4682–4690 (2016).

196. N'Diaye, A. T. *et al.* In situ observation of stress relaxation in epitaxial graphene. *New J. Phys.* **11**, 113056 (2009).

197. Liang, X. *et al.* Toward clean and crackless transfer of graphene. *ACS Nano* **5**, 9144–9153 (2011).

198. Wu, J. Bin, Lin, M. L., Cong, X., Liu, H. N. & Tan, P. H. Raman spectroscopy of graphene-based materials and its applications in related devices. *Chem. Soc. Rev.* **47**, 1822–1873 (2018).

199. Das, A., Chakraborty, B. & Sood, A. K. Raman spectroscopy of graphene on different substrates and influence of defects. *Bull. Mater. Sci. 2008 313* **31**, 579–584 (2008).

200. Feng, T. *et al.* Unipolar to ambipolar conversion in graphene field-effect transistors. *Appl. Phys. Lett.* **101**, 253505 (2012).

201. Bolotin, K. I. *et al.* Ultrahigh electron mobility in suspended graphene. *Solid State Commun.* **146**, 351–355 (2008).

202. Verguts, K. *et al.* Controlling Water Intercalation Is Key to a Direct Graphene Transfer. *ACS Appl. Mater. Interfaces* **9**, 37484–37492 (2017).

203. Kouroupis-Agalou, K. *et al.* Fragmentation and exfoliation of 2-dimensional materials: a statistical approach. *Nanoscale* **6**, 5926–5933 (2014).

204. Wang, S. *et al.* Shape evolution of monolayer MoS2 crystals grown by chemical vapor deposition. *Chem. Mater.* **26**, 6371–6379 (2014).

205. Najmaei, S. *et al.* Vapour phase growth and grain boundary structure of molybdenum disulphide atomic layers. *Nat. Mater. 2013 128* **12**, 754–759 (2013).

206. Yoo, H., Heo, K., Ansari, M. H. R. & Cho, S. Recent Advances in Electrical Doping of 2D Semiconductor Materials: Methods, Analyses, and Applications. *Nanomater. 2021, Vol. 11, Page 832* **11**, 832 (2021).

207. Cadiz, F. *et al.* Ultra-low power threshold for laser induced changes in optical properties of 2D molybdenum dichalcogenides. *2D Mater.* **3**, 045008 (2016).

208. Liu, W., Sarkar, D., Kang, J., Cao, W. & Banerjee, K. Impact of Contact on the Operation and Performance of Back-Gated Monolayer MoS2 Field-Effect-Transistors. *ACS Nano* **9**, 7904–7912 (2015).

209. Tong, X., Ashalley, E., Lin, F., Li, H. & Wang, Z. M. Advances in MoS2-Based Field Effect Transistors (FETs). *Nano-Micro Lett.* **7**, 203–218 (2015).

210. Radisavljevic, B. & Kis, A. Mobility engineering and a metal–insulator transition in monolayer MoS2. *Nat. Mater. 2013 129* **12**, 815–820 (2013).

211. Sebastian, A., Pendurthi, R., Choudhury, T. H., Redwing, J. M. & Das, S. Benchmarking monolayer MoS2 and WS2 field-effect transistors. *Nat. Commun. 2021 121* **12**, 1–12 (2021).

212. Dolui, K., Rungger, I. & Sanvito, S. Origin of the n-type and p-type conductivity of MoS2 monolayers on a SiO2 substrate. *Phys. Rev. B - Condens. Matter Mater. Phys.* **87**, 165402 (2013).

213. Bao, W., Cai, X., Kim, D., Sridhara, K. & Fuhrer, M. S. High mobility ambipolar MoS2 field-effect transistors: Substrate and dielectric effects. *Appl. Phys. Lett.* **102**, 042104 (2013).

214. Hao, S., Yang, B. & Gao, Y. Orientation-specific transgranular fracture behavior of CVD-grown monolayer MoS2 single crystal. *Appl. Phys. Lett.* **110**, 153105 (2017).

215. Tweedie, M. E. P. *et al.* Inhomogeneous Strain Release during Bending of WS2 on Flexible Substrates. *ACS Appl. Mater. Interfaces* **10**, 39177–39186 (2018).

216. Yin, Z. *et al.* Single-layer MoS 2 phototransistors. *ACS Nano* **6**, 74–80 (2012).

217. Buscema, M. *et al.* Photocurrent generation with two-dimensional van der Waals semiconductors. *Chem. Soc. Rev.* **44**, 3691–3718 (2015).

218. Wu, Y. C. *et al.* Extrinsic Origin of Persistent Photoconductivity in Monolayer MoS2 Field Effect Transistors. *Sci. Reports 2015 51* **5**, 1–10 (2015).

219. Tran, M. D. *et al.* Role of Hole Trap Sites in MoS2 for Inconsistency in Optical and Electrical Phenomena. *ACS Appl. Mater. Interfaces* **10**, 10580–10586 (2018).

220. Khan, M. F., Nazir, G., Lermolenko, V. M. & Eom, J. Electrical and photo-electrical properties of MoS2 nanosheets with and without an Al2O3 capping layer under various environmental conditions. *Sci. Technol. Adv. Mater.* **17**, 166 (2016).

221. Pradhan, N. R. *et al.* High Photoresponsivity and Short Photoresponse Times in Few-Layered WSe2 Transistors. *ACS Appl. Mater. Interfaces* **7**, 12080–12088 (2015).

222. Yang, M., Kim, T. Y., Lee, T. & Hong, S. Nanoscale enhancement of photoconductivity by localized charge traps in the grain structures of monolayer MoS2. *Sci. Reports 2018 81* **8**, 1–9 (2018).

223. Wang, S. W. *et al.* Thermally Strained Band Gap Engineering of Transition-Metal Dichalcogenide Bilayers with Enhanced Light-Matter Interaction toward Excellent Photodetectors. *ACS Nano* **11**, 8768–8776 (2017).

224. Krustok, J. *et al.* Optical study of local strain related disordering in CVD-grown MoSe2 monolayers. *Appl. Phys. Lett.* **109**, 253106 (2016).

225. Mak, K. F., He, K., Shan, J. & Heinz, T. F. Control of valley polarization in monolayer MoS2 by optical helicity. *Nat. Nanotechnol. 2012 78* **7**, 494–498 (2012).

226. Borys, N. J. *et al.* Anomalous Above-Gap Photoexcitations and Optical Signatures of Localized Charge Puddles in Monolayer Molybdenum Disulfide. *ACS Nano* **11**, 2115–2123 (2017).

227. Niehues, I. *et al.* Strain tuning of the Stokes shift in atomically thin semiconductors. *Nanoscale* **12**, 20786–20796 (2020).

228. Wang, L., Nilsson, Z. N., Tahir, M., Chen, H. & Sambur, J. B. Influence of the Substrate on the Optical and Photo-electrochemical Properties of Monolayer MoS2. *ACS Appl. Mater. Interfaces* **12**, 15034–15042 (2020).

229. Niehues, I. *et al.* Strain Control of Exciton-Phonon Coupling in Atomically Thin Semiconductors. *Nano Lett.* **18**, 1751–1757 (2018).

Curriculum vitae

Borna Radatović

Address: Tratina 18, 10 000, Zagreb, Croatia; **Date of Birth:** 19.04.1993.; **Mail:** bradatovic@ifs.hr

---

Education

2016 – Ongoing **Postgraduate doctoral program: Solid state physics; Faculty of Science, University of Zagreb,**
- PhD „Flexible devices based on 2D materials“ under the mentorship of dr. sc. Marin Petrović

2011 – 2016 **Faculty of Science, Physics department: research physics, University of Zagreb, Croatia**
- Master of Science in Physics: „Devices based on layered 2D materials and their heterostructures“ under the mentorship of dr. sc. Marko Kralj – September 2016.

2007 – 2011 **High school: V. Gymnasium, Zagreb, Croatia**

Work experience

Research related

2016 – Ongoing **Institute of Physics, Zagreb, Croatia**
Research assistant

2019 – Ongoing **Nanoing j.d.o.o., Zagreb, Croatia**
Founder and CEO of startup

Sep. 2015 – Dec. 2015 **Institute for Semiconducting Physics, Johannes Kepler University, Linz, Austria**
Research assistant, ERASMUS internship, research group of dr. sc. Georgios Katsaros

2014 – 2017 **Institute of Physics, Zagreb, Croatia**
Volunteer, research group of dr. sc. Marko Kralj

Teaching related

2019 – Ongoing **Faculty of Science, Physics department, University of Zagreb**
Teaching assistant, prof. dr. sc. Damir Pajić: Course ”Advanced Laboratory Physics 1 & 2”.

2018 – Ongoing **Zagreb University of Applied Sciences, Croatia**
Teaching assistant, prof. Alemka Knapp: Course ”Physics”.

2018 – 2019 **Faculty of Electrical Engineering and Computing, University of Zagreb, Croatia**
Teaching assistant, prof. dr. sc. Lahorija Bistričić: Course ”Physics 1”.

Scienctific projects and visits

Project leader

2019 – Ongoing **NEMS (nanoelectromechanical system) of acceleration, velocity and position sensors**
Principal Investigator, Hamag-Bicro Proof of Concept 8 project

Project associate

2021 – Ongoing **Boron – based 2D materials**
Associate, Croatian National Science Foundation project led by dr.sc. Marin Petrović

2018 – Ongoing **Photoexcitations in 2D Semiconductors**

Associate, Croatian National Science Foundation project led by dr.sc. Nataša Vujičić

2017 – Ongoing **Center of Excellence for Advanced Materials and Sensing Devices**
Associate, EU infrastructural project led by dr.sc. Marko Kralj

2017 – Ongoing **Center for Advanced Laser Techniques – CALT**
Associate, EU infrastructural project led by dr.sc. Damir Aumiler

2016 – 2017 **QuartzNano: QCM sensors improved on nanolevel**
Associate, Hamag-Bicro Proof of Concept 6 project

Bilateral projects

2020 – Ongoing **Organic semiconductor nanostructures on two-dimensional transition metal dichalcogenide substrates**
Associate, Austria-Croatia with Institute of Physics University of Leoben and dr.sc. Christian Teichert

2020 – Ongoing **Synthesis of novel low-dimensional materials for information applications and the characterisation of their magnetic and optical properties**
Associate, China – Croatia with Bejing Institute of Technology and dr. sc. Yeliang Wang

2018 – 2019 **Two – dimensional metals**
Associate, Germany – Croatia with Faculty for Physics University of Siegen and dr.sc. Carsten Busse

2016 – 2017 **Intercalation of epitaxial dichalcogenides**
Associate, Germany – Croatia with Institute for Material Physics of Münster and dr.sc. Carsten Busse

2016 – 2017 **Tuning many-body interactions in graphene by Cesium intercalation**
Associate, Serbia – Croatia with Institute of Physics Belgrade and dr.sc. Marko Spasenović

Visits

November 2021 **Materials Science Institute of Madrid – collaboration with group of dr. sc. Andres Castellanos Gomez**

September 2021 **University of Leoben, Austria – collaboration with group of dr. sc. Christian Teichert**

May 2019 **University of Belgrade, Serbia – collaboration with group of dr. sc. Đorđe Janaćković**

November 2017 **University of Münster, Germany – collaboration with group of dr. sc. Rudolph Bratschitsch**

April 2017 **Johannes Kepler University, Austria – collaboration with group of dr. sc. Andreas Ebner**

June 2016 **University of Hannover, Germany – collaboration with group of dr. sc. Christoph Tegenkamp**

List of publications

2022 **Macroscopic singe-layer borophene sheets on arbitrary substrates**
B. Radatović, V. Jadriško, S. Kamal, M.Kralj, D. Novko, N. Vujičić, M. Petrović, *ACS AMI*. 2022; 14 (18), 21727-21737,

2022 **Structural and optical characterisation of nanometer sized MoS_2/Graphene heterostructures for potential use in optoelectronic devices**
V. Jadriško, B. Radatović, B. Pielić, C Gadermaier, M. Kralj, N. Vujičić, *Flat Chem. 2022. 34, 100397*

2022 **Biocompatible hydroxyapatite nanoparticles as templates for the preparation of thin film polyelectrolyte multilayer nanocapsules**
T. Klačić, N. Peranić, B. Radatović, D. Kovačević, *Colloids and Surfaces A*. 2022; 648, 129385

2022 **Thiolated Chitosan Conjugated Liposomes for Oral Delivery of Selenium Nanoparticles**
A. Selmani, E. Seibert, C. Tetyczka, D. Kuehnelt, B. Radatović, E. Roblegg, R. Prassl et.al,, *Pharmaceutics*. 2022; 14 (4), 803

2021 **Comparison of the Effect of the Amino Acids on Spontaneous Formation and Transformation of Calcium Phosphates**
I. Erceg, N. Maltar-Stmečki, M. Ćurlin, B. Radatović, N. M. Mlinarić, D. Kralj, M. D. Sikirić et. al., *Crystals*. 2021; 11(7), 792

2021 **Precipitation at room temperature as a fast and versatile method for Calcium Phosphate/TiO_2 nanocomposites synthesis**
I. Erceg, A. Selmai, A. Gajović, B. Radatović, B. Šegota, I. Vinković Vrček, M. D. Sikirić, et. al., *Nanomaterials* 2021; 11(6), 1523

2021 **Impact of sandblasting on morphology, structure and conductivity of zirconia dental ceramics material**
M. Jakovac, T. Klaser, B. Radatović, B. Bafti, Ž. Skoko, L. Pavić, M. Žic, *Materials* 2021; 14(11), 2834

2021 **Investigation of Ion Irradiation Effects in Silicon and Graphite Produced by 23 MeV I Beam.**
K. Tomić Luketić, M. Karlušić, A. Gajović, S. Fanzić, J. H. O'Connel, B. Radatović, M. Kralj, *Materials* 2021; 14(8):1904.

2020 **Surface Characterisation and Conductivity of Two Types of Lithium-Based Glass Ceramics after Accelerating Ageing.**
M. Jakovac, T. Klaser, B. Radatović, Ž. Skoko, L. Pavić, M. Žic, *Materials* 2020; 13(24):5632.

2020 **The Influence of Different Classes of Amino Acids on Calcium Phosphates Seeded Growth.**
M.Josipović, M. Kovačević, S. Mateša, M. Kostešić, B. Radatović, D. Kralj, M. D. Sikirić et.al., *Materials* 2020; 13(21):4798.

2018 **Strain transfer across grain boundaries in MoS_2 monolayers grown by chemical vapor deposition**
I. Niehues, R. Schmidt, V. Jadriško, B. Radatović, M. Kralj, S. M. de Vasconcellos, R. Bratschitsch et. al., *2D Materials* 2018; 5 031003

2017 **Process for forming ready-to-use QCM sensors with atomically flat surface suitable for STM measurements**
T. Vuletić, B. Radatović, M. Jurdana, I. D. Marion, M. Kralj, WO/2019/042549

Conferences & Schools

May 2022 **International Scientific Meeting on Vacuum Science and Technique**
Selca, Croatia Invited talk title: "Macroscopic singe-layer borophene sheets on arbitrary substrates"

September 2021 **International Symposium on Nanoscale Research**
Leoben, Austria Presentation title: "Macroscopic singe-layer borophene sheets on arbitrary substrates"

January 2020 **Faculty of Science PhD Symposium**
Zagreb, Croatia Presentation title: "Flexible devices based on layered 2D materials"

January 2020 **Health Tech Hub Styria Pitch & Partner**
Graz, Austria

July 2019 **Summer School in Physics of Sensing and Processing**
Bologna, Italy

March 2019 **Symposium on Direct Write, Optical, Ion and Electron Beam Lithography**
Workshop at Institute for Science and Technology – IST, Wien, Austria

November 2018 **11th meeting of Croatian Physical Society – HFD**
Beli Manastir, Croatia Presentation title: "Atomically flat QCM sensors and applications"

August 2018 **Greta Pifat Mrzljak International School of Biophysics**
Split, Croatia. Organizing committee

August 2018 **ICN+T International conference on Nanoscience and Technology**
Brno, Czech Republic Presentation title: "Effects of electric field doping, photodoping and strain on optical properties of CVD grown MoS_2"

July 2018 **TESCAN e-beam lithography training**
Brno, Czech Republic

June 2018 & 2019 **Summer School for Young Physicist**
Invited talk title: 2D world at Veli Lošinj, Croatia

June 2017 **"Workshop on Modern Trends in Solid State Quantum Physics"**
Workshop at Institute for Science and Technology - IST, Wien, Austria

January 2017 **"Winter School on Photophysics of Hybrid Interfaces"**
NanoSpectroscopy COST training school, Ambroz pod Krvavcem, Slovenia

---

Scholarships and awards

2020 **Best oral presentation on 2020 Symposium of PhD students of Faculty of Science, University of Zagreb**

2018 **Best poster presentation on ICN+T (International conference on Nanoscience and Technology) 2018**

2015 **ERASMUS+ scholarship on the Institute for semiconducting physics of Johannes Kepler University, Linz, Austria**